UNIVERSITY OF CALIFORNIA
RIVERSIDE

Mathematical Modeling Study of the Impacts of Boundary Conditions and a Pseudo-3D Mechanism on the Maintenance of the Shoot Apical Meristem of *Arabidopsis thaliana*

A Dissertation submitted in partial satisfaction
of the requirements for the degree of

Doctor of Philosophy

in

Mathematics

by

Christian Thomas Michael

September 2022

Dissertation Committee:

Mark Alber, Chairperson
Weitao Chen
Venugopala Reddy Gonehal

The Dissertation of Christian Thomas Michael is approved:

Committee Chairperson

University of California, Riverside

Acknowledgments

I would like to express gratitude and appreciation for my advisor Dr. Mark Alber; for formulation of my research problems and for his guidance and mentorship which was crucial to keep me on course. Research can easily go off-the-rails or lose focus and I thank him for helping me focus my direction and build my ability to communicate.

I would like to thank Dr. Kevin Rodriguez, Professor G. Venugopala Reddy, Alex Plong, and everyone else who contributed towards the experimental support for this project. Without your passion to pursue biological insights *in silica*, none of this would have been possible.

I would also like to thank Calvin-Khang Ta for his assistance in 3D segmentation of the 3D data in this work, and professor Amit Roy-Chowdhury for providing support and direction for this.

I would like to thank Dr. Mikahl Banwarth-Kuhn for her perpetual mentorship and patience with me as I learned how to navigate the ropes of this research, as well as helping me to sharpen a good idea into a clear point.

Finally, I would like to acknowledge Rebecca Kurtz-Garcia and Luke Klein of the Statistics department of the University of California, Riverside, who together assisted in implementing high-throughput statistical analysis using standard methods in R for this work.

The text of this dissertation is in part a reprint of the material as it appears in: [1] Mikahl Banwarth-Kuhn, Kevin Rodriguez, Christian Michael, Calvin-Khang Ta, Alexander Plong, Eric Bourgain-Chang, Ali Nematbakhsh, Weitao Chen, Amit Roy-Chowdhury, G. Venugopala Reddy, and Mark Alber. Combined computational modeling and experimental analysis integrating chemical and mechanical signals suggests possible mechanism of shoot meristem maintenance. PLOS Computational Biology, 18(6):e1010199, jun 2022. Individual chapters and sections which include this work include disclaimers indicating relative contributions of Christian Michael and the other authors of [10].

The authors for correspondence of [1], Mark Alber and G.V. Reddy, directed and supervised the research that formed [1] in addition to contributing to the research and preparation of the

manuscript. Mikahl Banwarth-Kuhn and Ali Nematbakhsh conceptualized the investigation in [1] and provided the initial model implementation code in C++ from [2]. Kevin Rodriguez, Alexander Plong, and G.V. Reddy designed and performed all experiments with *Arabidopsis*. Calvin-Khang Ta, Eric Bourgain-Chang, and Amit Roy-Chowdhury conceptualized and contributed to the implementation of all image analyses in this work. All members contributed in preparation of the listed manuscript.

For my mother, father, and brother, who helped me through the darkest of times. Your support allowed the completion of this marathon to become a reality.

And, for all of my dear friends in the program - Ben, Nick, Michael, Daniel, Xander, Jennifer, Jacob, Joe, Luke, Rebecca, and most everyone else - The friendship and moral support that you've given me is worth its weight in gold.

ABSTRACT OF THE DISSERTATION

Mathematical Modeling Study of the Impacts of Boundary Conditions and a Pseudo-3D Mechanism on the Maintenance of the Shoot Apical Meristem of *Arabidopsis thaliana*

by

Christian Thomas Michael

Doctor of Philosophy, Graduate Program in Mathematics
University of California, Riverside, September 2022
Mark Alber, Chairperson

Stem cell maintenance in multilayered shoot apical meristems (SAMs) of plants requires regulation of cell growth and division. Exactly how the milieu of chemical and mechanical signals interact in the SAM to regulate cell division plane orientation is not well understood. In this work, simulations using a 2D multiscale mathematical model are combined with experiments to suggest and test three hypothesized mechanisms for the regulation of cell division plane orientation and the direction of anisotropic cell expansion. Simulations predict that in the Apical corpus, WUSCHEL and cytokinin regulate the direction of anisotropic cell expansion, and cells divide according to tensile stress on the cell wall. In the Basal corpus, model simulations suggest dual roles for WUSCHEL and cytokinin in regulating the direction of anisotropic cell expansion and cell division plane orientation. This is supported by a detailed analysis of experimental images upon manipulation of WUSCHEL and cytokinin. Moreover, simulations predict that this layer-specific mechanism maintains the experimentally observed shape and structure of the SAM and the WUSCHEL distribution in the tissue. The 2D model is then extended to include expansion and division of cells out-of-plane to form a pseudo-3D (P3D) model. Both models include boundary conditions which represent tension experienced by the SAM epidermis. The P3D model maintains the epidermal cell monolayer crucial for development in wildtype SAMs. By comparing the behavior of the P3D and 2D models, it is shown that tension-guided cell division plane orientation acts to regulate cell and tissue shape distributions.

Contents

List of Figures

List of Tables

Chapter 1

Introduction

1.1 Study of the shape and structure of plant tissue

This section up to and including Subsection 1.1 includes, in part, reproduction of the introduction and motivation published in [1]. Though the first authors were Mikahl Banwarth-Kuhn and Kevin Rodriguez, I contributed substantially to the writing and revision of those sections in [1].

Deciphering how chemical signals and physical forces interact to regulate the overall size, shape, and organizational structure of a growing tissue is a central problem in the development of animals and plants. In contrast to their animal counterparts, plant cells are physically adhered to each other through their shared cell wall and do not move relative to one another during tissue growth and morphogenesis [3, 4, 5, 6, 7, 8, 9]. As such, the precise regulation of cell growth and division rates, polarization, and division plane orientation play critical roles in pattern formation and maintaining the size and shape of plant tissues. While recent studies suggest that cell shape and tensile forces alone are sufficient to explain patterns of cell division plane orientation in plant tissues [3, 10, 11, 12], most research in this area has been limited to the plant epidermis and does not consider the role of chemical signals in orienting the direction of anisotropic cell expansion and division plane orientation.

Division patterning must also be robust to mechanical perturbation since a living plant must be able to thrive when exposed to natural conditions. Even under ideal environmental conditions, a healthy plant must withstand perturbations to tissue patterning due to developmental processes. There are multiple examples in literature of tissues whose unique structure is directly related to their mechanical context on both a local and global scale, including organization of plants' epidermal pavement cells [13] and their xylem [14]. In this dissertation, we explore the interplay of chemical signals and mechanical stress in regulating cell division plane orientation and the direction of anisotropic cell expansion in the corpus of the shoot apical meristem (SAM) of *Arabidopsis thaliana*, as it provides an ideal system for studying cell behavior in a morphogenetic and physiological context.

The mechanisms underlying cell division in plants have been studied extensively [3, 10, 11]. For example, Errera's rule- which assumes that cells divide along the shortest new wall dividing the mother cell's volume in half- has been shown to successfully predict cell division plane orientation in tissues with locally spherical shape and homogeneous growth, such as the tunica layers of the central zone of the distal portion of the SAM [15, 10, 3, 16, 17]. However, recent experiments and computational studies indicate that anisotropic stress arising from heterogeneous growth (different between adjacent cells) and saddle-shaped regions of the SAM result in deviations to shape-based division rules [3, 11, 18, 12]. Louveaux et al. [3] explained these deviations by proposing that new cell walls orient along the local maximum of tensile stress on the mother cell wall. In either case, patterns of cell surface expansion in the SAM give rise to changes in cell shape and tensile forces that could influence the positioning of new cell walls. The challenge is to understand how chemical regulators such as the transcription factor-WUSCHEL (WUS) and plant hormone cytokinin (CK) interact with mechanical stress to control cell division plane orientation and maintain the layered organization and shape of actively growing SAMs.

1.1.1 Study of the interplay between chemical signaling and cellular mechanical properties

In Chapter 2 of this dissertation, I present the my contributions to the study that I participated in the paper [1]. We explored the interplay of chemical signals and mechanical stress in regulating cell division plane orientation and the direction of anisotropic cell expansion in the corpus of the shoot apical meristem (SAM) of *Arabidopsis thaliana*, as it provides an ideal system for studying cell behavior in a morphogenetic and physiological context.

In Section 2.1, we present our newly developed, biologically-calibrated, 2D multiscale computational model. Section 2.1 gives descriptions of metrics along with sensitivity and perturbation analysis approaches used for validation of the model and for comparison to experiments. In Section 2.3, selected results from [1] are presented focusing on the detailed justification for the layer-specific division plane mechanism.

Special focus is placed in [1] on the study of mechanisms which determine division planes in the model of SAM cells. Out of three hypothesized mechanisms, the first two assume the sole function of WUS and CK in regulating the direction of anisotropic expansion of cells, while the placement of new cell walls during division is determined according to either Errera's rule or local patterns of in-plane tensile stress on the cell wall. In contrast, the third mechanism assumes dual roles for WUS and CK in directly regulating both anisotropic cell expansion and cell division plane orientation. Chapter 2 ends with selected discussion points from [1], summarizing the results and predictions of the model. A general description of the combined multiscale modeling and experimental analysis method we used in [1] is provided in Figure 1.1.

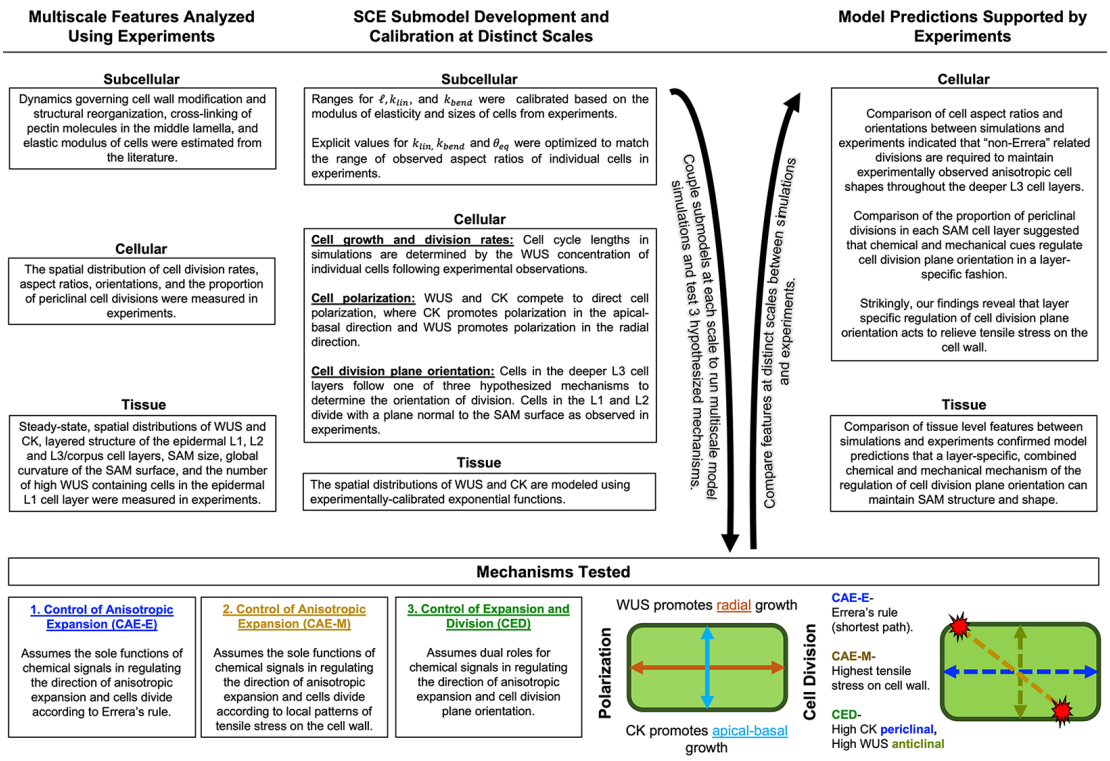

Figure 1.1: **Combined Multiscale Modeling and Experimental Study Workflow Outline**. Data from experimental studies was used to develop and calibrate submodel components at distinct scales. Multiscale model simulations were used to test three hypothesized mechanisms of the regulation of cell division plane orientation in the corpus. Results from perturbation experiments were used to support model predictions.

1.1.2 Development of a pseudo-3D model of the SAM and calibration of its boundary conditions

There are a multitude of signals known to influence the shape, size, and organization of the SAM though spatially-coordinated direction of cells' growth rate, direction of anisotropic expansion, and differentiation [19, 20]. It is unclear exactly where within these complex interactions mechanotransduction comes into play. Experimentally, it is challenging to determine whether a given hypothesized cell-scale mechanism is at play, as the complex and dynamic collection of interactions between cells within a tissue makes it difficult to determine what the emergent behavior of such a

cell-scale mechanism would have. Moreover, many experimental targets for genetic perturbations are upstream of multiple systems, and these experiments may easily have multiple confounding impacts due to modified downstream products.

To ameliorate this, many mathematical modeling techniques have been used to examine specific features of the SAM. One main subject of study is the epidermis of the SAM - cell layers L1 and L2, shown in Figure 1.3. For example, [21] studies how the division patterning of these clonally distinct layers serves to distribute tension isotropically across the SAM surface and minimize the reliance of the tissue upon any single cell for hormone transport. Vertex models have been used to study the L1 of the SAM [22], as well as a plethora of morphogenic phenomena in cell monolayers [23]. However, many models that have been used to investigate the SAM and similar systems have been two-dimensional [24, 22] the highest-resolution level of detail is cell-scale [25, 26].

In parallel, recent advancements in three-dimensional confocal microscopy have opened exciting possibilities. Such advances allow for detailed three-dimensional images to be taken of deep-layer tissue in the SAM to provide detailed high-resolution spatial data for model calibration and model prediction verification. Moreover, by adapting three-dimensional cell-scale segmentation methods such as spherical harmonic fitting, described in [27], we are able to accurately calibrate detailed multi-scale mechanistic models of the SAM. Moreover, biological findings support the idea that the epidermal layers of the L1 and L2 are under substantial tension, which may assist in coordinating organ-scale mechanical cues propagated through adhesion [28]. Our previous work [1] supports the idea that in the apical corpus of the SAM, mechanical cues are required for proper division plane patterning, but the stress exerted on the SAM by the surrounding tissue may impact this non-trivially.

In Chapter 3, we introduce and compare two detailed multi-scale mechanical models of the SAM. These models, which are extended from those in [1] (presented in Chapter 2), were developed to investigate the effect of experimentally calibrated boundary conditions on the shape and structure of the SAM. These models, 2D and pseudo-3D (P3D), differ from one another by the incorporation of

a stochastic, experimentally calibrated pseudo-3D submodel which represents cell anisotropy in three dimensions. The stochastic model components are calibrated to well-reproduce the heterogeneity of cell-scale behaviors observed in experiments, and avoids adding in any artifacts due to exclusively in-plane expansion/division of cells, and reduces model dependence on initial conditions. Calibration of the P3D submodel uses makes use of 3D segmentation of the SAM using the method of spherical harmonic segmentation described in [27].

We found that the inclusion of out-of-plane anisotropically expanded cells allows us to reveal the impact of biologically calibrated boundary tension on regulating the monolayered structure of the epidermal and subepidermal layers of the SAM. Conversely, we found that without out-of-plane cell expansion, cell-cell crowding dominates the distribution of mechanical stresses experienced by cells in the tunica. Lastly, we found that both 2D and P3D models simulations maintain similar distributions of cell and tissue shapes regardless of the magnitude of SAM boundary tension. We have shown, using model simulations, that this is due to the mechanically-driven cell division plane patterning in the apical corpus acting as a regulatory mechanism.

1.1.3 Organization of the thesis

This dissertation has been organized in the following manner. The Background sections of this chapter contain both mathematical and biological contexts for the computational methods and biological system studied in this dissertation, respectively. In Chapter 2, the mathematical model development chapter, contains a justification for the use and applicability of a 2D model of the longitudinal section, and a detailed presentation of each model component, as well as how they are coupled with one another. Chapter 2 also presents a portion of the analysis of this 2D model that was performed in parallel with experimental investigation in [1] to test multiple hypothesized mechanisms of the determination of division plane orientation in the corpus of the SAM. Chapter 3 presents novel models that extend this through the addition of pseudo-3D and boundary forces. We then present our comparisons between the models and their biological implications in the Computational Model

Predictions section. A general description of the implementation of all models and code availability are in Chapter 4. Chapter 5 contains experimental and image Analysis methods used for model calibration both in [1] and in my own work. Finally, Chapter 6 contains the conclusions of our studies of the pseudo-3D model, wherein we interpret the results and address potential broader impacts, and the differences in the models' predictive capabilities.

1.2 Mathematical and Computational Modeling Background

Mathematical models have been used to study biological processes for many years, but more powerful computers have been more readily available, the variety of computationally feasible modeling methods has expanded greatly. Cell behaviors can be incredibly complex and varied, and possess a diverse collection of important and mechanistically distinct behaviors. Any attempt to simulate the entirety of a cell with all known molecular dynamics, stochastic behavior, chemical interactions and mechanics is intractable not only because of the complexity, but analysis of such a model would be near-impossible to perform in any meaningful sense. Because of this, modern mathematical modeling approaches make an attempt to balance a few key factors, including the level of coarse-graining, computational efficiency (as most models include numerical solution of an ODE or PDE system [29, 30, 31, 32]), and parsimoniousness of the model. For example, an incredibly simple model may be very efficient, but be too simple to provide meaningful results. On the other hand, if the model is overly complex, analysis of the model is not straightforward and results may be caused by confounding factors.

1.2.1 Cellular Potts Models

The Ising model has been traditionally used for studying ferromagnetism [33]. It was generalized into what is now called the *Potts* model by Renfrey Potts in 1951[34]. Cellular Potts models (CPM) represent a biological cell as a cluster of nodes being assigned a particular multi-

dimensional index [35], and cell movement by randomly changing indices of nodes [36]. Nodes are chosen randomly at every iteration step to change an index according to a transitional probability, calculated using a *Hamiltonean* $\mathcal{H}$, or *energy*. Transitional probabilities are chosen to be

$$P(\text{transition is accepted}) = \begin{cases} e^{-c\cdot\Delta\mathcal{H}/T} & \Delta\mathcal{H} \geq 0; \\ 1 & \Delta\mathcal{H} < 0. \end{cases}$$

Here T is *temperature* and c is a constant.

In [35], Graner and Glazier introduced a Cellular Potts Model (CPM) where nodes in a cluster representing a biological cell have a multidimensional index representing its identity $\sigma = \{1, \ldots, n\}$, and a *type*, "light", "dark", or "medium", representing the type of cell. The Hamiltonean $\mathcal{H}$ incorporated an energy of adhesive interactions between populations of cells with distinct identities, causing cells on average to aggregate towards cells of the same type being clustered together[35]. CPMs were shown to be able to reproduce, by choosing different parameter values, a number of experimentally observed patterns of tissue structure [37].

In [36] and [38], a diffusion limit was applied to one-dimensional and two-dimensional CPMs of chemotactic cellular motion resulting in continuous PDE approximations of these models. The continuous limits of CPMs resulted in, among others, equations for the motion of cellular centers of mass in the form of classic Keller-Segel equations of chemotaxis [38]. The Keller-Segel model is a diffusion-advection PDE system which describes the time evolution of the spatial population density p of a motile chemotactic single-cell species whose motion is influenced by the local concentrations c of a chemoattractant. The system is given by

$$\partial_t p = D_1 \partial_x^2 p - \chi_0 \partial_x \left[p \partial_x c \right],$$

$$\partial_t c = D_2 \partial_x^2 c - \gamma c + ap;$$

where here χ_0 represents the sensitivity of the cell to the chemoattractant, γ is the rate of decay of the chemoattractant and a is the secretion rate of the chemoattractant by the cellular population.

The Keller-Segel model can capture phenomena observed in well known experiments such as the aggregation of *Dictyostelium discoideum* [39].

CPMs were incorporated into multi-scale models with several time and space scales of description of a biological process. A widely used computational platform based on the Cellular Potts model is CompuCell3D, which has been applied to simulate a plethora of biological phenomena [40, 41, 42, 43].

1.2.2 Vertex Models

A relatively straightforward approach to representing a collection of cells in a single layer (e.g. in most epithelial tissues) is a *vertex model*[23]. This is a model in which the tissue is described as a graph, i.e. a collection of vertices connected by edges with cells being represented by polygons which are defined by edges in the graph. In this framework, cells share membranes with their neighbors, and the motion of the cell is modeled by the motion of the vertices. Vertices are typically represented as being embedded in a viscous medium, and are assumed to have vanishing inertia. As such, an individual vertex's motion is governed by the following equation:

$$\eta \frac{d\boldsymbol{x}_i}{dt} = \frac{d\boldsymbol{F_i}}{dt}$$

where $\boldsymbol{x}_i$ is the position of vertex i, $\boldsymbol{F}_i$ is the sum of forces on node i, and η is a damping factor. Differences between vertex models are, in part, given the definitions of $\boldsymbol{F}$, the principle forces that primiarily drive motion of cells [23]. However, without special attention to junction rearrangements the topology, the tissue model representation is rather rigid, since defined edges results in each cell having a fixed set of neighbors. Since cell-cell interfaces are modeled by edges of a graph, capturing any phenomenon in which cells do not maintain a statis set of neighbor cells (e.g. one cell migrating through a tissue; tissue organization; cell division) requires the definition explicit rules for rearranging the graph. These rules must be chosen carefully to reflect the biological phenomena that they are representing.

One of the challenges is in deciding whether to allow the model tissue the capacity for more than three cells to be in contact with a single vertex, forming what is known as a *rosette*[23]. This was a phenomenon which was not thought to exist in epithelial tissue until it was documented by Blankenship et al. in 2006 [44]. Modeling graph rearrangements to allow for such a configuration to occur, and to only occur with experimentally observed frequency, could prove challenging. However, it is a challenge that is addressed in many works. This has since been addressed in works such as [45], and is an active area of study. The computational platform, VirtualLeaf, simulates plant tissue morphogenesis using an approach which is conceptually similar to the Cellular Potts model, yet bears similarities to the vertex model framework [46, 47, 48].

1.2.3 Subcellular Element Models

Although the vertex and Cellular Potts models are appropriate for modeling many aspects of cell processes and properties (e.g. proliferation of epithelial sheets [23]; complex adhesion interactions [36, 39]), it is often difficult to directly represent mechanical properties of a cell. In both CPM and vertex models, mechanical interactions are typically described by using abstract energy functionals [23, 49, 41]. The *Subcellular Element* (SCE) framework is designed to provide a detailed high-resolution coarse-grained representation of a molecular dynamics type for a cell and tissue. Though typically computationally intensive, SCE models may directly implement specific mechanical properties (e.g. elasticity of a material) which can be directly calibrated using experimental data. SCE models represent cells by heterogeneous sets of off-lattice nodes interacting with one another through simplified, yet biologically relevant potentials, representing mechanical and biological cell-cell and cell-ECM interactions. The ability to vary model parameters at the subcellular scale allows for the study of emergence of larger-scale tissue-level phenomena. In [2], a chemical signaling submodel was coupled with an SCE model to study anisotropic expansion of cells and a resultant curved tissue shape, observed in experiments.

Another example of the SCE model framework is presented in [50], where a two-dimensional (2D) model was used to determine a mechanism determining proper cell rounding and division in the imaginal wing disc in a *Drosophila* embryo. It is important to note that this biological system is appropriately modeled in two dimensions, since the wing disc is a single layer of cells (i.e. cell monolayer) with relatively constant height, and the relevant cellular machinery (i.e. the actomyosin cortex) is localized on the apical surface of the cell during division.

Other SCE type models are still being actively developed. Recently, PalaCell2D [51], was developed to study morphogenesis using a combination of explicit forces acting on nodes from extracellular sources (e.g. adhesion) and implicit, energy-minimizing forces to simplify the intracellular mechanics (e.g. cell area conservation).

Our group's studies focused on the interplay between chemical signaling and mechanotransduction phenomena in the SAM [1, 2]. In the recent paper [1] (with some results described in this dissertation), we used a SCE model to test a cell-scale mechanism controlling the orientations of division planes in the corpus being distinct between the apical and basal corpus. Whereas [1] provided insight in the behavior of the SAM Corpus, the monolayer structure of the epidermis of the SAM remained difficult to capture in simulations. The SCE model framework is particularly well-suited to investigate the impact of intra-cellular and cellular heterogeneity on tissue-scale structuring, especially when cell-scale behavior (e.g. placement of division planes) are driven by local mechanics (e.g. tension experienced by the cell wall). In this dissertation, we apply the SCE framework to create the 2D and pseudo-3D models of the SAM. These models are used to investigate how cells' responses to local mechanical stresses can regulate the distribution of cell shapes as well as tissue shape to provide robustness to boundary forces or cellular mechanical perturbations.

1.3 General Biological Background

1.3.1 Dependence of SAM organization on chemical signals and cellular mechanical properties

This subsection is a reproduction of the biological background presented in [10]. Though the first authors were Mikahl Banwarth-Kuhn and Kevin Rodriguez, I contributed substantially to the writing and revision of this subsection.

Traditionally, SAMs have been divided into distinct clonal layers and zones [52, 53, 54] (Figs 1.2A). The tunica consists of the outermost epidermal L1 layer and an inner sub-epidermal L2 layer. Both the L1 and L2 are composed of a single layer of cells that divide exclusively anticlinally (perpendicular to the SAM surface) ensuring that each layer remains one cell thick (Figure 1.2A). During development, the L3 cell layer, through periclinal cell divisions, forms into the multi-layered corpus, which we further separated into the Apical corpus and Basal corpus (Figure 1.2A). As such, rules governing the position of new cell walls are essential to maintain the clonally distinct layers, ensuring proper SAM organization during growth. While anticlines and periclines are traditionally used to quantify the patterning of division plane placement relative to the nearest tissue surface or sub-epidermal cell layers [55, 56], such definitions would present problems in the present work because we observe considerable variation in SAM shape between some of the more deformed mutant phenotypes (e.g. flat vs. enlarged meristems). Thus, for consistency across mutants, we define periclinal divisions in the corpus as those occurring perpendicular to the apical-basal axis of the SAM, and anticlinal divisions in the corpus as those occurring parallel to apical-basal axis (i.e. perpendicular to periclinal divisions) of the SAM [52] (see Figure 1.2A and Chapter 2 Section 2.2.3 for details).

In addition to this layered organization, the SAM is also subdivided into four distinct functional zones (Figure 1.2). The central zone (CZ) contains a set of stem cells that span the tunica and L3 cell layer. Within the CZ, stem cell progeny are pushed away laterally into the peripheral zone (PZ) where they begin expression of genes involved in differentiation. The organizing center

(OC) and rib meristem (RM) consists of stem cell progeny located beneath the CZ. Cells in the RM span the Basal corpus and gradually differentiate along the apical-basal axis to form the stem of the plant. Amidst this process of constant displacement and subsequent differentiation, the relative numbers of cells in each zone are maintained, requiring precise spatial and temporal regulation of both SAM growth and gene expression [57].

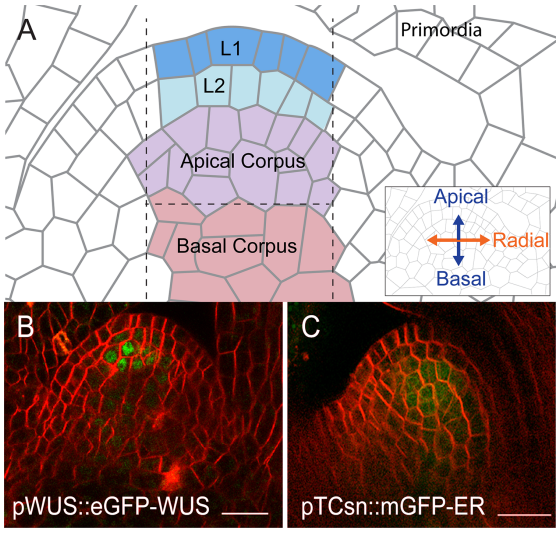

Figure 1.2: **Organizational structure of the SAM**. (A) Diagram showing a median longitudinal section of the SAM and depicting three distinct clonal layers. The tunica encompasses the L1 and L2 cell layers. The corpus is subdivided into the Apical corpus and Basal corpus. Vertical dashed lines represent the outer edges of the region used in experimental analysis. The horizontal dashed line represents the separation between the Apical corpus and Basal corpus. The L1 (blue), L2 (light blue), Apical corpus (purple), and Basal corpus (red) cells that fall within the region used for experimental analysis. These limits were manually determined for each experimental SAM image. (B) Median longitudinal section of the SAM showing the WUS protein domain *(pWUS::eGFP-WUS)* in a 9 day old SAM. (C) Median longitudinal section of the SAM showing the cytokinin signaling reporter *(pTCSn::mGFP5-ER)* in a 9 day old SAM. eGFP-WUS and mGFP5-ER (green) are overlaid on FM4-64 plasma membrane stain (Red). Scale bars = 20 μm.

Genetic analysis has revealed the importance of several chemical regulators in SAM growth and stem cell maintenance [58, 59, 60, 61, 62, 63, 64, 65]. In particular, the homeodomain transcription factor (TF)- WUSCHEL (WUS) and the plant hormone cytokinin (CK) have been shown to regulate SAM size, shape, and the number of stem cells [66, 61, 67, 68, 69]. *WUS* expression

domain and size is confined to the OC in part through a negative feedback loop by CLAVATA3 which represses radial and apical expansion of *WUS* expression. In addition, a new regulatory loop has been proposed through CLE40, a PZ diffused signaling peptide, which maintains the WUS domain by promoting *WUS* expression through an unknown non-cell-autonomous signal [70]. The WUS protein migrates into adjacent cells to form a concentration gradient (Figs 1.2B and Fig 3 in [1]). The concentration gradient resulting from this regulation has been shown to stabilize, i.e. it maintains a steady-state distribution within the tissue, and it moves upward with the growing distal portion of the SAM [68, 19].

Additionally, CK is perceived by a family of histidine kinase receptors localized in the RM, thus restricting the CK response to these cells as revealed by the CK signaling reporter-pTCSn [71, 72] (Figs 1.2C and Fig 3 in [1]). CK signaling has been shown to stabilize the WUS protein thus regulating the WUS gradient [68]. Consistent with this observation, ectopic activation of CK signaling results in taller SAMs [68]. Despite the central importance of WUS and CK in regulating SAM growth and stem cell maintenance, their precise roles and interaction in controlling cell division plane orientation in the RM is poorly understood.

1.3.2 Biological background for the study of epidermal tissue tension and 3D effects on tissue structure

The shape and structure of the SAM is maintained throughout the life of a plant [73, 74]. Composing the SAM is the tunica, comprising two clonally-distinct layers of epidermal and sub-epidermal stem cells. The maintenance of the layered structure is crucial for the continued development of the plant, since each layer will produce different cell types; failure to maintain structural arrangement of this tissue will result in the misplacement of organs in the tissue. In *lom* triple mutants, incorrect maintenance of layered structure results in premature termination of the meristem which prevents the continued growth of the plant.

Below the tunica is the corpus, which does not have layered structure (Figure 1.3 C), though the growth and division patterns are known to be controlled by the plant hormones WUSCHEL and cytokinin. Because all cells are tightly adhered, the ability for the plant to maintain the shape and structure of the SAM depends entirely on cell-scale anisotropic expansion directions and cell division orientations. Our previous work investigated division patterning in the corpus of the SAM, wherein we found evidence of a qualitative difference in cell division plane placement between the apical and basal regions of the corpus [1] (also presented in Chapter 2).

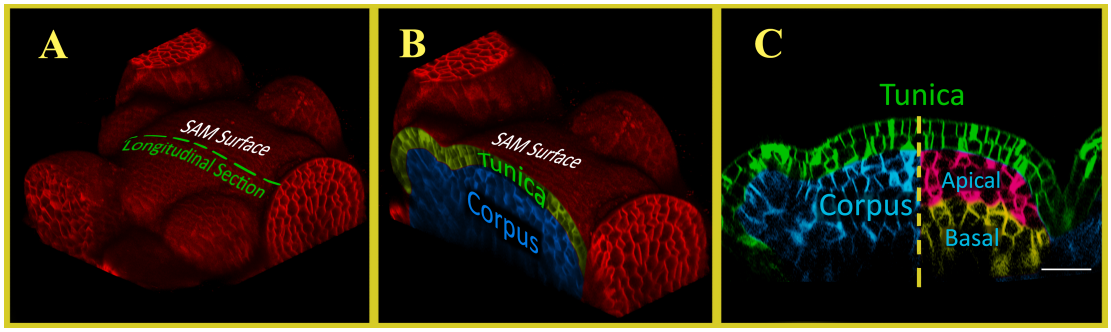

Figure 1.3: **Shape and layered structure of the SAM** (A) 3D confocal micrograph of the SAM and surrounding primordia of Arabidopsis thaliana. Cell walls are stained in red. A longitudinal sectional contour taken through the SAM apex is illustrated. (B) Longitudinal section taken of the SAM and adjacent tissue, shown in the context of the 3D tissue. Tunica and corpus are labeled in green and blue, respectively. (C) Longitudinal section of the SAM taken from the previous panel. The SAM is flanked by newly forming primordia. Larger cells below the SAM are expanded, indicating they have begun differentiation. The tunica of the SAM (green cells) comprises two clonally distinct monolayers layers of cells. The corpus of the SAM is rendered in blue (left), and (right) is subdivided into the apical corpus (red) and basal corpus (yellow). Scale bar is $20\mu m$.

Experimental procedures have elucidated many of the key factors in the maintenance of the SAM, both from a mechanical and chemical perspective. Techniques such as atomic force microscopy have examined the spatial distribution of the SAM surface via mechanical perturbations [75]. The impact of signaling on the spatial patterning of both the cell and organ scale size and structure of the SAM has been an active area of research [76, 73, 77, 78]. The critical role of auxin in phyllotaxis patterning and the regulation of auxin itself has been an active area of research as well [79, 80].

Multiple levels of control have been shown to spatially regulate the tissue structure of the SAM and signals therein, such as the active degradation of WUS and CK deeper inside of the SAM by *HAIRY MERISTEM* [81], the transportation of auxin by *PIN* and its downstream transport proteins [82].

Our previous work [1] sought to understand the role of mechanics on tissue structure by employing two-dimensional subcellular element (SCE) models. Advantages of the SCE model are in its ability to mechanistically model heterogeneity within a cell to analyze the emergent tissue-scale impact of such heterogeneity, as in [1, 2]. While our work in [1] (and presented Chapter 2) established that parallel longitudinal cross-sectional slices of the SAM were similar enough to merit a two-dimensional approach [1], such an approach does not account for effects that may be acting perpendicular to the longitudinal cross-section that was modeled. Though the two-dimensional SCE remains a good choice for investigating mechanical cues that are spread across a tissue, the intrinsically three-dimensional nature of the SAM's deep layers makes the impact of three dimensional organization difficult to study.

Chapter 2

Description of the Mathematical Model and Model Simulation Results

This chapter is a reproduction of the model description presented in [1]. Though the first authors were Mikahl Banwarth-Kuhn and Kevin Rodriguez, I contributed substantially to the implementation, analysis, writing, and revision of this work. I also substantially towards design and creation all figures and their captions presented in this chapter, in collaboration with Mikahl Banwarth-Kuhn in their revision. It should be noted that the models in this chapter and Chapter 3 are based on the same subcellular element model approach, but are substantially different. The model in Chapter 2 is two-dimensional, and the model in Chapter 3 is pseudo-3D and has a detailed description of boundary forces. The notations used are substantially different between this chapter and Chapter 3. I independently developed the models in Chapter 3.

2.1 2D Mathematical Model of Plant Tissue Maintenance

2.1.1 Mathematical Model Development

To study the interplay between chemical regulators and mechanical stresses in directing underlying cell behaviors and maintaining SAM structure and shape, we developed a detailed, multiscale, 2D computational model and calibrated it using experimental data. The model uses the subcellular element (SCE) computational framework to simulate a two-dimensional (2D) longitudinal section of the central region (as depicted in Figure 1.2A) of a growing SAM (see Figure 2.10, S1, S2, and S3 Videos of [1] for typical simulation output, and Section 2.2 for details on model initial and boundary conditions). The SCE modeling approach is a well-established, coarse-grained simulation framework for determining the impact of local biophysical and biochemical processes on emergent cell and tissue scale properties of growing or deforming multicellular tissues [83, 84, 85, 86, 87, 88, 89, 90, 91, 92, 93, 94].

The novel, 2D, multiscale, SCE model described in this chapter (reproduced from [1]) represents cells using two types of nodes- internal/cytoplasmic and external/cell wall nodes- that interact via different potential functions. Such biologically calibrated interactions between nodes simulate mechanical properties of plant cell walls facilitating novel predictions of how cell wall mechanics can help regulate the direction of anisotropic expansion of cells, and cell division plane orientation (see Figs 1.1 and 2.1, and Section 2.2 for details). Furthermore, an important distinction between our previous modeling approach [83] and the computational model presented in this chapter (reproduced from [1]), is the introduction and detailed testing of novel hypothesized mechanisms regulating cell division plane orientation and the modification of cell wall properties leading to anisotropic cell surface expansion (see Section 2.1.4 and Section 2.2 for details). Both of these processes are thought to play an important role in emergent cell and tissue level properties of the SAM. In what follows, we provide a detailed description of the development, calibration, and

implementation of SCE submodel components at distinct scales and how they are coupled to run multiscale simulations of SAM growth.

2.1.2 Submodel of mechanical properties of cells and cell-cell interactions

Individual cells are modeled by a heterogeneous collection of wall nodes and internal nodes (shown in Figure 2.1A and 2.1B). Interactions between nodes represented via Morse and linear spring type potentials as in [83]. In particular, each cell i has N_i wall nodes W_i^j (for $j = 1, \dots N_i$) and M_i internal nodes I_i^j (for $j = 1, \dots, M_i$). The potential functions E in Eq 2.1-2.2 represent specific biological features of plant cells (described in detail below) and are used in the model to calculate the displacement of each internal or cell wall node at each time step based on their interactions with neighboring nodes. The Langevin equations of motion used in the model are as follows:

$$\eta_i \frac{d}{dt} W_i^j = -\sum_{k=1}^{M_i} \nabla E^{IW}(W_i^j, I_i^k) - \nabla E^{WWS}(W_i^j, W_i^{j\pm 1}) \\ - \sum_{\text{cells } l} \sum_{k=1}^{N_l} \nabla E^{WWD}(W_i^j, W_l^k) - \sum_{\substack{\text{adhesion} \\ \text{neighbors of cell } k}} \nabla E^{Adh}(W_i^j, W^k) \tag{2.1}$$

$$\eta_i \frac{d}{dt} I_i^j = -\sum_{k=1}^{M_i} \nabla E^{II}(I_i^k, I_i^j) - \sum_{k=1}^{N_i} \nabla E^{IW}(W_i^k, I_i^j), \tag{2.2}$$

where η_i is a cell's damping coefficient. The Morse potential functions E^{II} and E^{IW} together represent coarse-grained cytoplasmic forces and resulting turgor-pressure of cells. The Morse potential function E^{WWD} represents volume exclusion of neighboring cells. Pairwise linear spring interactions (E^{Adh}) between cell wall nodes of adjacent cells function as a coarse-grained model for cross-linking of pectin molecules in the middle lamella. The potential function E^{WWS} governs interactions between cell wall nodes of the same cell and is used to represent mechanical stiffness and extensibility of the primary cell wall. These functions comprise both linear and rotational spring potentials, as well as Morse potentials, given by:

$$
\begin{aligned}
E^{WWS}(W_i^j, W_i^{j+1}) = & \underbrace{\frac{1}{2}k_{\text{lin}}\left[\left(\left|W_i^{j+1} - W_i^j\right| - \ell\right)^2 + \left(\left|W_i^{j-1} - W_i^j\right| - \ell\right)^2\right]}_{\text{Linear spring potential}} \\
& + \quad \underbrace{\frac{1}{2}k_{\text{bend}}\left(\theta - \theta_{\text{eq}}\right)^2}_{\text{Rotational Spring Potential}} \quad , \\
E^{IW}(W_i^k, I_i^j) = & \underbrace{\left[U^{IW}\exp\left(-\frac{\left|W_i^k - I_i^j\right|}{\xi^{IW}}\right) - W^{IW}\exp\left(-\frac{\left|W_i^k - I_i^j\right|}{\gamma^{IW}}\right)\right]}_{\text{Turgor Pressure}}, \\
E^{WWD}(W_i^j, W_l^k) = & \underbrace{\left[U^{WWD}\exp\left(-\frac{\left|W_i^j - W_l^k\right|}{\xi^{WWD}}\right) - W^{WWD}\exp\left(-\frac{\left|W_i^j - W_l^k\right|}{\gamma^{WWD}}\right)\right]}_{\text{Volume Exclusion}}, \\
E^{Adh}(W_i^j, W^k) = & \underbrace{\frac{k_{\text{Adh}}}{2}\left(\left|W_i^j - W^k\right| - \ell^{\text{Adh}}\right)^2}_{\text{Cell-Cell Adhesion}}, \\
E^{II}(I_i^k, I_i^j) = & \underbrace{\left[U^{II}\exp\left(-\frac{\left|I_i^k - I_i^j\right|}{\xi^{II}}\right) - W^{II}\exp\left(-\frac{\left|I_i^k - I_i^j\right|}{\gamma^{II}}\right)\right]}_{\text{Cytoplasm Pressure}}
\end{aligned}
\tag{2.3}
$$

where $W_i^{j\pm1}$ denotes the positions of the nodes adjacent to node W_i^j, and θ is the angle formed by the lines $\overline{W_i^j W_i^{j+1}}$ and $\overline{W_i^j W_i^{j-1}}$. Ranges for the parameters k_{bend},k_{lin},θ_{eq}, and ℓ were calibrated based on the modulus of elasticity, sizes, and shapes of cells measured in experiments (see Section 2.1.4 and Section 2.2 for details on sensitivity analysis and calibration of these parameters). The Morse parameters ξ^*, γ^*, U^* and W^* were chosen based on coarse graining resolution and discussed in [83, 95]. In simulations, the exact values used for these parameters are dynamic and change in response to a probability distribution function parameterized by the amount of signal (WUS and CK) present in the cell at a given time (see Section 2.1.4 for details). The explicit parameter values for all other potential functions were calibrated in previous work [83, 95].

Each simulation represents 40 hours of tissue growth. The Euler numerical scheme was used for solving Eqs 2.1 and 2.2. The time step Δt was chosen to be 0.4 seconds to maintain stability

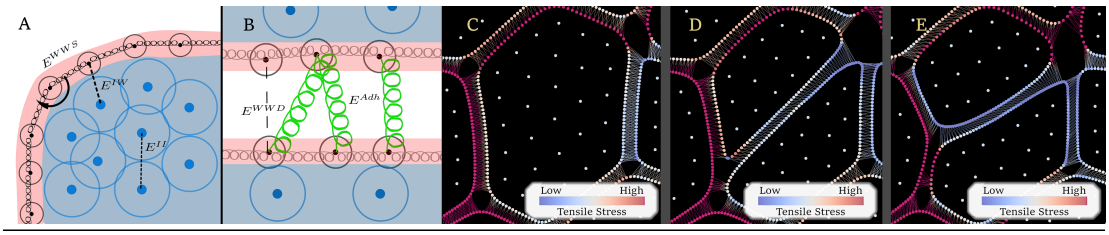

Figure 2.1: **Two-dimensional multi-scale model of SAM growth and maintenance.** Simulated cells are represented by two collections of nodes: cell wall nodes (solid black dots in the red region in A and B) and internal nodes (solid dark blue dots in the blue region in A and B). (A) Adjacent wall nodes of the same cell are shown interacting via linear and rotational springs given by E^{WW} that represent mechanical stiffness and extensibility of the primary cell wall. Pairs of internal nodes and internal and cell wall nodes of the same cell are shown interacting via Morse potential functions given by E^{II}, E^{IW} that represent cell turgor-pressure. (B) Wall nodes of neighboring cells may form adhesion partners and interact via a linear spring potential given by E^{Adh} that represents the adhesive properties of the middle lamella. Wall nodes of adjacent cells enforce cell-cell volume exclusion via Morse potentials given by E^{WWD}. The division process in the model is demonstrated in C-E, with the cell on display dividing in response to in-plane tensile stress. The heat map shown in C-E represents in-plane tensile stress tensile stress on each node where warmer colors represent nodes under higher tensile stress, and cooler colors represent nodes under lower tensile stress. (C) A simulated cell nearing mitotic phase. (D) A pair of simulated cells shortly after division. Cytoplasm nodes are redistributed within the daughter cells and adhesion partners of each wall node are updated. (E) The same cells as in D after an elastic relaxation phase occurs.

of the numerical scheme. Growth rates and cell cycle lengths are discussed in more detail in the Section 2.1.3.

2.1.3 Chemical signal distribution submodel controls growth of cells

The concentrations of WUSCHEL ([WUS]) and cytokinin ([CK]) for individual cells are assigned using the experimentally-calibrated exponential functions given in Eqs 2.4 and 2.5. While multiple feedback loops are known to regulate WUS and CK at both the transcriptional and protein levels, their net effect has been shown to result in steady-state distributions of WUS and CK in the SAM [19, 68]. Thus, Eqs 2.4 and 2.5 in the model were calibrated based on the steady-state distributions of WUS and CK measured from experimental images as in [83], by neglecting the mechanism underlying the establishment of such gradients. These functions describe the concentrations of WUS and CK as being distributed with radial symmetry about a dynamically determined point, the *signal center*, which represents the middle of the signals' expression domains. Values of [CK] in L1 and L2 are maintained at 0, since in wildtype SAMs these cells do not show CK responsiveness, which is likely due to the limitation of the CK reception system [71, 72]. Concentrations for WUS, as well as concentrations for CK in the corpus, are independently calculated using the expressions:

$$[\mathrm{WUS}] = [\mathrm{WUS}]_0 \exp\left(-\mu_{\mathrm{WUS}}(r_{\mathrm{WUS}} \cdot \alpha_{\mathrm{WUS}})\right); \tag{2.4}$$

$$[\mathrm{CK}] = [\mathrm{CK}]_0 \exp\left(-\mu_{\mathrm{CK}}(r_{\mathrm{CK}} \cdot \alpha_{\mathrm{CK}})\right), \tag{2.5}$$

where r_{WUS} and r_{CK} are the distance from the centroid of each cell to the WUS and CK signal centers, respectively.

In experiments, the WUS and CK expression domains are located below the distal portion of the SAM, heuristically described as being located two and three times the length of the average cell diameter beneath the distal portion of the SAM, respectively (Figure 2.2B and 2.2C). We established the signal center locations for WUS and CK similarly in simulations, setting them as two

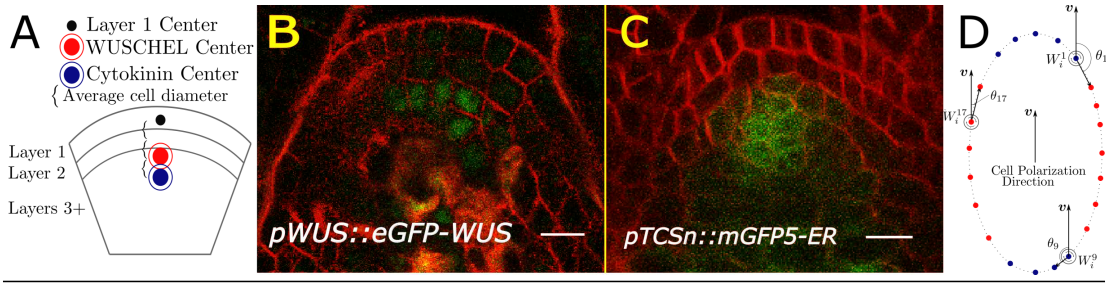

Figure 2.2: **Chemical signaling submodel of the SAM.** (A) Schematic of model signal expression domains of WUSCHEL and cytokinin. (B-C) Wildtype SAM longitudinal section image. Cell walls (red) outline the dome-shape of the SAM; reporters (green) indicate presence of the WUSCHEL protein (B) and cytokinin reporter (C). (B-C) Contrast was manually increased in the red channels for visibility. Scale bars are $10\mu m$. (D) Cell growth direction polarization $\boldsymbol{v}$ is dependent upon signaling. Wall nodes of a model cell polarized in direction $\boldsymbol{v}$ are illustrated. The angle θ_j between $\boldsymbol{v}$ and the vector connecting W_i^j to W_i^{j+1} are used to partition the wall nodes into sides (red) and ends (blue).

and three times the average diameter of the tunica cells, respectively, directly below the centroid of the central L1 cell (Figure 2.2A). The signal centers are updated dynamically throughout the course of simulations to ensure that the center of the WUS and CK expression domains in simulations maintain their position relative to the growing distal portion of the SAM, as observed in experiments. Parameters μ_{WUS}, μ_{CK}, $[\text{WUS}]_0$, and $[\text{CK}]_0$ were fitted to experimental wildtype data in [83] for $\alpha_{\text{WUS}} = 1$ and $\alpha_{\text{CK}} = 1$. Parameters $[\text{WUS}]_0$, $[\text{CK}]_0$, α_{WUS}, and α_{CK} were then perturbed to simulate under/over-expression or ectopic distribution of signals corresponding to experimental mutant conditions.

In simulations, individual cell cycle lengths (the amount of time between two successive divisions of an individual cell) are dynamically assigned based on the current WUS concentration of individual cells as in [83]. The cell cycle length is chosen using a normal distribution parameterized by [WUS], and calibrated using experimental data (data from [59]; calibration method as in [83]). New cytoplasm nodes are added linearly in time until the cell divides upon having 30 internal nodes. The process of division is detailed in subsection 2.1.5.

2.1.4 Dependence of cell growth direction polarization and direction of anisotropic expansion on competing signals

Cells in the SAM experience turgor-pressure driven expansion, and the orientation and level of alignment of microfibril bundles within the cell wall can promote preferential cell expansion along one axis of a cell [96, 8, 97]. We refer to this phenomenon as *growth direction polarization*, which we capture by making the stiffness and equilibrium angle of the cell wall's rotational springs heterogeneous across wall nodes in a cell (Figure 2.2D). Cells that are growing on the simulation boundary grow isotropically, so the rotational spring parameters are chosen to be uniform. All other cells do so anisotropically, detailed below.

Model signals of WUS and CK compete to direct cell growth direction polarization, where CK promotes growth direction polarization in the apical-basal direction and WUS promotes growth direction polarization in the radial direction. Each cell's growth direction polarization is signal-determined as in Section 2.1.6. We then set the stiffness and equilibrium angle of the rotational spring for E^{WWS} (see Eq 2.3) heterogeneously across the cell's wall nodes, representing microfibril-bound wall nodes (sides) and freely growing wall nodes (ends) as in Figure 2.2. The side nodes (red) have a much stiffer rotational spring, $k_{\text{bend}^{\text{high}}}$, whose equilibrium angle is set to π (flat), while the ends (blue) have a much looser rotational spring, $k_{\text{bend}^{\text{low}}}$, whose equilibrium angle set to prefer a circular arrangement - i.e. $\frac{\pi(N_i-2)}{N_i}$ where N_i is the number of wall nodes possessed by cell i. The explicit values of the rotational spring stiffness coefficients,$k_{\text{bend}^{\text{high}}}$ and $k_{\text{bend}^{\text{low}}}$, were determined via a sensitivity analysis optimizing the range of observed areas and aspect ratios of individual cells in single-cell simulations to the range of areas and aspect ratios measured in wildtype experiments [95] (see Table 2.2 in Section 2.2.2 for exact parameter values and Section 2.2.4 for more details on sensitivity analysis studies).

2.1.5 Dependence of cell division plane orientation on chemical regulators and in-plane tensile stress

When model cells complete a mitotic cycle (i.e. reach 30 internal nodes), they divide. Layer 1 and 2 cells are always prescribed to divide with a plane normal to the SAM surface as observed in experiments. To do this, we defined anticlinal division planes to be perpendicular to the line segment connecting its in-layer neighbors' cell centers. In the corpus, each simulated meristem follows one of four hypothesized mechanisms determining the position of the planes of division. The individual mechanisms are described in the following subsections.

Following the choice of division plane, two daughter cells are formed. These daughter cells are created out of the mother's original wall nodes and redistributed cytoplasm nodes, as well as new cell wall nodes along the division plane which represent the new cell wall and middle lamella. These newly formed cells are adhered to one another (Figure 2.1C- 2.1E).

Cell division based on Errera's Rule (CAE-E mechanism). Errera's rule states that the division plane chosen for a cell should result in the shortest possible cell wall [21]. This method selects the plane passing through the pair of nodes that minimizes the distance $\left\|W_i^j - W_i^k\right\|$ while evenly dividing the cell's area ($0.9 \leq \frac{A_1}{A_2} \leq 1.11$).

Cell division based on in-plane tensile stress (CAE-M mechanism). The in-plane tensile stress S on a cell wall element W_i^j is calculated as the average mechanical force exerted on it by its neighbors in the tangential direction, as follows:

$$\begin{aligned} S_{i,j} = &\frac{1}{2}\cdot \left\| \text{Proj}_{\boldsymbol{\tau}} \left(\frac{W_i^j - W_i^{j-1}}{\left\|W_i^j - W_i^{j-1}\right\|} k_{\text{lin}} \left(\left\|W_i^j - W_i^{j-1}\right\| - \ell \right) \right) \right\| \\ &+\frac{1}{2}\cdot \left\| \text{Proj}_{\boldsymbol{\tau}} \left(\frac{W_i^j - W_i^{j+1}}{\left\|W_i^j - W_i^{j+1}\right\|} k_{\text{lin}} \left(\left\|W_i^j - W_i^{j+1}\right\| - \ell \right) \right) \right\|, \end{aligned} \tag{2.6}$$

where denote $\boldsymbol{\tau}$ as a unit vector tangent to the surface of the cell, W_i^j is the node's location as 2D a vector, and ℓ and k_{lin} are the equilibrium length and stiffness of the linear spring part of

E^{WWS} (see Eq 2.3). We then calculate $S(W_i^j)$ for all wall nodes in the cell and select location of the maximally stressed wall node as one point on the division plane. The second node defining the division plane is chosen so that the cell area divides evenly ($0.9 \leq \frac{A_1}{A_2} \leq 1.11$). We observe in simulations that the distribution of in-plane tensile stress along the cell wall is smooth, and the largest variation in stress is near cell wall junctions. In most cases, the node experiencing maximal tensile stress is indicative of a local region of high tensile stress around that node, demonstrating that a single-node based selection method is sufficient for the CAE-M mechanism. While our model is in 2D, an analogous approach could be used for a 3D model as described in Section 2.2.

Cell division based on chemical signals (CED mechanism). Under this mechanism, cells under relatively high levels of CK are more likely to divide periclinally, and cells under the influence of WUS will likely divide anticlinally. The anticlinal versus periclinal behavior of the cell is determined by the probability distribution described in the Section 2.1.6. If the cell divides periclinally, the cell area divides evenly ($0.9 \leq \frac{A_1}{A_2} \leq 1.11$) with a horizontal plane; otherwise it divides anticlinally - that is, evenly divided and with a vertical plane.

Layer-specific combined chemical signaling and mechanical mechanism. In this mechanism, cells whose lineage are traced back to the third and fourth layers of the initial conditions divide according to the CAE-M mechanism, as in the Section 2.1.5. Cells in layers below that divide according to the CED mechanism, as in the Section 2.1.5.

2.1.6 Stochastic antagonistic signaling between WUSCHEL and cytokinin.

Two novel hypothesized mechanisms we tested using our model include 1) whether WUS and CK can regulate cell growth direction polarization and 2) how WUS and CK regulate cell division plane orientation. Thus, in our model, cell behavior is influenced by WUS to expand and divide anticlinally and by CK to expand and divide periclinally. However, we assume that every cell responds to these competing signals with some uncertainty - abstractly representing any

heterogeneity in the cells' sensitivity to the signal. To represent this, we use the relative signal - the ratio of WUS signal in a cell to the CK signal in a cell - to parameterize the probability distribution used to determine cells' behavior.

More specifically, noise in the competition between WUS and CK is modeled by considering the ratio $\lambda = [\text{CK}]/[\text{WUS}]$ as a parameter for a probability mass function:

$$\text{Prob(Cell follows periclinal behavior)} = \frac{1}{1 + \left(\frac{K_{\text{Hill}}}{\lambda}\right)^{N_{\text{Hill}}}};$$

$$\text{Prob(Cell follows anticlinal behavior)} = 1 - \left[\frac{1}{1 + \left(\frac{K_{\text{Hill}}}{\lambda}\right)^{N_{\text{Hill}}}}\right].$$

K_{Hill} was calculated by imposing that the midpoint between the signaling domains (Section 2.1.3) have equally probable anticlinal and periclinal behavior, and as such $K_{\text{Hill}} \coloneqq [\text{CK}]/[\text{WUS}]\big|_{\boldsymbol{x}=\text{Signal Center}}$. The value of N_{Hill} was fitted experimentally to experimentally observed anticlinal-periclinal division ratios under wildtype conditions.

2.2 Additional model and model analysis components

This section up to and including Section 2.2.4 is a reproduction of the extended model description presented in the S3 appendix of [10]. Though the first authors were Mikahl Banwarth-Kuhn and Kevin Rodriguez, I wrote and revised this technical description of model with direction and guidance from Mark Alber, Weitao Chen, and Mikahl Banwarth-Kuhn. In particular, I primarily developed and implemented subsections 2.2.2-2.2.3 and 2.2.5 equally with Mikahl banwarth-Kuhn. I performed the sensitivity and perturbation analyses in section 2.2.4.

2.2.1 Model Parameters

Table 2.1 provides parameter values used in simulations. The μ_* and $[*]_0$ values for WUS and CK were experimentally fitted in [2]. Values for α_X were defined to be 1 for wildtype, and varied by factors that replicated observed [CK] : [WUS] ratios. Ranges of model parameters controlling me-

chanical stiffness and extensibility of the primary cell wall (k_{lin}, ℓ, $k_{\text{bend}}^{\text{loose}}$, and $k_{\text{bend}}^{\text{stiff}}$) were calibrated in [2, 95] so that the modulus of elasticity (E) of cells lies within the biological range. Additionally, global sensitivity analysis was used in [95] to quantify the impact of each of these parameters on the area and aspect ratio of cells in simulations. Then the parameters with the most impact on these two cell-level features were fit based on the area and aspect-ratio of cells measures in experiments. There are many other parameters of the model, e.g. parameters controlling the strength of cell-cell adhesion and for coarse-graining parameters, which have been described previously in [2, 95].

Table 2.1: **Main parameter values for simulations.** Parameters that varied in *in-silica* experiments.

Parameter	Value	Interpretation	Chosen by
μ_{WUS}	0.01573 a.u.	Exponential fitting parameter	Calibrated in [2]
μ_{CK}	0.01637 a.u.	Exponential fitting parameter	Calibrated in [2]
α_{WUS}	0.4-1.5 a.u.	Ectopic misexpression factor	See Methods
α_{CK}	0.4-1.5 a.u.	Ectopic misexpression factor	See Methods
$[\text{WUS}]_0$	84.6 a.u.	Maximum WUSCHEL intensity	Calibrated in [2]
$[\text{CK}]_0$	110 a.u.	Maximum cytokinin intensity	Calibrated in [2]
N_{Hill}	10 a.u.	Steepness of stochastic threshold. Deterministic as $N_{\text{Hill}} \to \infty$.	See Methods
K_{Hill}	1.3 a.u.	[CK]/[WUS] yielding even CK-WUS competition	See Methods
ℓ	0.9 μm	Coarse graining parameter; linear spring equilibrium length	Calibrated in [2]
k_{lin}	280 $\frac{nN}{\mu m}$	Cell wall extensibility	Calibrated in [2, 95]
$k_{\text{bend}}^{\text{loose}}$	4.543 $\frac{nN}{\text{rad}}$	Loose wall bending spring constant - See Methods	Calibrated in [2, 95]
$k_{\text{bend}}^{\text{stiff}}$	13.5 $\frac{nN}{\text{rad}}$	Stiff wall bending spring constant - See Methods	Calibrated in [2, 95]
θ_{eq}	π or $\frac{\pi(N_i-2)}{N_i}$ rad	Equilibrium rotational spring angle	See Methods

2.2.2 Initial and Boundary Conditions

The initial "wedge" shape of the tissue (see Figure 2.3, panel A) and the initial number of cells in each layer used as the geometry input for model simulations were calibrated based on previously published results by our group [98]. These results provide average measurements of the central zone of the SAM, indicating that the number of central zone cells in Layer 1 is between 7-9

cells and decreases in a wedge-like shape across the next 3 layers. Additionally, we verified using this data that variability in both the "wedge" shape of the tissue and the number of cells in each layer is low. Our model simulates a 2D longitudinal section of the central region of the SAM (as depicted in Chapter 1 Figure 1.2 A) that includes the central zone together with the organizing center and rib meristem. So, we start each simulation with 10 cells each in the first layer, where the outermost cell on each side acts as a boundary cell (see below), and include 4 additional corpus layers encompassing the organizing center and rib meristem (see Figure 2.3, panel A and panel C of Fig A in S1 Appendix of [1]). The staggered configuration of cells is used to minimize the number of four-cell rosettes (as very few are observed in experiments [99]). To ensure that our precise tiling did not meaningfully impact simulations, we performed a perturbation analysis which is described in section 2.2.4 below.

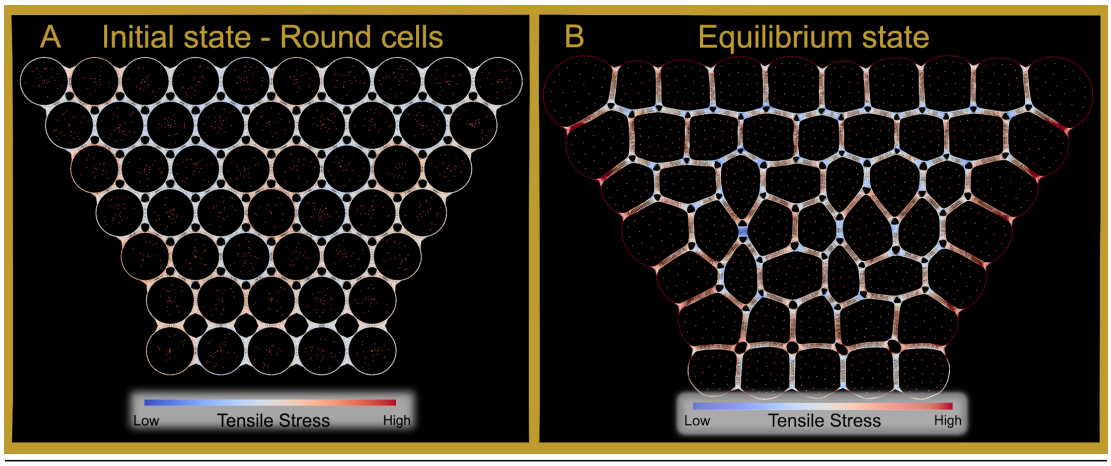

Figure 2.3: **Initial conditions and equilibrium state.** (A) 50 model cells and their initial adhesion connections between neighboring cell wall nodes are shown in the initial layout used for each simulation. (B) An example of an equilibrium state achieved after stage one of simulations. Note that in the equilibrium state, each cell has been stochastically assigned a direction of cell growth polarization, leading to anisotropically expanded cells at mechanical equilibrium. (A-B) Cells on the left and right sides of the simulated tissue domain are the boundary cells which do not divide in any stage of the simulation, but otherwise obey the same rules as other cells. Cells in the bottom most layer are considered part of the stem, and have a much higher damping to provide a foundation for the expansion of the SAM. The heat map shows the distribution of in-plane tensile stress as calculated in equation (2.6).

To model the tissue boundary, a single layer of cells at the bottom and sides of this configuration do not divide during the simulation to act as a boundary, representing the neighboring cells around the CZ. Cells beneath the simulated region are assumed to be differentiating and expanding, and act as a barrier to prevent downward expansion of the SAM. We capture this by giving the bottom-most layer of cells a higher damping coefficient ($\eta_i = 10$ for cells i in the deepest layer) compared to all other cells ($\eta_i = 1$). Each cell is initialized as being partway through its cell cycle when the simulation begins, so we choose the initial number of cytoplasm nodes M_i to be uniformly random between 15 (recently divided daughter cell) and 29 (pre-mitotic, fully grown mother cell). 2.2 Table provides values for the initial conditions used in simulations along with a description of how each variable was calibrated.

Table 2.2: **Initial conditions for simulations.** Variables that control the initial configuration of the system.

Variable	**Value or Pattern**	**Calibration**
Number of (Non-boundary) L1 cells	8 Cells	Experimentally quantified in (6)
Initial Tissue Shape	"Wedge", Experimentally quantified in (6)	
Tiling of L2-L7 cells	Staggered/Hexagonal grid	Minimizing 4-way junctions
Initial signaling distribution	Spatial distribution as in Methods	Calibrated from experiments
Cell Growth Direction	Stochastically chosen as in Methods	Calibrated from experiments
Parameters controlling boundary cell behavior		
$k^{\text{lin}}_{\text{Boundary}}$	$560.3272 \frac{nN}{\mu m}$	Local SA, see section 2.2.4
η_{Stem}	10	Local SA, see section 2.2.4
Centroid Noise Amplitude A	0	Local SA, see section 2.2.4

All simulations consist of two stages. The first stage starts with circular cells arranged in the experimentally observed "wedge" shape representing the central region of the SAM (see Figure 2.3, panel A). Then the simulation is run without cell growth and division to achieve an equilibrium of the system resulting in specific cell shapes based on experiments as well as a distribution of stresses for each cell (see Figure 2.3, panel B). The second stage makes up the main simulation and starts with the equilibrium state achieved in stage one. In this way, the distribution of cell shapes used as

initial conditions for the main simulation are representative of experimentally observed cell shape distributions. During the second stage, cells are allowed to grow, divide, and dynamically change their cell growth direction polarization in time as described in the Model Description section.

2.2.3 Metrics

Simulation outputs consist of collections of nodes' locations, WUS and CK signal concentration, cell identity within the tissue (i.e. layer), and information tracking the plane of divisions. What follows are the metrics applied to these data for comparison of the model to experimental data. Where applicable, experimental data were manually annotated to have directly analogous metadata (e.g. manual identification of the layers of each cell) in order to calculate these metrics using experimental images as well.

Anticlinal and Periclinal Division Metrics. Division data was recorded for all cells during simulations, including both the orientation of the chosen division plane and the layer the division occurred in. We report only on the layer 3 and below divisions, since L1 and L2 orient divisions via a local rule that always yields anticlinal divisions.

For each cell division j in layers 3 and below in a simulated meristem, consider $\{\Theta_j\}$ to be the set of acute angles the division planes made relative to the horizontal, so each $\Theta_j \in [0, 90°]$. We subdivide this interval to categorize our divisions as we would in experimentation:

$$\underbrace{[0°, 30°]}_{\substack{\text{Periclinal}\\ \text{Division}\\ \text{Range}}}; \quad \underbrace{(30°, 60°)}_{\substack{\text{Diagonal}\\ \text{Division}\\ \text{Range}}}; \quad \underbrace{[60°, 90°]}_{\substack{\text{Anticlinal}\\ \text{Division}\\ \text{Range}}}.$$

Letting A be the number of divisions whose Θ_j fall within the anticlinal division range and P be the number of divisions whose Θ_j that fall into the periclinal division range, the proportion of periclinal divisions for each cell layer was calculated as $P/(A + P)$. The partition of $[0, 90°]$ was chosen to match those used for experimental observations.

Aspect ratio and orientation of Cells. The aspect ratio and orientation of cells in all modeling results were computed directly from simulation data in the following manner. To determine the aspect ratio of a cell, we find the pair of cell wall nodes $W_i^{s^1}, W_i^{s^2}$ that define the short axis, i.e. the line segment with minimal segment distance that evenly divides the cell. The perpendicular bisector of the short axis is drawn to find the direction of the long axis of the cell (see Figure 2.4). The wall nodes closest to the long axis on either side of the cell are taken to be the endpoints of the longest axis itself $W_i^{l^1}, W_i^{l^2}$. The aspect ratio is then determined as the ratio $\frac{\left\|W_i^{l^1} - W_i^{l^2}\right\|}{\left\|W_i^{s^1} - W_i^{s^2}\right\|}$. Cell orientation is measured using the long axis in the same way as experiments described above. Cells with aspect ratios smaller than 1.3 are considered isotropic in shape, otherwise cells are considered as anisotropically expanded along the long axis. The growth direction angle is defined as the acute angle between the x-axis and the long axis direction.

Layered organization of the epidermal L1 and L2 cell layers. To quantify the amount of deviation from the layered organization as shown in Fig 7 H in [1], we separately calculated the root mean squared error (RMSE) of the regression lines fit to the sets of cell centers from both the L1 and L2 cell layers. The values reported in Fig 7 H in [1] are an average of the RMSE for the L1 and L2 layers across all 20 simulations for each distinct mechanism.

Dome height, width, and width-height ratios for simulations. To capture the exaggeration of the dome structure in a given meristem, we measure the *dome height* as follows. If $\{(x_j, y_j)\}$ are the centroids of all layer 1 cells, then

$$\text{dome height} := \max_j y_j - \min_j y_j.$$

To measure the SAM *width*, we measured the maximum distance between layer 1 centroids, given by the expression

$$\text{width} := \max_j x_j - \min_j x_j.$$

The width-height ratio was determined for a given SAM by calculating $\frac{\text{width}}{\text{dome height}}$.

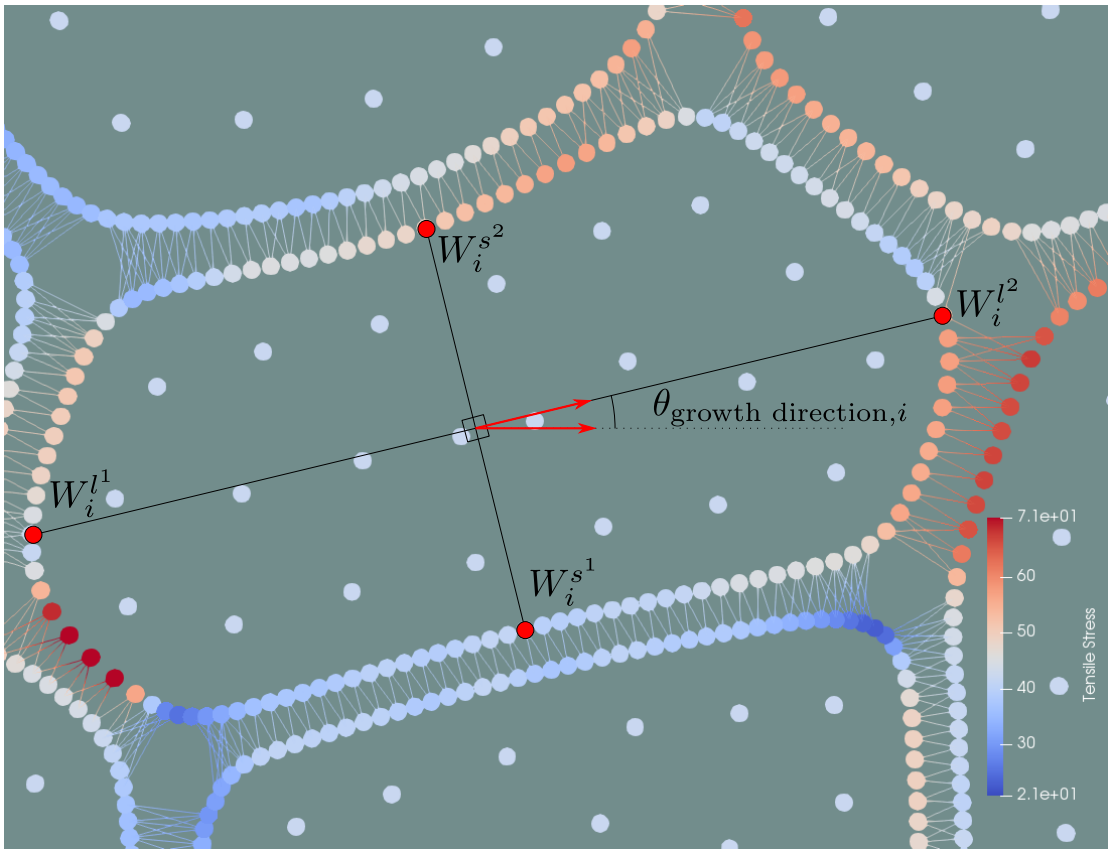

Figure 2.4: **Aspect ratio and orientation of cells.** Nodes $W_i^{s^1}$ and $W_i^{s^2}$ (highlighted nodes) are chosen to evenly divide the cell area with minimal segment length. The perpendicular bisector is formed and nodes nearest are taken to be the long axis $W_i^{l^1}$ and $W_i^{l^2}$ (highlighted nodes). The growth direction angle θ of cell i is the positive acute angle between the horizontal and the long axis. Aspect ratio is also calculated from the lengths of the long and short axes. Orientation is measured in the same way as for experimental images described above. Image was rendered via simulation output, and the heat map shows tensile stress calculated by node as in equation (2.6).

Global curvature of the surface of the SAM. Global curvature of the surface of the SAM was used to compare the shape of the SAM after 40 hours of growth between experiments and simulations. For both experimental and simulation images, the x and y coordinates of each cell center in the L1 layer were recorded. Then a circle was fit to the resulting set of data points using the Circle Fit (Pratt method) in MATLAB. Finally, *global curvature* was calculated by taking the inverse of radius of the best fit circle for each meristem.

Spatial Distribution of WUS in the SAM. To quantify the spatial distribution of WUS in the SAM, we measured both the *radial distance* of WUS in the tissue and analyzed the number of *high WUS containing cells* in the epidermal L1 cell layer. In order to visualize the number of high WUS containing cells in the L1 layer of experimental images, we first quantified the average nuclear WUS fluorescence intensity within each cell in the L1. We then divided the average fluorescence intensity of each cell by the value of the brightest cell in its respective SAM to determine each cell's relative WUS concentration. Next, we binned the relative WUS concentration of all L1 cells by their distance (in average cell diameter) from the brightest cell (i.e. highest WUS containing cell) using a fixed bin size of the average cell diameter for the given meristem and going out to 6 average cell diameters on either side of the brightest cell. In addition, 95% confidence intervals are shown for each bin. The same process was used for simulations as demonstrated in Fig 7 L in [1].

Similar analysis of the WUS concentration across the L2 and corpus of experimental images was used to determine the maximum diameter of the set of high WUS containing cells along the radial axis of the meristem across all layers, denoted D_{CZ}. In addition, we manually measured the diameter of the PZ, denoted D_{PZ}, for each image. We define the radial distance of WUS in the tissue as the ratio $\coloneqq D_{CZ}/D_{PZ}$ as can be seen in Fig 7 K in [1] and Fig A in S1 appendix of [1]. In simulations, we measured the radial distance of WUS in the following way. Let $\{c_j\}$ be the set of all cell centroids for cells with WUS concentration greater than the experimentally calibrated threshold WUS_{min}. We define $D_{CZ} \coloneqq \max_{i,j}\{|c_j - c_i|\}$ and D_{PZ} is equal to SAM width, as described above.

As suggested by previous studies [98], the 8 brightest cells expressing the *CLV3* reporter across the L1 encompass the stem cell population in this layer. Thus, we determined the threshold WUS_{min} for each simulation by calculating the minimum WUS value of all L1 cells within 8 average cell diameters of the highest WUS containing cell in the L1 layer.

2.2.4 Sensitivity and Perturbation Analyses on the Equilibrium State of the SAM

The equilibrium state of the model SAM, as described in section 2.2.2 above, is the result of stage one of the simulation rather than being controlled by any model inputs. Since the equilibrium state serves as the initial condition of the main simulation, we investigated the impact of perturbations on the initial positioning of cells as well as variations in parameters controlling the cell-wall extensibility and stiffness of boundary cells during the establishment of the equilibrium state. In these analyses, we fixed an initial selection of a growth polarization direction and number of cytoplasm nodes for each cell to remove the stochastic confounding of the analyses. We expect that for a fixed distribution of cytoplasm nodes and growth directions for each cell, any impacts clearly attributable to those fixed distributions may be averaged out since they are the only non-deterministic features of the stage one of the simulation.

We perturbed the initial positioning of each cells' center from c_i to $c_i + A \cdot \hat{v}(\Theta)$, where $\hat{v}$ is a unit vector oriented towards the uniformly randomly chosen direction Θ. We perturbed the *centroid noise amplitude* A from 0 to $0.2\mu m$, where 0 returns the unperturbed system and 0.2 is chosen to prevent cell-cell overlapping. Separately, we performed sensitivity analyses on the impacts of two mechanical parameters, $k^{\mathrm{lin}}_{\mathrm{Boundary}}$ and η_{Stem} controlling boundary behavior to assess the impact of boundary dynamics on the equilibrium structure. We examined 100 values of $k^{\mathrm{lin}}_{\mathrm{Boundary}}$ logarithmically sampled between one half and twice its default value, and sampled 100 values of η_{Stem} logarithmically around one tenth and ten times its default value. Parameter values for sensitivity

and perturbation analyses were varied independently; when one was being varied, the others were fixed at their default values.

Figure 2.5 shows the results of the perturbation analysis on A for two tissue-scale and three cell-scale metrics. Though there was an increase of variance of curvature and apical surface length, the proportional increase of the curvature circle's fitness RMSE and the small absolute differences of the metric values suggest that the overall impact of the perturbation is negligible, and can be attributed to slight disruptions to the nearly-colinear centroids of the layer 1 cell layer. The cell-scale metrics show no clear impact of A on cell orientation, aspect ratio, or area distributions. Thus, we conclude that there are no critical singular perturbations of our equilibrium distribution of cells in the tissue arising from any symmetry inherent in the placement of the initial cells within the range of perturbation explored.

Figure 2.6 shows the results of the sensitivity analyses on boundary parameters $k^{\text{lin}}_{\text{Boundary}}$ and η_{Stem}. Within the range of perturbation we explored, the impact of η_{Stem} on all tissue-scale and cell-scale measurements were negligible, except for a slight increase in stem-layer cell area when damping values were dropped substantially. Lastly, $k^{\text{lin}}_{\text{Boundary}}$ was demonstrated to slightly decrease the apical surface length of the SAM by $0.3\mu m$. However, this is consistent with the observations that high-$k^{\text{lin}}_{\text{Boundary}}$ simulations have boundary cells shrink due to tightened walls, which forces the adhered, neighboring cells into alignment. This is further supported by the impact of $k^{\text{lin}}_{\text{Boundary}}$ cell area, wherein the equilibrium area of a boundary is smaller with a higher value of $k^{\text{lin}}_{\text{Boundary}}$. For all non-boundary cells, the impact of $k^{\text{lin}}_{\text{Boundary}}$ is negligible.

2.2.5 CAE-M Division Plane Mechanism in 3D

This subsection is a reproduction of the extended model description presented in the S3 appendix of [10]. This subsection was drafted and revised in equal collaboration between Mikahl Banwarth-Kuhn and myself.

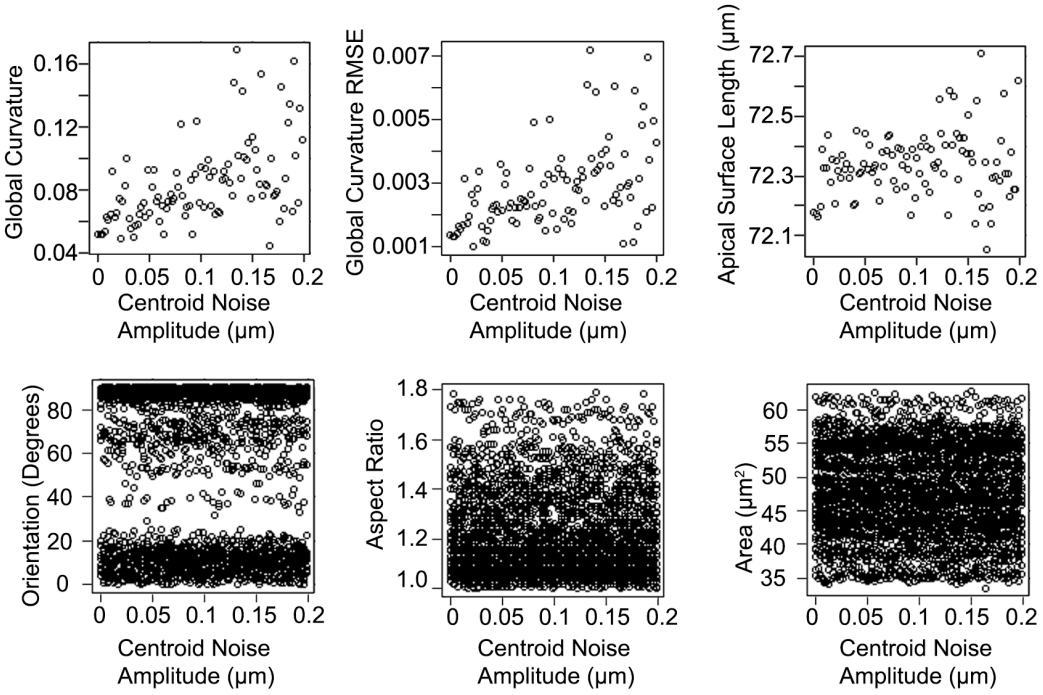

Figure 2.5: **Perturbation Analysis of Equilibrium State.** Perturbation analysis results of adding small, random displacements to initial cell locations on the mechanical equilibrium state of the tissue - i.e. after representing t =15 minutes of growth, as discussed in section 2.2.4. The top left and top center panels demonstrate both the impact of cell center displacement on global curvature and how that impact may be attributed to the fitness of a circle to the surface. The top right panel shows that the apical surface length of the equilibrium SAM is only impacted via a negligible increase in variation of the total apical surface length. The bottom panels show all cell-level measurements of non-boundary cell orientation, aspect ratio, and areas from 100 simulations of increasing centroid noise amplitude. These panels exhibit independence of cell geometry and orientation from random cell displacement - suggesting that the initial tiling's precise spatial arrangement does not play a role in the equilibrium distribution of cells.

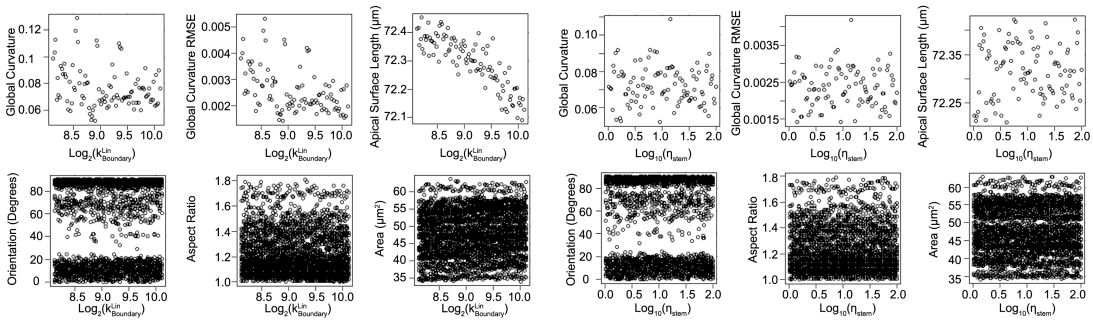

Figure 2.6: **Sensitivity Analysis of Equilibrium State.** Tissue scale (top) and cell-scale (bottom) measurements taken from simulated SAMs after 15 minutes of simulated growth were represented as in section 2.2.4. Values of k^{lin} (left 6 panels) and η_{Boundary} (right 6 panels) were independently varied to 100 values around their default. (Top) all tissue-scale impacts on boundary dynamics were negligible, with the exception of the reduction of apical surface length with a fourfold increase of $k^{\text{lin}}_{\text{Boundary}}$. However, this is attributable to the shrinkage of the boundary cells with high k^{lin} on the boundary which, upon observation, appear to pull the SAM surface flatter. This difference is less than half of a micron, and so we conclude that the overall impact of boundary cell properties on tissue-scale measurements is negligible. (Bottom) Local sensitivity analysis shows no impact of passive boundary mechanical properties on equilibrium cell shape.

In what follows, we describe how the CAE-M division plane mechanism would be implemented in a 3D, subcellular element (SCE) model of cells of the SAM (see Figure 2.7). In our 3D model of cells of the SAM, plant cell walls are discretized using a triangular mesh consisting of a set of edges and nodes in three dimensions. The 3D version of the CAE-M mechanism of positioning the division plane consists of first calculating the local stresses at each cell wall node in the plane tangent to the cell wall surface at each node. We denote the tangent plane at node N to be T_N. The cell wall node with the maximal net stress (i.e. the node with the largest sum-square of stresses projected onto T_N) is chosen as the "base-point" or node with maximal stress denoted N_{Max}. Next, we compute the local stress vectors between cell wall nodes in a small neighborhood around N_{Max} and then project these stresses onto $T_{\text{N}_{\text{Max}}}$. The vector v_{max} is chosen as the average of these projected stresses that represents the maximal stress direction on the cell surface at N_{Max}, then we find a vector v_1, which is orthogonal to v_{max} and in the plane $T_{\text{N}_{\text{Max}}}$. At this point, candidate division planes are any planes which include both the vector v_1 and the point N_{Max}, and so we choose the

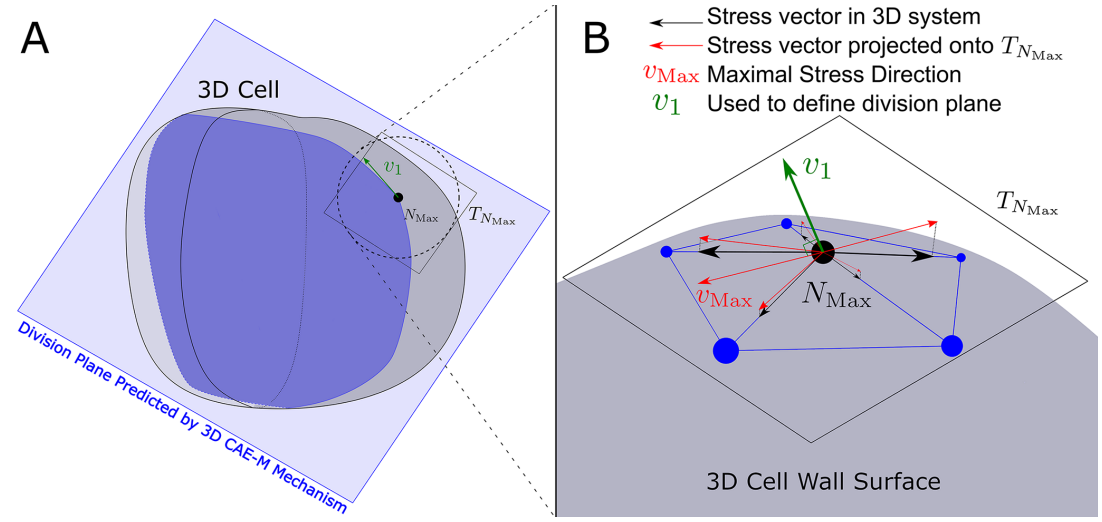

Figure 2.7: **CAE-M division plane mechanism in 3D model.** (A) Diagram of a 3D model cell is shown in gray and depicts the cross-section of the division plane predicted by the CAE-M mechanism in blue. The vector v_1 (green) is used to determine the cell division plane by finding the plane that includes both v_1 and N_{Max}, and that divides the cell volume approximately in half. (B) Diagram of the calculation of v_{Max}, the maximal stress direction in $T_{N_{\mathrm{Max}}}$ within a neighborhood of N_{Max}, and the resulting vector v_1 in $T_{N_{\mathrm{Max}}}$ orthogonal to v_{Max}. Vectors indicating stresses acting on N_{Max} as a result of nearby cell wall nodes are indicated in black, and their projection onto the tangent plane $T_{N_{\mathrm{Max}}}$ is shown in red.

3D CAE-M division plane to be the one that also divides the cell volume approximately in half. Note that if our calculation results in $v_1 = 0$, this represents isotropic local stress and in this case v_1 is selected as a random direction in $T_{\mathrm{N_{Max}}}$. We included Figure 2.8 below to demonstrate that, in at least a simplified case, the division plane line segment in 2D lies at the intersection of the 3D division plane and the longitudinal SAM section we are modeling in simulations.

2.3 Selected results and analysis of the 2D model

This section is a partial reproduction of the results presented in [1]. Though the first authors were Mikahl Banwarth-Kuhn and Kevin Rodriguez, I contributed substantially to the image analysis, writing, figure generation, and revision of this work in each section. All experimental

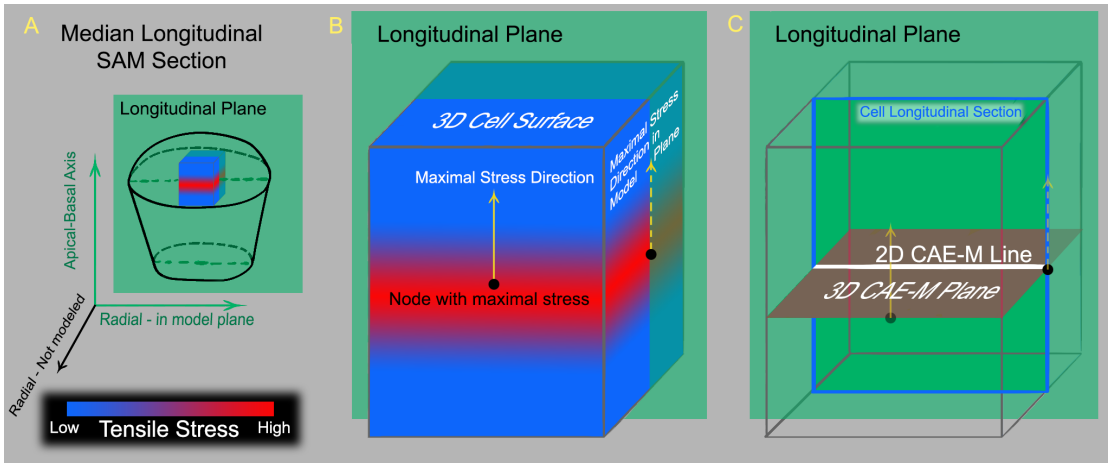

Figure 2.8: **CAE-M division plane in 3D cell and corresponding 2D model plane.** (A) 3D SAM (black lines) with cell (blue) intersected by the 2D longitudinal plane (green) our model simulates. (B) 3D cell (blue) intersected by the 2D model plane (green). The front face of the cell shows the out-of-plane node with maximal stress and maximal stress direction (solid yellow arrow) found using the 3D version of our CAE-M mechanism. The right face of the cell shows the in-plane node with maximal stress and maximal stress direction (dashed yellow arrow) found using the 2D version of our CAE-M mechanism based on in-plane tensile stresses. (C) 3D cell intersected by 2D model plane (green) and the division plane predicted by the 3D CAE-M mechanism (brown). The line segment predicted by the 2D CAE-M mechanism lies at the intersection of the 3D division plane and the 2D model plane (solid white line).

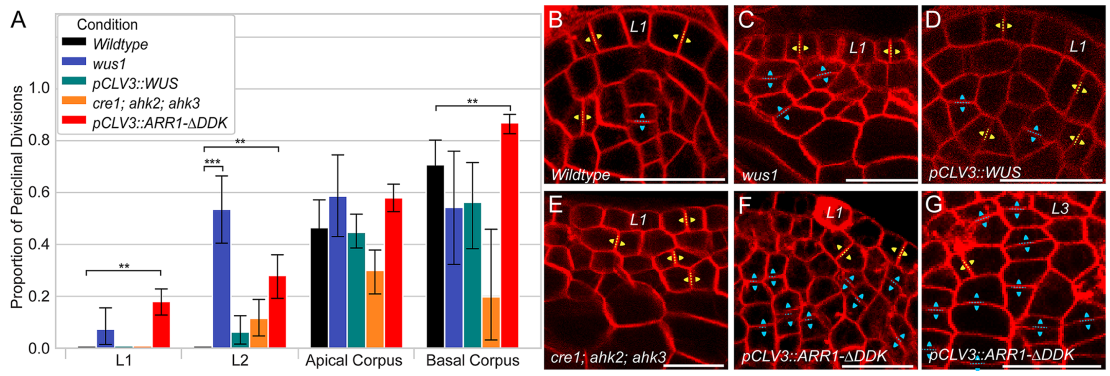

Figure 2.9: **Layer-specific organization of cell division plane orientation**. (A) Periclinal and anticlinal divisions were quantified by cell layer on a minimum of 10 SAMs (see S1 Appendix of [1] for details). Significance tests were performed using independent t-tests. Asterisks indicate significance at the following levels: ** ($p \leq 0.01$), *** ($p \leq 0.0001$). Higher magnification median longitudinal section from Chapter 1 Figure 1.2 showing (B) wildtype [l*er*], (C) *wus1-1*, and (E) *cre1-12;ahk2-2;ahk3-3* vegetative meristems. 48 hour Dex induction of (D) ectopic misexpression of WUS *[pCLV3::LhG4; 6xOP::eGFP-WUS-GR]* and (F) ectopic misexpression of CK signaling *[pCLV3::LhG4; 6xOP::ARR1-ΔDDK-GR]*. (G) Characteristic "strips" of cells formed by repeated periclinal divisions in the Basal corpus of ectopic misexpression of CK experiments. (B-G) Positioning of new cell walls between speculated daughter cells after recent divisions are annotated in yellow arrowheads for anticlinal cell division and cyan arrowheads for periclinal cell division. Scale bar = 20 μm.

methods were designed and performed by G.V. Reddy, Kevin Rodriguez, and Alexander Plong at the Reddy lab at U.C. Riverside. Image analysis techniques were selected and configured by Amit K. Roy-Chowdhury his graduate student Calvin-Khang Ta. Output of image segmentation methods were analyzed by Christian Michael and Mikahl Banwarth-Kuhn. I also substantially contributed to the design and creation of figures and captions in this chapter.

2.3.1 Testing hypothesized mechanisms of the regulation of SAM growth using a computational model

It is experimentally difficult if not impossible to uncouple the effects of WUSCHEL and cytokinin in controlling cell division plane orientation and the direction of anisotropic expansion of cells. To address this, we developed a detailed, biologically calibrated, multiscale, computational

model and used it to test three separate hypothesized mechanisms for how WUS, CK, and mechanical stresses can regulate cell division plane orientation in the corpus (for details see the Section 2.1.1 and Section 2.2). The first two mechanisms we tested assume that the sole functions of WUS and CK are in regulating the direction of anisotropic expansion of cells. In the model, the direction of anisotropic expansion of cells is determined by an experimentally-calibrated probability distribution where cells with relatively high levels of WUS are more likely to preferentially expand in the radial direction and cells with relatively high levels of CK are more likely to preferentially expand in the apical-basal direction (see Section 2.1.1 for details). We refer to this mechanism of regulation as "the control of anisotropic expansion" (CAE). In simulations assuming the CAE mechanism, we compared simulation output where division plane orientation was determined using either Errera's rule (CAE-E mechanism), which assumes that cells divide by following the shortest path, or "the mechanical division rule," (CAE-M mechanism), which assumes that cells divide according to maximum in-plane tensile stress on their cell wall (see Figure 2.10A and Section 2.1.1 for details).

The third mechanism we tested assumes dual roles for WUS and CK in both regulating anisotropic cell expansion and cell division plane orientation. We refer to this mechanism of regulation as "the control of expansion and division" (CED). In simulations assuming the CED mechanism, the direction of anisotropic cell expansion is determined by relative concentrations of WUS and CK as above, and cell division plane orientation is determined by a second experimentally-calibrated probability distribution where cells with relatively high levels of CK are more likely to divide periclinally (perpendicular to the root-to-shoot axis) and cells with relatively high levels of WUS are more likely to divide anticlinally (perpendicular to the SAM surface) (see Figure 2.10A and Section 2.1.1 for details).

To test the CAE-E, CAE-M and CED mechanisms described above, we simulated growing SAMs under three different experimental conditions where the levels and spatial patterns of WUS and CK were calibrated to be analogous with either wildtype, ectopic misexpression of WUS or ectopic misexpression of CK experiments (see the Section 2.1.1 and Section 2.2 for details). We then

compared model simulations directly with experiments using both cell (aspect ratios and orientations) and tissue level metrics (proportion of periclinal divisions, ratio of SAM width to SAM dome height, global curvature of the SAM surface, spatial distribution of WUS in the tissue and layered structure of the L1 and L2 cell layers) to determine the mechanism of WUS and CK-mediated regulation of cell division plane orientation in the corpus (see Section 2.2.3 for biological relevance of the metrics we used and further details). Results below are based on 20 simulations for each of the nine conditions tested. Each simulation begins with an organized array of 50 cells in seven cell layers as shown in Figure 2.10B, and we allow each simulated meristem to grow for approximately 40 hours. Typical output from simulations involving each of the three mechanisms under wildtype conditions is shown in Figure 2.10B, 2.10C, 2.10D, 2.10E, and S1 Video of [1]. In what follows, we first demonstrate that a 2D model provides an appropriate approximation for studying cell behaviors in the central region of the corpus, and then we provide a detailed description of the model simulation results used to test the specific hypothesized mechanisms above.

CAE-M and CED mechanisms regulate cell division plane orientation in a layer-specific fashion. Next we tested whether the CAE-E, CAE-M, and CED mechanisms could produce experimentally observed proportions of periclinal divisions in the corpus. We found that in the Apical corpus, the CAE-M and CED mechanisms resulted in a proportion of periclinal divisions that was not significantly different from experiments, while the CAE-E mechanism was significantly higher (p-value = 2.93e-4) (Figure 2.10H). In contrast, in the Basal corpus, we found that only the CED mechanism resulted in a proportion of periclinal divisions that was not significantly different from experiments, while the CAE-E and CAE-M mechanisms were significantly lower (p-value = 5.5e-3 and 3.86e-2 respectively) (Figure 2.10H). Since both the CAE-M and CED mechanisms matched experimental cell shapes and the proportion of periclinal divisions in the Apical corpus, it is unclear which of these two mechanisms is likely to control cell division plane orientation there. However, since only the CED mechanism matched the proportion of periclinal divisions in the Basal corpus,

this suggests that chemical and mechanical signals could regulate cell division plane orientation in a layer specific fashion. Thus, in order to uncouple the role of the CAE-M and CED mechanisms in directing cell division plane orientation in individual cell layers, we studied the effect of each mechanism in simulations where we independently perturbed the levels and spatial patterns of WUS and CK.

Layer-specific, combined chemical and mechanical regulation of cell division plane orientation can maintain SAM structure and shape. Based on our simulation results above (Figs 5-7 of [1]), we next tested whether a layer-specific, combined chemical and mechanical mechanism regulating cell division plane orientation would maintain SAM structure and shape. To do this, we ran wildtype simulations where cells in the Apical corpus follow the CAE-M mechanism and cells in the Basal corpus follow the CED mechanism for division plane placement (Figure 2.11D). We refer to this model of regulation as "the combined CAE-M and CED" mechanism. First, we found that the combined CAE-M and CED mechanism resulted in a distribution of mother cell orientations that was not significantly different from experiments in the Apical corpus, and maintained a bimodal distribution in the Basal corpus (Figure 2.11E). Second, we found that the combined CAE-M and CED mechanism produced experimentally observed distribution of cell aspect ratios in both the Apical corpus and Basal corpus (Figure 2.11F). We also found that the proportion of periclinal divisions matched experiments in both the Apical corpus and Basal corpus (Figure 2.11G). Since we observed slightly more periclinal divisions in the Basal corpus of combined CAE-M and CED simulations compared to wildtype SAMs, we believe this could explain why the distribution of mother cell orientations in this region did not result in a direct match with the experimental distribution. Finally, we found that the combined CAE-M and CED mechanism resulted in the smallest amount of deviation from the layered organization of the epidermal L1 and L2 cell layers compared to the CAE-E, CAE-M, and CED mechanisms (Figure 2.11H). This suggests that a layer-specific,

combined chemical and mechanical mechanism regulating cell division plane orientation is necessary to maintain the multi-layered structure of the SAM.

Next, we investigated whether the combined CAE-M and CED mechanism would result in the correct shape and size of the SAM. While all four mechanisms resulted in experimentally observed SAM size (i.e. average ratio of SAM width to dome height) (Figure 2.11I), our analysis revealed that the combined CAE-M and CED mechanism most closely matched experimentally observed SAM shape (i.e. global curvature) (Figure 2.11J). Notably, while both the CED and combined CAE-M and CED mechanisms most closely matched the experimentally observed distribution of WUS in the radial direction (Figure 2.11K), only the combined CAE-M and CED mechanism resulted in the correct number of high WUS containing cells in the epidermal L1 cell layer (Figure 2.11A-2.11D, and 2.11L). S5 Fig of [1] provides additional analysis of the time evolution of simulated cell orientations and aspect ratios by condition and division plane mechanism.

2.4 Partial discussion of 2D model results

The work of [1] aims to further elucidate the structure-function relationship between the mechanisms driving SAM growth and proper stem cell regulation in plants. Through comparing experimental and model simulation results obtained under multiple perturbation conditions, we confirmed that 1) in the Apical corpus, WUS and CK only regulate anisotropic expansion of cells and cell division plane orientation is determined based on tensile stress on the cell wall and 2) in the Basal corpus, WUS and CK regulate both cell division plane orientation and anisotropic expansion. Moreover, experimental results confirm our model prediction that this layer-specific, combined chemical and mechanical mechanism can maintain proper SAM shape, layered structure, and the correct distribution of WUS within the tissue. Hence, the results of the work of [1] provide an additional link between the roles of WUS, CK, and mechanical stress in regulating pattern and shape during SAM morphogenesis. Cell and tissue level outcomes resulting from the testing of four

hypothesized mechanisms of regulation compared to experiments are summarized in Tables 1 and 2 of [1]. Since some results were not presented in this dissertation, we refer the reader to [1] for full details.

Obtained results also complement several recent studies linking mechanical stress on the cell wall to macroscopic behavior of plant tissues [12, 100, 101, 102]. Our work provides further mechanistic insight into how stress on individual cell walls could regulate cell division plane orientation in the corpus. Namely, we found that model simulations assuming cell division plane orientation based on local patterns of tensile stress on the cell wall closely matched experimental data, while simulations assuming cell division plane orientation based on cell shape (i.e. Errera's rule) did not. This is profound because it suggests that tensile stress caused by growth heterogeneity and other local interactions supersedes cell shape in controlling cortical microtubule orientation which plays a crucial role in cell wall deposition [100, 99, 103, 12].

While our knowledge of exactly how cells sense and interpret mechanical forces prior to cell division remains unclear, it has been demonstrated that microtubules directing microfibrils impact placement of the preprophase band (PPB) (a microtubule and microfilament structure that marks the cell division plane before mitosis) [99, 103, 104]. In addition, coordination of cell division among neighboring cells both within and across clonally distinct layers could be mediated by mechanical cues [59]. Although directly measuring mechanical stress in the internal cell layers of the SAM remains experimentally difficult, the quantitative image analysis of microtubule dynamics has been used to indirectly infer stress patterns in the distal portion of the SAM [12, 105]. Thus, similar quantitative approaches could provide a way to verify stress distributions from our computational model predictions to better understand how cells communicate via mechanical cues to regulate cell division plane orientation.

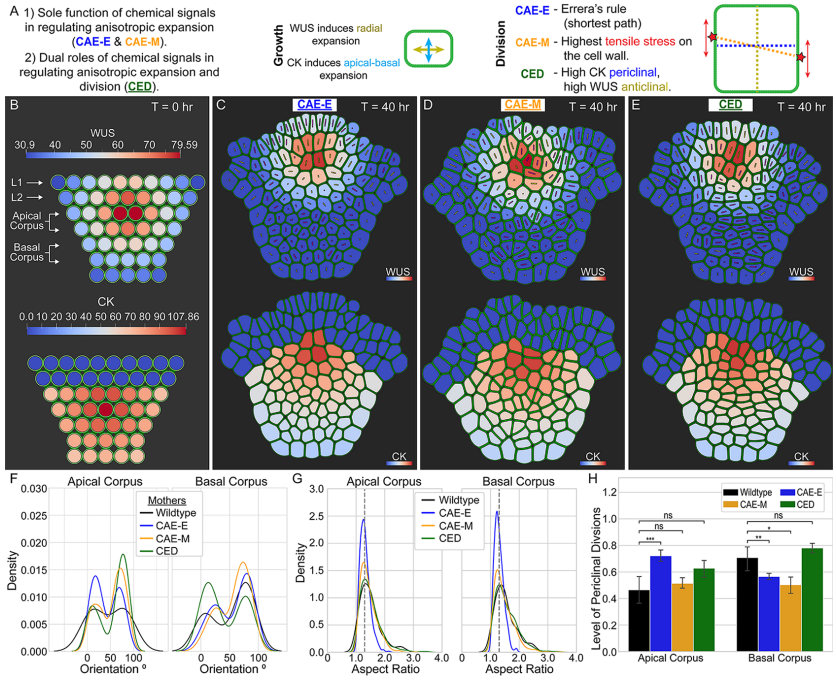

Figure 2.10: **Results of computationally testing three hypothesized mechanisms of cell division plane orientation in the corpus**. (A) Three hypothesized mechanisms for WUS and CK-mediated regulation of cell division plane orientation and the direction of anisotropic expansion of cells. (B) Cells are initialized as circles and allowed to "relax" into more biological cell shapes before growth and division begin (see Section 2.2 for details on model initial and boundary conditions). The internal colors of cells represent their levels of WUS (top row) and CK (bottom row). (C-E) Final simulation time point after 40 hours of growth reveals differences in cell shapes and orientations between each of the three mechanisms. The internal color shows the final levels and spatial patterns of WUS (top row) and CK (bottom row). Line segments inside cells are provided to help visualize cell aspect ratios and orientations. The length of each line segment is proportional to the encompassing cell's aspect ratio, where cell's with aspect ratio = 1 have line segments with length 0. The directional vector of each line segment represents the orientation of the longest axis of the encompassing cell. Purple lines denote daughter cells while yellow lines denote mother cells (see S1 Appendix of [1] for details on mother/daughter cell classification). (F) The distributions of mother cell orientations for the CAE-E (blue), CAE-M (gold), and CED (green) mechanisms were not statistically different from wildtype experiments (black) in both the Apical corpus (p-value = .5520, .6841, and .8330 respectively) and Basal corpus (p-value = .7567, .3103, and .2173 respectively). (G) The distributions of cell aspect ratios for the CAE-M (gold) and CED (green) mechanisms were not statistically different from wildtype experiments (black) in both the Apical corpus (p-value = .4879 and .9521 respectively) and Basal corpus (p-value = .1724 and .5781 respectively) while the CAE-E mechanism was significantly different (p-values < 1.0e-32 in both cell layers). (H) Proportion of periclinal cell divisions in the Apical and Basal corpus for all three mechanisms. In the Apical corpus, the CAE-M and CED mechanisms matched experiments, while the CAE-E mechanism did not (p-value = 2.93e-4). In the Basal corpus, only the CED mechanism matched experiments (p-value = 5.5e-3 and 3.86e-2 for the CAE-E and CAE-M mechanisms respectively). S2 Fig of [1] provides extended analysis between experimental wildtype SAMs and wildtype simulations for all four hypothesized mechanisms presented in this paper ([1]).

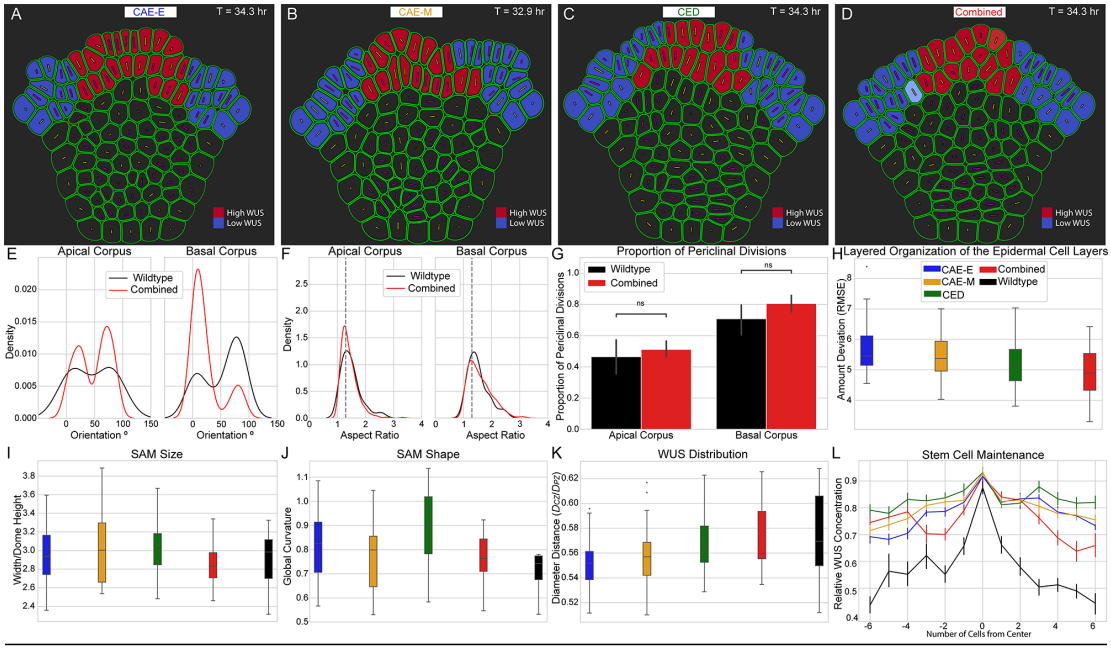

Figure 2.11: **Layer-specific combined chemical and mechanical regulation of cell division plane orientation maintains proper shape, multi-layered structure and spatial distribution of WUS in the SAM.** (A-D) Typical simulation output after 40 hours of growth for all four mechanisms (CAE-E, CAE-M, CED, and combined CAE-M and CED) in wildtype signaling conditions. Cell color highlights distinct patterns of WUS accumulation in the epidermal L1 and L2 cell layers for each mechanism (red = high WUS and blue = low WUS). (E-F) The combined CAE-M and CED mechanism resulted in distributions of (E) mother cell orientations that were similar to experiments and (F) cell aspect ratios that matched experiments. (G) The proportion of periclinal cell divisions in combined CAE-M and CED simulations were found to match experiments. (H) The combined CAE-M and CED mechanism resulted in the smallest amount of deviation from a single-cell layer in the epidermal L1 and L2 cell layers. The combined CAE-M and CED mechanism most closely matched experimentally observed SAM (I) size- the ratio of SAM width to dome height, (J) shape- global curvature of the SAM surface, and (K) WUS distribution in the SAM after 40 hrs of growth. (L) The combined CAE-M and CED mechanism resulted in the correct number of high WUS containing cells in the epidermal L1 cell layer. (E-L) Experimental wildtype (black), CAE-E (blue), CAE-M (gold), CED (green), and combined (red) in all panels. See Section 2.2.3 for detailed description of all metrics used in this Figure.

Chapter 3

Pseudo-3D Mathematical Model of the SAM with Boundary Conditions

3.1 Model Description

This section describes different submodels and how they are linked to one another to provide novel detailed 2D and Pseudo-3D models of the 2D longitudinal section of the shoot apical meristem with specific boundary conditions (Figure 1.3 C). A diagram of the flow of information between submodels is provided in Figure 3.1 in both the 2D SAM model and the P3D SAM model. The main advantages of these multiscale models are their detailed biologically-calibrated descriptions of cellular growth and division, a detailed implementation of tunica tension boundary conditions and, for the P3D model, the inclusion of cell anisotropic expansion and division both in and out of the model plane. The justification for modeling a specific section of the tissue is given in Section 3.1.1. It should be noted that the models in this chapter and Chapter 2 are based on the same subcellular

element model approach, but are substantially different. The model in Chapter 2 is two-dimensional, and the model in Chapter 3 is pseudo-3D and has a detailed description of boundary forces.

It was found in [1], by using a 2D model, that cells in the apical corpus of the SAM are likely to divide according to mechanical cues with freely expanding SAM boundary. In this chapter, we study, by using a newly developed and calibrated P3D model, the roles of a force distribution applied to the SAM boundary and of out-of-plane growth, on the maintenance of shape and structure of the SAM. Cell growth and division are assumed to be controlled by concentrations of cytokinin and WUSCHEL as observed in experiments [1]. Cells are modeled as a heterogeneous collection of nodes representing the cell wall and cytoplasm which interact with each other through local forces, are discussed in Section 3.1.2.

In the models, cytoplasm nodes are added to each cell at a signal-dependent rate, resulting in turgor pressure increase and leading to addition of new wall nodes to accommodate for the build-up of pressure (Section 3.1.4). Cells are assumed to grow anisotropically entirely within the model domain in the 2D model, or both along the plane or orthogonal to the SAM longitudinal section in P3D model (Figure 3.4 E). Model cells are assigned a concentration of WUS and CK in the chemical signaling submodel (Section 3.1.4) which influences growth direction polarization and growth rate (Section 3.1.5 and 3.1.4). Once cells reach the end of their cell cycle, they divide with a division plane position determined via a mechanism discussed in [1]. Section 3.1.7 details how these models are coupled together. Lastly, Section 3.1.8 describes the representation of out-of-plane cell anisotropic expansion unique to the P3D model.

In these models, cytoplasm nodes are added to each cell at a signal-dependent rate, and this turgor-pressure resultant expansion induces deposition of new wall nodes (Section 3.1.4). The models assume that cells grow anisotropically with stochastic behavior determined by signals 3.1.6, and this may happen either entirely within the model domain (2D), or both along the plane or orthogonal to the SAM longitudinal section (P3D, Figure 3.4 E). Cell growth direction polarization is detailed

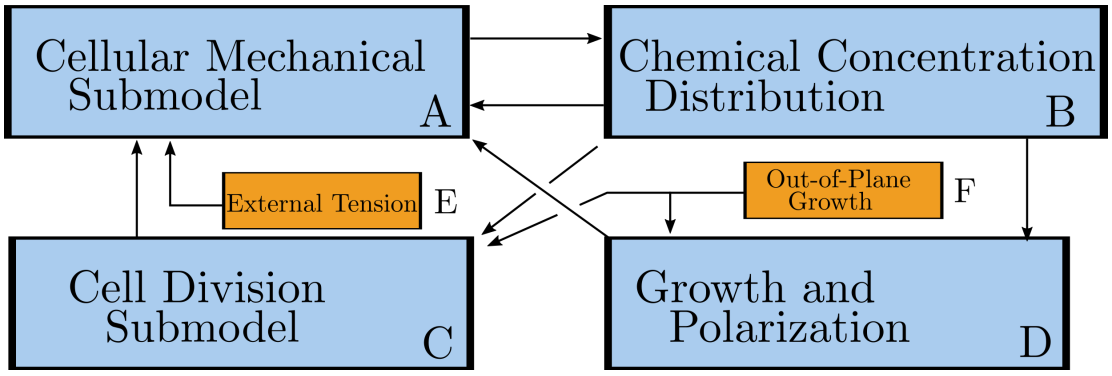

Figure 3.1: **Information flow between the coupled submodels and novel extensions.** (A-D) Boxes show the interdependencies between the major submodel components. (A) The cellular mechanical submodel determines the domain and signal center for the chemical distribution submodel. (B) The impact of WUS and CK are represented by a calibrated spatially-dependent approximation of their concentration in cells. Cells' CK and WUS values parameterize the probabilities of anticlinal vs. periclinal expansion as well as growth rate; and the orientation of cell division in the basal corpus. (C) The cell division submodel changes the number and position of nodes by adding new cell walls and allowing multiple cell cycles to be represented. (D) The growth direction polarization submodel stochastically chooses a preferred anisotropic expansion direction for cells based on their signal concentrations, and cell growth changes the mechanical equilibrium of the mechanical submodel by continually adding new cytoplasm nodes at a WUS-dependent rate. (E) Tension applied to the meristem is given by force acting upon the boundary nodes of cells in layers 1 and 2, directed to promote experimentally calibrated curvature. The magnitude of the force is computed in Section 3.1.10. (F) In the P3D model, growth polarization out-of-plane represents the impact of three-dimensional expansion of cells, as well as how their division is represented.

in Section 3.1.5. Once cells reach the end of their cell cycle, they divide with a division plane selected via a mechanism discussed in [1], though the implementation is detailed in Section 3.1.6. Cell growth direction polarization and division in response to signaling concentrations are governed by an implementation of an experimentally-calibrated probability distribution based on the Hill function as in [1] detailed in 3.1.6.

Figure 3.1 provides an overview for information flow between submodels. The cellular mechanical submodel provides geometry for cell division and chemical signaling domains. Distributions of WUSCHEL and cytokinin determine growth and polarization properties of the cell (Sections 3.1.5 and 3.1.6). Division adds new cells, wall nodes, and adhesion connections. Growth and polarization modify subcellular mechanical properties across a cell's wall nodes. Cells in each meristem place their division plane via the layer-specific mechanism described in [1].

3.1.1 Experimentally calibrated model of a longitudinal section of the central zone of the SAM

At this point, the use of a detailed three-dimensional subcellular element model is prohibitively expensive for large portions of three-dimensional tissue [1], so using a 2D model by leveraging symmetry is critical. Our models represent a longitudinal section of the central region of a SAM as it develops in time, and the SAM has been experimentally observed to have radially symmetry in both tissue shape and signaling distributions. Previous work [1] showed that longitudinal sections of the SAM contain information about the shape of the cell the sections were taken from if consideration is restricted to those cells with high aspect-ratios. In order to use this assumption in a P3D mechanical model of the SAM, we checked whether this symmetry holds for the distribution of shape features of longitudinal sections of cells.

The radial symmetry is not strictly maintained due to perturbations by developmental processes (e.g. when primordia are formed during phyllotaxis). However, a majority of SAM central zones' longitudinal sections look similar regardless of the plane chosen. To support this, we imaged 14

wildtype SAM central zones in three dimensions and, after segmentation and analysis (see Section 5.4 for details), we found that when varying the choice of an axial-basal plane, 8 SAMs did not show a significant difference in cell section area distribution, and 13 showed no difference either cell aspect ratio distribution or directions of anisotropic expansion in cells' longitudinal sections. However, even a radially symmetric structure may still be affected by forces or cell behavior directed orthogonally to a longitudinal plane. One such phenomenon, cells' expansion and division orthogonal to the longitudinal plane, is represented in the model in subsection 3.1.8.

Based on the image analysis, we then assume that experimentally calibrated 2D and P3D models of the SAM are sufficient to capture the dynamics and mechanical interactions of the SAM on a cell-scale up to matching distributions. Some of the cell-scale mechanical components of the models were calibrated and validated in our previous work [1] by matching simulated and experimental values of cells' aspect ratios, orientations of longest axes, and by matching the distribution of cell centroids in simulations to experimental longitudinal sections.

3.1.2 Subcellular elements (SCE) mechanical submodel

Individual cells are modeled as a heterogeneous collection of wall nodes and internal nodes, interacting via potentials representing mechanical forces, moving in two dimensional space as in Banwarth-Kuhn et al.[2]. Each cell i has N_i wall nodes W_i^j $(j = 1, \dots N_i)$ and M_i cytoplasm nodes C_i^j (for $j = 1, \dots, M_i$). We use W_i^j and C_i^j to indicate both spatial coordinates of nodes in $\mathbb{R}^2$ as well as node identity. Moreover, W_i^j is a neighbor of $W_i^{j\pm1}$ where we denote $W_i^{N_i+1} = W_i^1$and $W_i^0 = W_i^{N_i}$, since the wall nodes form a loop and the first and last nodes are neighbors. Nearby

nodes W_k^l from adjacent cells (i.e. $k \neq i$) can adhere to node W_i^j. The Langevin equations of motion of individual nodes are as follows:

$$\begin{aligned}\eta_i \frac{d}{dt} W_i^j = &- \sum_{k=1}^{M_i} \nabla E_{\text{Turg}}(W_i^j, C_i^k) - \sum_{k=j\pm 1} \nabla E_{\text{Ext}}(W_i^k, W_i^j) \\ &- \nabla E_{\text{M.F.B.}}(W_i^j, W_i^{j\pm 1}) - \sum_{\text{Cells } l} \sum_{k=1}^{N_l} \nabla E_{\text{V.E.D.}}(W_i^j, W_l^k) \\ &- \sum_{\substack{\text{Adhesion} \\ \text{partners } \ell}} \nabla E_{\text{Adh}}(W_i^j, W^\ell) + F_{\text{Boundary}}\end{aligned} \tag{3.7}$$

$$\eta_i \frac{d}{dt} C_i^j = - \sum_{k=1}^{M_i} \nabla E_{\text{Pres}}(C_i^k, C_i^j) - \sum_{k=1}^{N_i} \nabla E_{\text{Turg}}(W_i^k, C_i^j), \tag{3.8}$$

where η_i is a cell's damping coefficient, which represents the relative viscosity experienced by the small amount of mass represented by each node as in [2]. The force F_{Boundary} is the force applied to specifically chosen nodes belonging to boundary cells in the tunica. The boundary force F_{Boundary} is described more in Section 3.1.3. Potentials E in the equations 3.7-3.8, yielding forces acting on nodes representing cell wall and cytoplasm, are described in Table 3.1 and illustrated in Figure 3.2. They have a form of a Morse or linear spring type potential:

$$\begin{aligned}E_{\text{Morse}}(\boldsymbol{x}, \boldsymbol{y}) &= U_{\text{Morse}} \exp\left(\frac{-\|\boldsymbol{x}-\boldsymbol{y}\|_2}{\xi_{\text{Morse}}}\right) - V_{\text{Morse}} \exp\left(\frac{-\|\boldsymbol{x}-\boldsymbol{y}\|_2}{\gamma_{\text{Morse}}}\right), \\ E_{\text{Linear Spring}}(\boldsymbol{x}, \boldsymbol{y}) &= \frac{1}{2} k^{\text{lin}}_{\text{Linear Spring}} \left(\|\boldsymbol{x}-\boldsymbol{y}\|_2 - \ell^{\text{eq}}_{\text{Linear Spring}}\right)^2, \\ E_{\text{Bending Spring}}(\boldsymbol{x}, \boldsymbol{y}, \boldsymbol{z}) &= \frac{1}{2} k^{\text{bend}}_{\text{Bending Spring}} \left(\theta_{\angle \boldsymbol{yxz}} - \theta^{\text{eq}}_{\text{Bending Spring}}\right)^2.\end{aligned}$$

These formulae describe soft-core potentials (i.e. the potential has finite value as $\boldsymbol{x} \to \boldsymbol{y}$). Such methods are commonly used in molecular dynamics simulations [106]. With soft-core potentials, the volume exclusion forces never approach infinity. This promotes numerical stability. Even though this means that volume exclusion forces may be exceeded and two cells may be "pushed to overlap", such a phenomenon would require tremendous force which is not observed with the parameter ranges used in our model simulations. These forms of the potentials are also differentiable and have critical

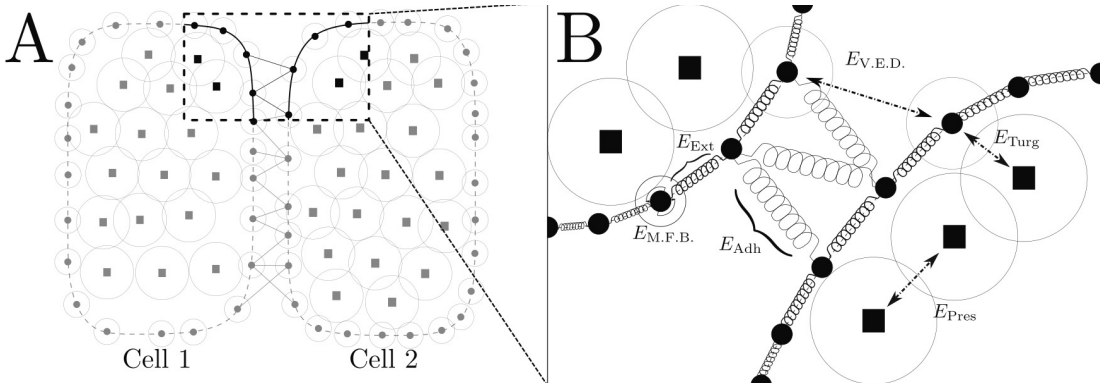

Figure 3.2: **Diagram of the mechanical submodel.** (A) Two interacting cells represented by heterogeneous collections of linked wall nodes (solid circles) and the cytoplasmic nodes (squares) with characteristic Morse potential ranges (rings). (B) Cells' nodes interacting with each other through mechanical forces represented by potentials described in Table 3.1.

Table 3.1: Model potentials and associated physical phenomenon.

Potential	Type	Cellular property
E_{Turg}	Morse Potential	Turgor pressure
E_{Ext}	Linear Spring	Mechanical Stiffness & Extensibility
$E_{\text{M.F.B.}}$	Bending Spring	Bending Stiffness of microfibrils
$E_{\text{V.E.D.}}$	Morse Potential	Volume exclusion between different cells
E_{Adh}	Linear Spring	Cell-cell adhesion (See Figure 5 of [2])
E_{Pres}	Morse Potential	Cytoplasmic pressure

points at $\boldsymbol{x} = \boldsymbol{y}$ for our parameter values, which guarantees that $-\nabla E_{\text{Morse}}(\boldsymbol{x}, \boldsymbol{y})$ is continuous in the variable $\|\boldsymbol{x} - \boldsymbol{y}\|_2$.

3.1.3 Boundary forces provide epidermal tension and impose curvature

The SAM tunica has been observed to be under tension [28]. Moreover, curvature of an adult SAM is maintained over at least 36 hours (demonstrated in Figure 3.3 A-E). To calibrate in the model the impact of tension on the SAM boundary, we use r_{Ex}, the experimentally observed average SAM curvature (calibrated in Section 3.1.10). The boundary forces are applied in the model

to the boundary cells in the tunica, and are directed in order to promote the experimental curvature of the SAM.

Specifically, the force F_{Boundary} represents the collective adhesion-propagated tension originating from the tissue lateral to the represented portion of the SAM. As such, forces are applied to the outward-facing nodes of L1 and L2 boundary cells (Figure 3.6 A), to obtain the experimentally observed SAM curvature r_{Ex} (see Figure 3.3 F). The direction of F_{Boundary} is determined by approximating the location of the SAM apex (x_A, y_A) and then defining the center of a circle whose curvature we want to calibrate the SAM to, and we call this center $\boldsymbol{x}_C = (x_C, y_C) \coloneqq (x_A, y_A - r_{\text{Ex}})$. Point approximations of the left and right boundaries of the SAM, denoted $\boldsymbol{x}_L$ and $\boldsymbol{x}_R$, are used to compute the direction of F_{Boundary} applied to all boundary nodes. The points $\boldsymbol{x}_L$ and $\boldsymbol{x}_R$ are calculated as the midpoint of the centroids of the L1 and L2 boundary cells on the left and right sides, respectively. Finally, the direction assigned to F_{Boundary} is taken to be the outward facing perpendicular direction to the lines $\overline{\boldsymbol{x}_L\boldsymbol{x}_C}$ and $\overline{\boldsymbol{x}_R\boldsymbol{x}_C}$ (Figure 3.3 F-G. In this way the radial component of F_{Boundary} relative to $\boldsymbol{x}_C$ will act to pull the boundary cells inward, promoting the prescribed curvature r_{Ex} (Figure 3.3 G). Throughout a given simulation, the force magnitude is maintained as constant. This was chosen from a biologically-relevant range derived experimentally in detail in Section 3.1.10.

3.1.4 Chemical distribution controls growth and division rate of cells

Cells in the model are assigned concentrations of WUSCHEL ([WUS]) and cytokinin ([CK]) using experimentally-calibrated concentration distributions as in [2]. As in the model published by [2]. Namely, WUSCHEL chemical signal controls cells' life cycle length, which is used to determine the rate at which cytoplasm nodes are added to a growing cell. In L1 and L2, values of [CK] are maintained at 0, since in wildtype experiments cells do not respond to cytokinin signaling. In deep-

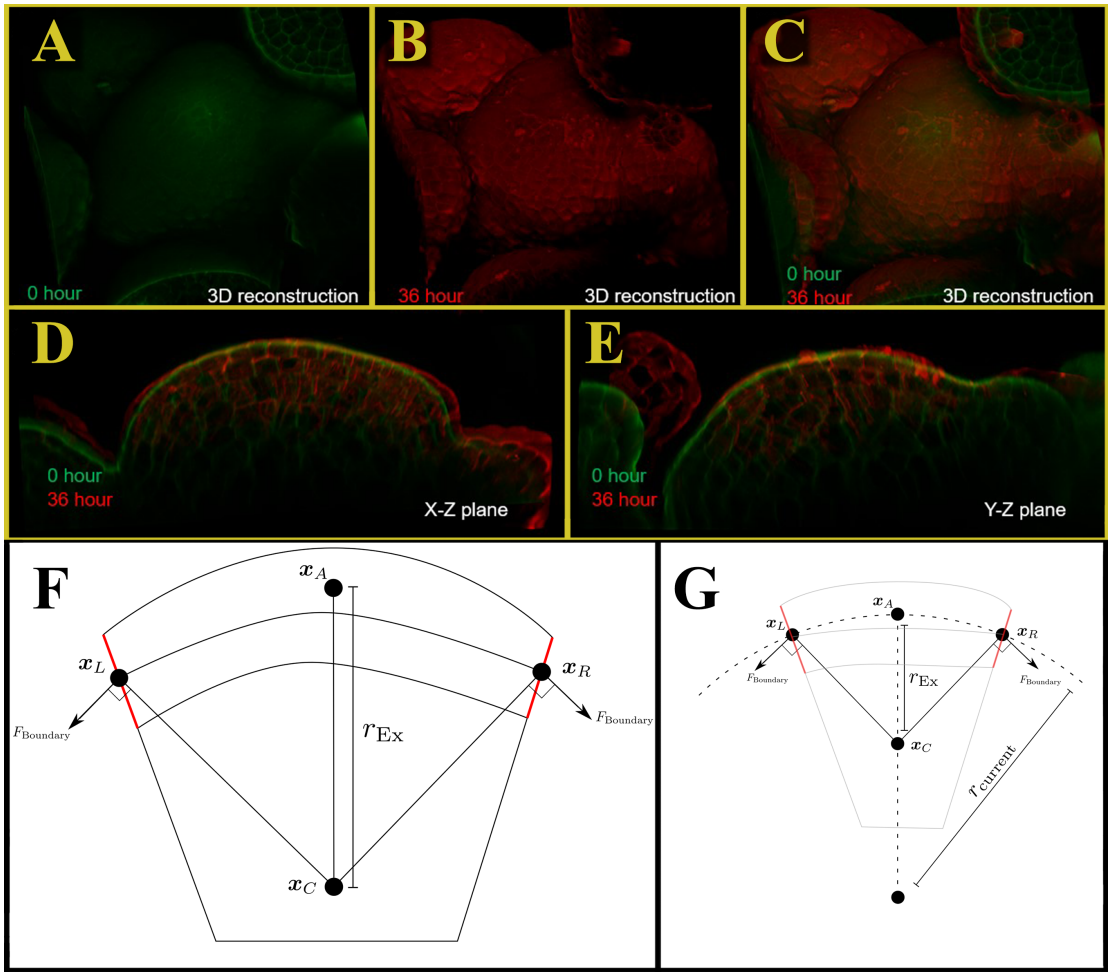

Figure 3.3: **Self-similarity of curvature over time is imposed by directed boundary tension.** (A-B) 3D reconstructions of time-lapse images of a SAM. Images taken (1) at t_0 and (B) at $t_0 + 36$ hours are shown in green and red, respectively. In (C), these two timepoints are superimposed. The SAM is approximately self-similar in over 36 hours with a maintained curvature. The approximation of the SAM curvature from experiments is detailed in SI section 3.1.12. (D-E) Two orthogonal longitudinal slices of the SAM generated from the 3D reconstruction in (C). (F-G) Directing the tension force of the SAM to promote experimentally observed curvature. (F) The apex of the model SAM is approximated, and from there $\boldsymbol{x}_C$ is calculated. Force is applied perpendicular to the lines $\overline{\boldsymbol{x}_L\boldsymbol{x}_C}$ and $\overline{\boldsymbol{x}_R\boldsymbol{x}_C}$. (G) When the simulation curvature, illustrated here as r_{current}, is not aligned with the experimental curvature, the radial component of F_{Boundary} relative to $\boldsymbol{x}_C$ acts as a corrective force.

layers (i.e. L3 or deeper) cytokinin and WUSCHEL concentrations are independently calculated using the expressions calibrated in [2]:

$$[\text{WUS}] = [\text{WUS}]_0 \exp\left(-\mu_{\text{WUS}}(r \cdot \alpha_{\text{WUS}})\right); \tag{3.9}$$

$$[\text{CK}] = [\text{CK}]_0 \exp\left(-\mu_{\text{CK}}(r \cdot \alpha_{\text{CK}})\right), \tag{3.10}$$

where r is the distance from the centroid of each cell to the "signal centers", which we introduce as point-approximations of the centers of the WUSCHEL and cytokinin expression domains.

Signal centers for WUSCHEL and deep-layer cytokinin are located two and three cell diameter-lengths, respectively, directly below the SAM apex (Figure 3.4 A) as observed in experiments. Parameters $\mu_{\text{WUS}}, \mu_{\text{CK}}, [\text{WUS}]_0$, and $[\text{CK}]_0$, which represent the maximum intensity of [WUS] and [CK] and their respective spatial gradients, were fitted to experimental wildtype data in [2]. Parameters α_{WUS} and α_{CK} are factors to simulate under/over-expression of signals as in experimental mutant conditions. The cell cycle length, denoted p_i, represents the amount of time between cell i's divisions. Cell cycle lengths are chosen as normally distributed random variables parameterized by [WUS]. The mean and standard deviation of p_i values for a given concentration of [WUS] were fitted to experimental data as in [2]. We define the cell progress, denoted CP_i for each cell i, as the portion of time elapsed after the last cell division. A new cell has $CP_i = 0$, and will divide when $CP_i = 1$. Cell progress for each cell in a simulated SAM is shown as a heat map in Figure 3.6 D.

Given the cell cycle length p_i, the total amount of time that cell i takes to divide, each cell's progress is updated throughout its life cycle as follows:

$$CP_i(t + \Delta t) = CP_i(t) + \frac{\Delta t}{p_i}.$$

Cell progress determines the number of cytoplasm nodes per cell, denoted as M_i,

$$M_i = \lfloor s_i + (f_i - s_i) \cdot CP_i^{\frac{2}{3}} \rfloor. \tag{3.11}$$

The exponent 2/3 is chosen due to the assumption that volume increases linearly in time for a given p_i. For a sphere, if a the volume $V \propto t$, then the cross sectional area $A \propto t^{2/3}$. At M_i increments, a new cytoplasm node is added at the cell's centroid resulting in an increase of the net outward force on the wall nodes and stretching them. New cell wall nodes are added between the most stretched pairs of adjacent wall nodes to drive irreversible expansion as in [2].

The parameters s_i and f_i represent the starting and final number of cytoplasm nodes in each cell, calibrated as coarse-graining parameters in [2] which determine the resolution of the model simulations. In 2D simulations, each cell begins at $s_i = 15$ cytoplasm nodes and divides once it reaches $f_i = 30$ cytoplasm nodes. In the P3D model, some cells are stochastically chosen to "expand out-of-plane" (i.e. represent the biological cells anisotropically expanding orthogonal to the longitudinal plane of the model, described in Section 3.1.8). We heuristically assume that the sections of cells expanding out-of-plane expand in the plane only half as much as those cells completely in-plane, and use $f_i = 22$. Additionally, if a cell expanding out-of-plane finishes its cell cycle, we reset its cell progress to zero and it retains all cytoplasm nodes in the section (i.e. we set its value of s_i for the next cell cycle to its previous f_i). In this way, a cell that is stochastically determined to expand and divide out-of-plane across multiple consecutive cell cycles will not further expand in the longitudinal section.

3.1.5 Preferential expansion of cells

In the plant, cells can influence the direction of their anisotropic expansion via the rearrangement of a structural girdle of microfibrils on the cell wall, which constrains growth in two directions, leaving the third orthogonal direction's expansion promoted. We represent this by making the bending spring's equilibrium angle $\theta^{\text{eq}}_{\text{Bending Spring}}$ heterogeneous within a single cell. The only exceptions are cells which are polarized out-of-plane (see Section 3.1.8) and cells in the simulation boundary, whose uniform cell wall mechanics are set such that wall nodes would reach a circular arrangement if the cell was in an isolated system.

Plant hormones WUSCHEL and cytokinin are assumed to influence cell growth polarization, with WUSCHEL promoting anticlinal growth and cytokinin promoting periclinal growth. A cell's growth direction is determined as in 3.1.6, with an example of the spatial distribution of cell growth polarization shown in Figure 3.6 B. Approximately every 4 hours of represented time, cells will reassess their growth polarization direction using their current signaling levels, and this time scale was based on observations of how long it takes cells to reorient their microtubules and respond to changes in chemical signaling. Nodes belonging to cells whose growth is polarized are given heterogeneous equilibrium bending angles, with values varied depending on whether the nodes fall within a cell's "sides" or "ends" (Figure 3.4 B-D). Nodes in model cells' sides are given $\theta^{\text{eq}}_{\text{Bending Spring}}$ which prefers a linear arrangement, while the equilibrium angles for nodes on the ends prefer a circular arrangement.

As in [1], we represent the expansion direction and division of the cells as being stochastically controlled by the relative concentrations of WUSCHEL and cytokinin. WUSCHEL is understood to promote anticlinal behavior, and cytokinin is thought to promote periclinal behavior. We paramaterize the probability mass function used to determine each cell's behavior via the expression:

$$\text{Prob(Cell follows periclinal behavior)} = \frac{1}{1 + \left(\frac{K_{\text{Hill}}}{[\text{CK}]/[\text{WUS}]}\right)^{N_{\text{Hill}}}};$$

$$\text{Prob(Cell follows anticlinal behavior)} = 1 - \text{Prob(Cell follows periclinal behavior)}.$$

3.1.6 Antagonistic signaling between WUSCHEL and cytokinin controls cell anticlinal and periclinal cell divisions

For this study, the values of K_{Hill} and N_{Hill} were the same as in [1] (and presented in Chapter 2 Section 2.1.6). In that work, the value of K_{Hill} was calibrated by assuming the center of the WUSCHEL and cytokinin's signaling domain had a 50% chance of expanding or dividing anticlinally

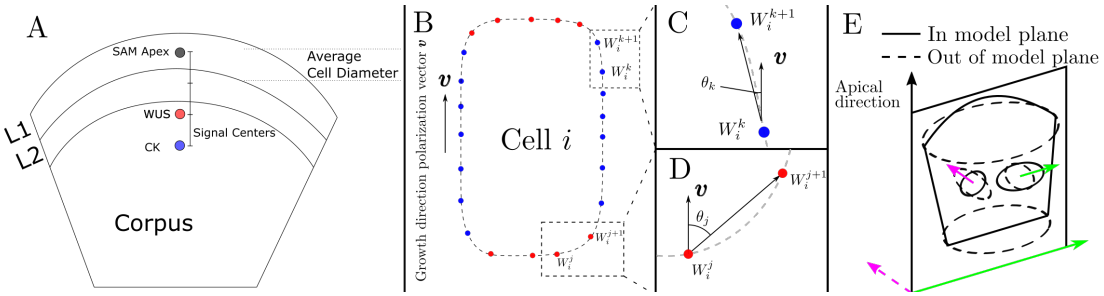

Figure 3.4: **Chemical Signaling and Cell Growth Direction Polarization.** (A) A schematic for positioning the signal centers for WUS and CK is shown. These centers, which determine signal concentration in all model cells, are placed two and three cell diameter lengths below the SAM apex. This positioning reflects experimental observations, and is implemented as in [1]. (B-D) A schematic for the model cell i is shown. If the cell is assigned a growth direction $\boldsymbol{v}$, the angle between consecutive cell wall nodes is used to determine whether cell wall nodes are assigned to be an end (red) or a side (blue). Once assigned, the mechanical parameters of those nodes will be modified to promote anisotropic expansion as in [1]. (E) Cells in the P3D model (solid rings) are stochastically assigned to grow and divide either along the SAM cross-section (green) or out of the model plane (magenta). The probability distribution for this assignment is discussed in Section 3.1.10. In the 2D model, all cells expand and divide in-plane (i.e. along the green axis).

or periclinally, since the apical corpus appeared unstructured compared to the basal corpus. The value of N_{Hill}, which controls how deterministic the response of cells to the relative WUSCHEL-cytokinin ratio is, was calibrated by matching the distribution of cell-scale features observed in simulations to those in wildtype experiments. This was accomplished by matching the proportion of anticlinally to periclinally expanded cells in the model SAM to the same frequency measured in experiments.

When model cells complete a mitotic cycle (i.e. reach $CP_i = 1$), they divide and CP_i is reset to 0 for the daughter cells. Cells growing out-of-plane (Section 3.1.8) only have one represented daughter - the other is treated as having grown out of the cross-section - and the represented daughter inherits all nodes and adhesion connections from the mother cell. All other cells divide in plane. Layer 1 and 2 cells are always prescribed to divide with a plane normal to the SAM surface as occurs in all wildtype SAMs. For deeper layers, each simulated cell follows the layer-specific division plane placement rule introduced by [1], wherein cells in the apical corpus orient their division plane with

respect to mechanical cues, and cells in the basal corpus orient their division plane stochastically with probability distribution parameterized by relative levels of WUSCHEL and cytokinin.

Two daughter cells inherit the cytoplasm nodes evenly and two sets of wall nodes separated by the division plane. A new row of wall nodes forms in each daughter cell parallel to the division plane, representing the new walls and middle lamella. Both daughter cells are considered to be part of the same layer as the mother cell, since the 40-hour time frame is short enough to have only between one and two rounds of cell division on average. It is important to note that this means that the behavioral differences between cells in the L1, L2, apical and basal corpus cells are considered as hereditary within each simulation.

3.1.7 Coupling submodels into a cell-based model

Computational implementation of the mechanical submodel of the SAM has the smallest time step among all submodels, with $\Delta t \approx 0.4s$ of represented time. The chemical division submodel is run every time a cell cycle completes, and the distributions of cell cycle lengths were experimentally calibrated in [2], and their implementation is discussed more in Section 3.1.4. We assume that division occurs at the end of each cell cycle as in [1]. Simulations were run to represent 40 hours as in [1, 2]. Coupling of the mechanical and chemical signaling submodels in space is achieved implicitly through the common use of the same spatial scale (i.e. the micron-scale) and the "signal center" (Figure 3.4 A), whose positioning is determined by the size of cells from the mechanical submodel. For the pseudo-3D submodel, horizontal displacement of cell centroids from the apex of the SAM was used to categorize each cell as a central or peripheral zone cell which, along with the cell layer, determines the probability of that cell growth polarizing along or out of the plane.

3.1.8 Description of a pseudo-3D model

The apical surface of the SAM (perpendicular to our cross-sectional plane) has a radial symmetry (see Section 5.4), and so we assume in the model that some cells are preferentially ex-

panding perpendicular to our cross-section. If anisotropic expansion were to occur only in-plane, the 3D tissue would lose this radial symmetry as it elongated preferentially in that plane. Thus, in P3D model simulations, we label the cells as having growth direction polarized out-of-plane (i.e. growth direction polarized perpendicular to the longitudinal section) or in-plane (along the model cross-section), as in Figure 3.4 E.

In the P3D model, we also treat out-of-plane polarized cells as growing isotropically - i.e. we assign wall nodes of these cells uniform mechanical parameters, unlike those for the anisotropically expanding cells. Cells in the 3D biological system anisotropically expanding out-of-plane will have their longest axis orthogonal to the longitudinal section. We represent this in P3D by giving out-of-plane expanding cells a smaller longitudinal sectional area than those polarized along the model plane ($\approx 25\%$ smaller), since only their minor axis will be shown explicitly in simulations. When a cell growing out-of-plane completes its cell cycle, one daughter cell does not fall within the cross-section and is not represented explicitly in the simulation. Whenever an in-plane cell divides (Section 3.1.6), both of its daughter cells are assigned to have their growth polarized either in-plane or out-of-plane with probability distributions as discussed in the next paragraph. Similarly, an out-of-plane expanding cell whose cell cycle finishes only has one daughter represented in the model (or, from a computational standpoint, does not divide) and the represented daughter cell again has a randomly assigned probability to expand either in-plane or out-of-plane by a probability distribution described in the next paragraph. Lastly, cells expanding out-of-plane have a terminal expansion size smaller than those in-plane, heuristically assigned to grow only to $f_i = 23$ instead of $f_i = 30$ for in-plane cells (Section 3.1.4).

Experimental data suggests that the fraction of cells whose growth direction is polarized out of a longitudinal plane intersecting it is distinct between the central and peripheral zones. To quantify this, 450 cell divisions in wildtype SAMs were observed and the division planes were manually classified as either radial or tangential, and a frequency distribution was obtained for cells in the central and peripheral tunica and corpus. Section 3.1.10 details the experimental measurement

of this frequency distribution. These frequencies were then used in P3D model simulations as a spatially heterogeneous probability distribution to choose which cells in each zone grow out-of-plane for their entire cell cycle. An example of a P3D simulation showing which cells are growing in and out-of-plane is provided in Figure 3.6 C and Supplemental Video S1.

3.1.9 Initial conditions

The mechanical submodel is given an initial, wedge-shaped tissue layout as shown in Figure 3.5 A. The top layer of cells are considered, L1, the next are L2, the third and fourth are the apical corpus cells, and the fifth and sixth are the basal corpus cells. The bottom layer cells are considered part of the stem, and are given very high damping coefficients to represent their stiffened, partially differentiated state. This initial layout was developed and connected to the biological context in [1].

Each cell is initially circular and is given a uniformly random initial value of CP_i (Section 3.1.4). In each simulation, the cells are stochastically chosen to begin as growing in-plane or out-of-plane with the probability distribution described in 3.1.10, determined by their centroid positioning. From this, we can determine the initial number of cytoplasm nodes M_i, and each cell is initialized with a number of wall nodes $N_i = 100 + 2M_i$. Adhesion partners are formed based on proximity to neighboring cells' wall nodes.

The cells along the sides of the simulated SAM are marked as boundary cells, and do not divide upon the completion of a cell cycle. They expand with uniform mechanical parameters, so as not to promote anisotropy in any preferred direction. Nodes on the distal portions of the L1 and L2 cells are marked as "boundary nodes", and are the nodes to which all tension forces are applied (Figure 3.5). Cells along the bottom of the SAM are considered to be the differentiating cells in the stem, which are expanding vertically and given a vertical anisotropic expansion direction, as observed in experiments. To represent the increased rigidity of more differentiated cells in the stem, the nodes in the bottom layer of cells are given a stiffer value of η_i by an order of magnitude.

The entire simulation has two stages. Stage one is a brief elastic relaxation phase, and occurs rapidly within the first 15 minutes of simulated growth. During this stage, we allow the cells to re-assign their adhesion neighbors very frequently, which effectively allows cells to "slide" along one another to achieve a state of mechanical equilibrium. The bulk of the simulation occurs in stage 2, which subsequently begins from the equilibrium state illustrated in Figure 3.5 B. In this stage adhesion neighbors only update their adhesion partners once every 6 hours. This causes the cell neighbor structure to be much more rigid, since cells are not observed to slide relative to one another easily in the experimental context.

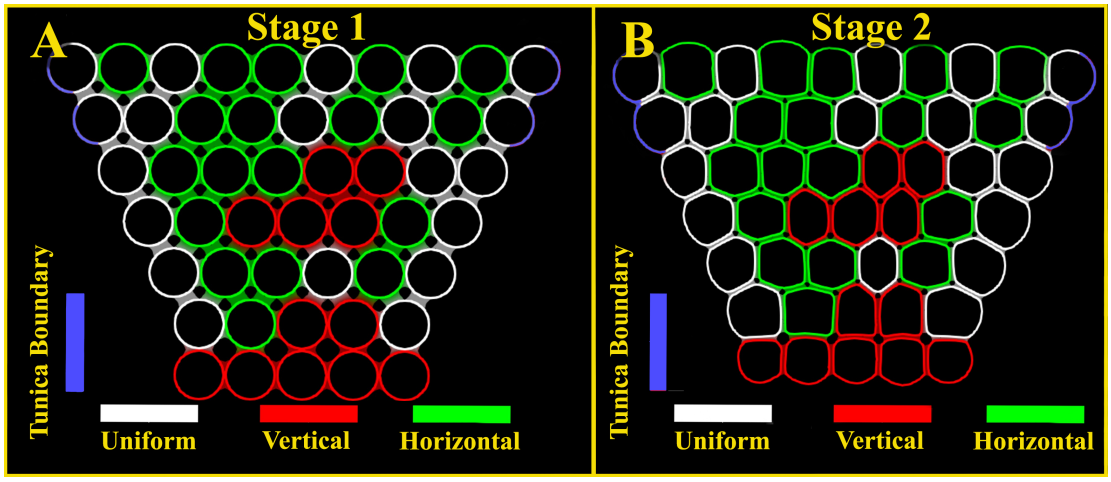

Figure 3.5: **Initial conditions and equilibrium state.** (A) 50 model cells and their initial adhesion connections between neighboring cell wall nodes are shown in the initial layout used for each simulation. (B) An example of an equilibrium state achieved after stage one of simulations. (A-B) Note that in the equilibrium state, each cell has been stochastically assigned a direction of cell growth polarization, leading to anisotropically expanded cells at mechanical equilibrium. Cells on the left and right sides of the simulated tissue domain are the boundary cells which do not divide in any stage of the simulation, but otherwise obey the same rules as other cells. Cells in the bottom most layer are considered part of the stem, and have a much higher damping to provide a foundation for the expansion of the SAM. Coloration of red, green and white shows the stochastically chosen growth direction polarization direction of each cell. Nodes in blue show the tunica boundary nodes, to which F_{Boundary} is applied during both stages.

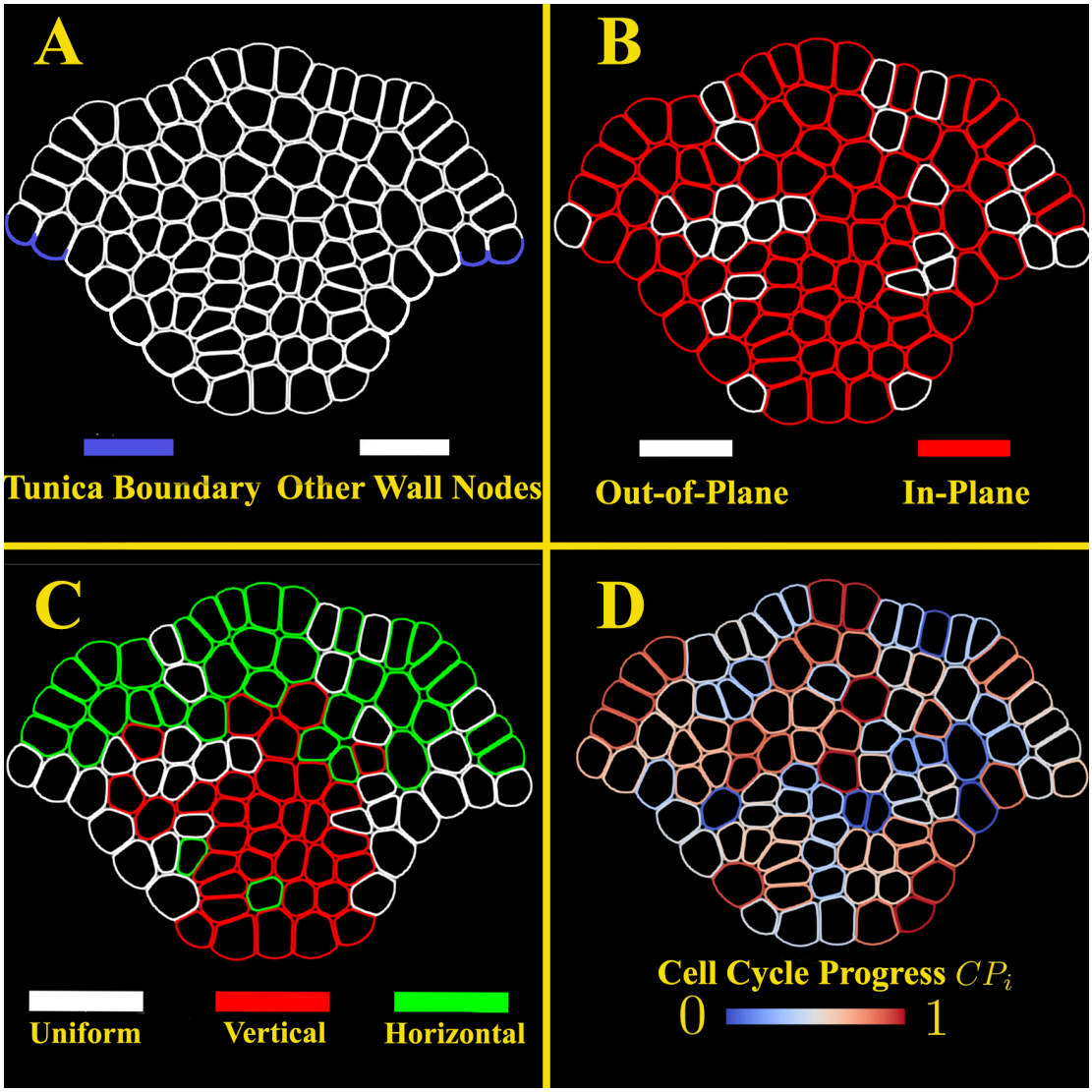

Figure 3.6: **Cell Properties During Simulations.** Four different properties of nodes and cells given as color mapping. All panels depict different features for the same simulated P3D SAM during a single timestep. (A) Boundary nodes are shown in red. Once the direction for F_{Boundary} is determined as in Section 3.1.3, each boundary node is pulled in that direction with magnitude $|F_{\text{Boundary}}|$ / # boundary nodes. All non-boundary wall-nodes are white, and cytoplasm nodes are not rendered. (B) Cells expanding out-of-plane (white) are chosen stochastically at simulation initiation and at the end of every cell cycle (details in Section 3.1.8). All other cells expand in-plane (red). (C) Cell growth directions are shown. Cells whose nodes are green (red) are preferentially expanding anticlinally (periclinally). Cells preferentially expanding out-of-plane or boundary grow with uniform mechanical properties along their wall (white). (D) Cell progress CP_i is shown for each cell. Cells with smaller values of CP_i have recently finished a cell cycle, whereas cells with larger values of CP_i are about to finish a cell cycle.

3.1.10 Model calibration

Estimation of F_{Boundary} magnitude. In [28], the SAM studied under the assumption that it behaved as though it was a pressurized shell, providing a justification to relate the tension-induced pressure directly to modified boundary conditions applied to the SAM. Section 3.1.11 derives the following expression for the boundary conditions based on the pressure experienced by the SAM P_0, the average width of a cell w, and the radius of a sphere which approximates the SAM surface r_{Ex}:

$$|F_{\text{Boundary}}| = \frac{r_{\text{Ex}}}{2} \cdot w \cdot P_0. \tag{3.12}$$

The radius of curvature $r_{\text{Ex}} = 80.1\mu m$ was chosen by selecting the L1 cells from segmented 3D experimental images, fitting a sphere to them, and taking the average radius for 17 wildtype SAMs. The value of $w = 7.04\mu m$ comes from measuring the diameter of each cell in the SAM in the direction normal to the longitudinal plane (see Chapter 5 Section 5.4 for experimental details and Section 3.1.12 for analysis methods). The value of $P_0 \in [0.66, 0.98]MPa$ was taken from literature [28].

These values applied to equation 3.12 yields $F_{\text{Boundary}} \in [187.54, 278.47]\mu N$. When running simulations, we call $187.54\mu N$ "low" force, $233.01\mu N$ "average" force, and $278.47\mu N$ "high" force. We examined the effects of running the simulations with inordinately large tension magnitudes using $557.95\mu N$ as "2X" force. If we set $F_{\text{Boundary}} = 0$, we call this the free boundary condition.

Calibration of the out-of-plane expansion frequency. To calibrate the frequency of cells growing out of plane, previously reported live time-lapse of plants expressing a fluorescent nuclear reporter (35S::H2B-mYFP) [107] were used to analyze cell division orientation in distinct zones of the SAM. Registration of time series of 512 x 512 x 20 images using Fijiyama on ImageJ were used to align the nuclear reporter construct across the time series imaged every 1-1.5 hours. Image slices capturing the layer 1, layer 2, apical corpus, and basal corpus were isolated manually in Adobe Photoshop. Superimposing two sequential time series allowed for the manual identification of the new nucleus after divisions.

Table 3.2: **Frequency of out-of-plane divisions by functional zone.**

Region	Probability of out-of-plane growth polarization
Central Zone Tunica	47.4%
Central Zone Apical Corpus	17.8%
Central Zone Basal Corpus	10.5%
Peripheral Zone Tunica	43.4%
Peripheral Zone Apical Corpus	29.0%
Peripheral Zone Basal Corpus	18.2%

These nuclei were manually classified to be aligned radially (both nucleus centers could be touched with a single radius line from the center of the SAM) or to be tangentially aligned (Figure 5.9). Additionally, the nucleus within an 8 cell diameter across the center were manually classified to be in the central zone (CZ) while cells outside this region were classified as divisions in the peripheral zone (PZ). This analysis gave us a region-specific calibration of the relative frequency of in-plane anticlinal divisions to out-of-plane divisions. It is important to note that in this method, it is difficult to accurately detect periclinal divisions, as the division planes may be parallel to and between z-stack slices. To remedy this, we also incorporated established frequencies of periclinal-divisions to in-plane anticlinal divisions taken from our previous work [1]. The final values used to parameterize probabilities of cell growth polarization out of the plane in pseudo-3D enabled simulations is in Table 3.2.

Other Parameter Values. Table 3.3 provides parameter values for all wildtype simulations. The X_{Pres} Morse parameters were calibrated to experimental single-cell area and perimeter values for our imposed $M_i \in [15, 30]$ values. The μ_X and $[X]_0$ values for WUS and CK were experimentally fitted in [2]. Values for α_X were defined to be 1 for wildtype, and varied by factors that replicated observed [CK] : [WUS] ratios.

Larger values of $k_{\text{Adh}}^{\text{lin}}$ and $\ell_{\text{Adh}}^{\text{eq}}$ had a strong effect on tissue-scale structure: smaller $k_{\text{Adh}}^{\text{lin}}$ caused cells to slide relative to one another more easily, and $k_{\text{Adh}}^{\text{lin}}$ was chosen to prevent cell-cell sliding. The adhesion equilibrium length $\ell_{\text{Adh}}^{\text{eq}}$ was chosen to be as small as possible while maintaining

Table 3.3: **Parameter values for simulations.** Parameters with values marked as $*$ are ranges described in more detail in the indicated sections.

Parameter	Value	Selection	Parameter	Value	Selection
μ_{WUS}	0.01573	[2]	U_{Turg}	45	[2]
μ_{CK}	0.01637	[2]	V_{Turg}	0	[2]
F_{Boundary}	$*$	See section 3.1.10	ξ_{Turg}	0.3	[2]
$[\text{WUS}]_0$	84.6	[2]	γ_{Turg}	0	[2]
$[\text{CK}]_0$	110	[2]	$U_{\text{V.E.D.}}$	53	Equilibrium $\approx l^{\text{eq}}_{\text{Adh}}$
$k^{\text{lin}}_{\text{Adh}}$	12	Cell geometry (see 3.1.10)	$V_{\text{V.E.D.}}$	0.2	Equilibrium $\approx l^{\text{eq}}_{\text{Adh}}$
$\ell^{\text{eq}}_{\text{Adh}}$	0.07	Cell geometry (see 3.1.10)	$\xi_{\text{V.E.D.}}$	0.103	Equilibrium $\approx l^{\text{eq}}_{\text{Adh}}$
U_{Pres}	95	Coarse graining	$\gamma_{\text{V.E.D.}}$	1.1	Equilibrium $\approx l^{\text{eq}}_{\text{Adh}}$
V_{Pres}	6.71	Coarse graining	$k^{\text{lin}}_{\text{Ext}}$	12	Calibrated in [2, 95]
ξ_{Pres}	0.8	Coarse graining	$\ell^{\text{eq}}_{\text{Ext}}$	0.9	Calibrated in[2]
γ_{Pres}	1.34	Coarse graining	$k^{\text{bend}}_{\text{M.F.B.}}$	12	[2, 95]
K_{Hill}	1.3	See [1]	$\theta^{\text{eq}}_{\text{M.F.B.}}$	π or $\frac{\pi(N_i-2)}{N_i}$	See 3.1.5
N_{Hill}	10	See [1]	p_i	$12-72$ hours	[2]

numerical stability, as the middle lamella is very thin in experiments. Volume-exclusion parameters $X_{\text{V.E.D.}}$ were chosen to give a very strong repulsive force with the same equilibrium length as $\ell^{\text{eq}}_{\text{Adh}}$, and to have negligible attractive force. Values of $k^{\text{lin}}_{\text{Ext}}$, $\ell^{\text{eq}}_{\text{Ext}}$ and $k^{\text{bend}}_{\text{M.F.B.}}$ represent the mechanical stiffness and extensibility of the primary cell wall, and were calibrated in [2, 95].

3.1.11 Deriving an expression for boundary tension magnitude

Our method of approximating the tension experienced by the tunica of the SAM is to approximate the epidermal cell layers by a sphere of radius r_{Ex} inflated by uniform pressure P_0. Our two-dimensional model represents a projection of a vertical "wall" of cells upon an apical-basal plane that they are intersected by. This assumption allows us to derive an expression which will allow us to calibrate boundary conditions from experimental data.

The derivation of our expression for calibration begins by assuming that the surface of the SAM is well-approximated by a sphere of radius r_{Ex}, and that the tissue represented by our SCE model is approximated by a "thick wedge" of cells. We assume that this wedge has thickness w in the direction orthogonal to the longitudinal plane, and the epidermal portion of this tissue forms a strip along the surface of the SAM. This strip-approximation of the surface of the model region is represented by the region D in Figure 3.7 A. In describing the boundary effect on cells in the L1 and

L2 cell layers, Beauzamy et al. argue that the SAM behaves as a shell that is inflated by a pressure P_0 [28] (for explicit values used, see Section 3.1.10).

Let us approximate the surface of the 3D SAM by a portion of a sphere, and approximate the apical surface of our SCE-represented tissue by a strip D with width w along that sphere (Figure 3.7 A. We can describe D with the following expression:

$$\begin{aligned} D &= \left\{x^2 + y^2 + z^2 = r_{\text{Ex}}^2,\ |y| \leq w/2, z \geq h\right\} \\ &= \left\{(\rho, \phi, \theta) \colon \rho = r_{\text{Ex}},\ \theta \in \left[-\frac{w}{2r_{\text{Ex}}}, \frac{w}{2r_{\text{Ex}}}\right], \phi \in [-C, C]\right\}. \end{aligned}$$

Note that h and C are arbitrary, as the result does not depend on the length of the strip.

Whereas the SAM *in vivo* is a three-dimensional tissue with a two-dimensional apical surface, approximation by a two-dimensional model of a medial longitudinal section means that the corresponding apical surface will be one-dimensional. We represent the force-per-area pressure on D by linear pressure along the surface of the 2D model. By assuming uniform pressure along the interior of the SAM, we can calculate the linear pressure experienced by the 2D model $P_\ell(\phi)$:

$$P_\ell(\phi) \coloneqq \int_{-w/2r_{\text{Ex}}}^{w/2r_{\text{Ex}}} P(\phi, \theta) r_{\text{Ex}} d\theta = \int_{-w/2r_{\text{Ex}}}^{w/2r_{\text{Ex}}} P_0 r_{\text{Ex}} d\theta = w \cdot P_0,$$

giving $P_\ell(\phi)$ in units of force per length. Since $P_\ell(\phi)$ is assumed to be uniform, it is constant by the above calculation, and we refer to it as P_ℓ. To obtain the tension experienced by the surface of the SAM, let us approximate the one-dimensional apical surface of the 2D SAM by a chain of N rigid segments of length ε attached end-to-end. These segments are pushed outward by pressure to form a portion of a regular N-gon. The boundary tension can be obtained by looking at the forces acting upon any segment and observing the free-body diagram (Figure 3.8 D Inset).

Since the mass of each segment is small and motion only occurs on the timescale of cell growth, we can assume that $\sum F \approx 0$ in all directions (i.e. - the same assumption for applying

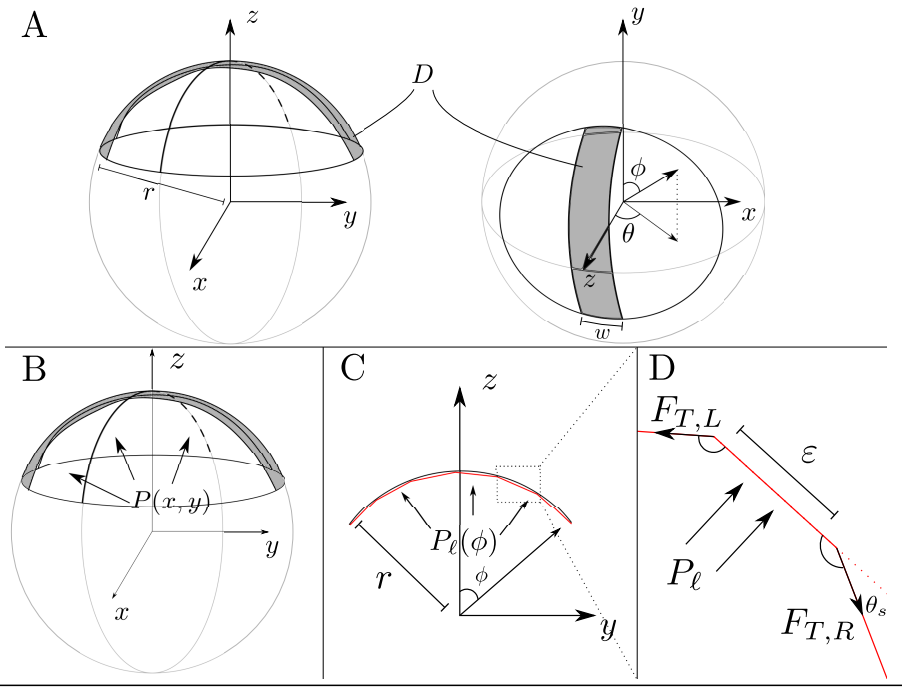

Figure 3.7: **Spherical approximation for the SAM surface to calculate $|F_{\text{Boundary}}|$.**(A) The surface of the SAM is approximated by a portion of a sphere; the region D corresponds to the epidermal portion of the SAM that we are representing in the subcellular element model. (B) Uniform outward-directed pressure on the SAM is represented by $P(x, y)$, acting as a force per unit area on the portion of the sphere representing the SAM surface. (C) Pressure on D is approximated in the sectional view as linear pressure P_ℓ pressing on an arc of a circle with radius r_{Ex}. In calculating mechanical equilibrium, this arc is discretized into multiple rigid, connected rods of length ε (D) Free body diagram for calculating $|F_{\text{Boundary}}| = |F_{T,L}| = |F_{T,R}|$, obtained by balancing the force of P_ℓ on segments with $F_{T,L}$ and $F_{T,R}$ of neighboring segments. Tension is obtained by sending $\varepsilon \to 0$

Langevin dynamics in the SCE model). Tension forces parallel to the segment are equal by symmetry (Figure 3.7 C), so we consider the forces normal to surface, $F_{\hat{n}}$:

$$\underbrace{|F_{T,L}| = |F_{T,R}|}_{\substack{\text{Equal magnitude} \\ \text{tension forces}}}; \; \sum F_{\hat{n}} = P_\ell \cdot \varepsilon - 2\,|F_T|\sin(\theta_s),$$

where θ_s is supplementary to the interior angles. By using the geometry of the N-gon, we obtain

$$\varepsilon = 2r_{\text{Ex}}\sin\left(\theta_s/2\right)$$

$$\theta_s = \frac{2\pi}{N}$$

and so we define

$$|F_{\text{Boundary}}| \coloneqq P_\ell \frac{\varepsilon}{2\sin(\theta_s)} = P_\ell \frac{2r_{\text{Ex}}\sin(\theta_s/2)}{2\sin(\theta_s)}.$$

We then send $N \to \infty$ to recover our circular geometry, thus $\theta_s = \frac{2\pi}{N} \to 0$ as $N \to \infty$, and the small-angle approximation of $\sin(x)$ gives us that

$$\begin{aligned} |F_{\text{Boundary}}| &= \lim_{N\to\infty} P_\ell \frac{\varepsilon}{2\sin(\theta_s)} = P_\ell \lim_{N\to\infty} r_{\text{Ex}} \frac{(2\pi/2N)}{(2\pi/N)} \\ &= \frac{r_{\text{Ex}}}{2} P_\ell \\ &= \frac{r_{\text{Ex}}}{2} \cdot w \cdot P_0. \end{aligned} \tag{3.13}$$

3.1.12 Obtaining r_{Ex} and w from experimental data

Both r_{Ex} and w are measured from 3D confocal micrographs as in Figure 3.8 A. 3D segmentation of the images were performed using the spherical harmonic method as described in the Chapter 5 Section 5.4.2. Reconstructed longitudinal sections were taken from the segmented SAM for five different longitudinal planes rotated about the SAM apex (Figure 3.8 C-D). The epidermal layer of cells was identified from each longitudinal section. A sphere was then fit to the collection of these L1 segmented cell boundaries using the "pcfitsphere" function in MATLAB's Computer Vision toolbox (Figure 3.8 E). It is important to note that this function's sphere fitting is robust to perturbations to the spherical assumption, such as the presence of primordia creating bumps on the surface of the SAM. The value $r_{\text{Ex}} = 80.11\mu m$ was taken as the average sphere radius over seventeen SAMs.

The value of w comes from the breadth of the strip that we are representing in the model. To measure this, we examined each of the L1 cells present in the five longitudinal planes taken for each SAM (blue cells in Figure 3.8 E). Each of these cells i then had its diameter d_i measured in the direction normal to the longitudinal section in which it appeared (Figure 3.8 F). The strip width w

for a SAM is the mean of d_i. The mean strip width for 17 SAM across 5 planes was used to obtain $w = 7.04\mu m$.

3.2 System-Specific Metric Definitions

Simulation outputs were collections of nodes' locations, signaling information, and identity within the tissue. What follows are the metrics applied to these data for model analysis. In all subsections, we refer to the centroid of a cell i as

$$(x_i, y_i) \coloneqq \frac{1}{N_i}\left[\sum_{j=1}^{N_i} W_i^j\right].$$

We gather these cells by layer ℓ, and define

$$\mathcal{C}_\ell \coloneqq \{(x_i, y_i) \colon i \text{ is in layer } \ell\}.$$

as the collection of cell-centers centroids in layer ℓ. Because we wish to decouple the effects of shape from size, we take C_ℓ and scale it so that all x-values are between 0 and 1. For this reason, we define the scaled centroids as

$$\begin{cases} \mathcal{C}'_\ell \coloneqq \left\{ \frac{1}{x^{\max} - x^{\min}} \left(x_i - x^{\min}, y_i\right) : i \text{ is in layer } \ell \right\} \\ x^{\max} = \max_{j\in\ell}\left(x_j\right);\ x^{\min} = \min_{j\in l}\left(x_j\right) \end{cases} \tag{3.14}$$

is the x-normalized set of cell centers.

Definition of Relative Curvature. To quantify the pronouncedness of the curved shape of the simulated SAM and have this measurement be decoupled from its absolute size and area, we fit a circle to the scaled set of centroids of the SAM's tunica (Figure 3.10 C). To be more specific, the x-scaled centroids of each cell in layer 1 $\mathcal{C}'_1$ are fitted with a circle of radius R using the least-squares fitting method. The relative curvature is $1/R$. In this way, the relative curvature is invariant under similarity transformations.

Monolayer Length of L1 and Layer Structure. The following describes a procedure to approximate the total length across the apical surface of the SAM. Though the method is simple and intuitive - tantamount to accumulating length while "connecting the dots" between nearest L1 centroid nodes - it is entirely dependent on the layered structure of the L1 layer of the tunica. Time discontinuity of this metric is sufficient to indicate the loss of the only assumption: the layer structure of the L1. While we do expect that over time tissue will expand and apical length will increase, the presence of sharp jumps (e.g. increasing by a factor of 1.2 in 15 minutes of growth) is sufficient to indicate the presence of a jump.

To approximate the monolayer length, we leverage the fact that the layer-1 boundary cells do not grow or divide. Let $1, \ldots, N_L$ be indices for all L_1 cells, and $k^{(1)} \in 1, \ldots, N_L$ be the index of the leftmost cell. If we assume that the layer structure of the SAM is intact, the next cell in the layer will be the cell with the closest centroid. The next cell in the layer will be the cell closest to that, and so on. So, we compute the distance matrix $(D)_{i,j} = |\boldsymbol{x}_i - \boldsymbol{x}_j|$, and define $k^{(2)}$ as the nearest neighbor of $k^{(1)}$, or more specifically, by $\min_{i \in \{1,\ldots,N_L\}} (D)_{i,k^{(1)}} = (D)_{k^{(2)},k^{(1)}}$. By sequentially finding the next nearest nodes without replacing our steps in this way, we can iterate by defining $k^{(i+1)}$ such that

$$\min_{j \in \{1,\ldots,N_L\} \setminus \{k^{(1)},\ldots,k^{(i)}\}} (D)_{j,k^{(i)}} = (D)_{k^{(i+1)},k^{(i)}} .$$

After all $k^{(i)}$ have been found, the monolayer length is calculated as

$$\sum_{i=1}^{N_L - 1} (D)_{k^{(i+1)},k^{(i)}} .$$

Now, if the layer structure of the SAM is preserved, then division of cells in the L_1 cell layer should have a small impact on the overall monolayer length. Moreover, since each node in the SAM simulation is moved continuously and on the timescale of cell expansion, any large-scale discontinuity of the monolayer length evolution in time is either a result of the breakdown of the assumption of layer structure, or is the result of a higher-order tissue deformation (e.g. a wrinkle or crypt forming in the SAM surface with a gap comparatively similar to a cell diameter). Since we have observed no

higher-order layer folding, we conclude that any substantial jump discontinuities of the monolayer length are indicative of a breakdown of layer structure, which has been confirmed to be the case in several simulated SAMs. For quantification, we assume that a $> 20\%$ increase of monolayer length within 1.4 hours of simulated growth indicates a breakdown of that SAM's layer structure.

Percentage of Periclinal Divisions. In the absence of cell motility within a tissue, the expansion and division of cells primarily drive the directionality of the SAM's expansion [2, 1]. The horizontal division of cells followed by the expansion of daughter cells is then a primary driver of apical-basal growth. As a measurement of this impact, we record the frequency of the periclinal divisions in order to quantify the SAM's apical-expansion driving behavior.

To capture this, information describing the timing and position of each cell division in simulations were recorded. This included division plane orientation and the tissue region of the dividing cell. Since the divisions in L1 and L2 were geometrically derived, our results report only divisions from the corpus of a simulated meristem.

The plane of every division j in the 2D model has a line, and let Θ_j be the acute angle between it and the radial axis (i.e. the horizontal axis). In experiments, the difference between the natural coordinate system (as described in [108]) and the global coordinate system given by the apical-basal axis (as used in [76]) should be small, since our model's consideration is restricted to the portion of the corpus subtending the central zone of the SAM. Still, there may be some disagreement, so when classifying division planes, we consider only divisions with $\Theta_j \leq 30^\circ$ to be periclinal, and divisions with $\Theta_j \geq 60^\circ$ to be anticlinal. Due to the model construction, the division planes in the tunica are of little mechanistic interest (barring the degradation of layer structure) since their division planes are prescribed geometrically to maintain layered structure. Moreover, division patterning in the apical and basal corpus are mechanistically distinct, so we treat the division data from those regions separately. Thus, from a chosen zone, we can define $P \coloneqq |\{j : \Theta_j \leq 30^\circ\}|$ and $A \coloneqq |\{j : \Theta_j \geq 60^\circ\}|$ from those divisions that occurred in that zone. Values of A and P were pooled

across replicates of simulated meristems with identical conditions and parameter sets. Percentage of periclinal divisions within that zone is returned as $P/(A+P)$.

3.3 Computational Model Predictions

The biologically calibrated P3D model maintains the monolayer structure of the SAM epidermis observed in experiments. In wildtype SAMs, the epidermal and subepidermal layers of the SAM (collectively called tunica) are maintained as clonally distinct layers. Failure to maintain these layers in the wildtype SAM results in misplacement of organs. However, in 2D model simulations initialized with these layers, the tunica's layer-structure deteriorates within 40 hours. In those 2D simulations, cells in the tunica tend to become highly compressed and elongated.

Local buckling of the layers pushes some cells out-of-layer by allowing its neighbors to form new connections above or below it. To quantify the proportion of SAMs whose layer structures can't be maintained within forty hours, we introduce and observe the time evolution of *monolayer length* of model simulated SAMs (Figure 3.9 A-B and Section 3.2 for technical details), which evolves continuously in time if a monolayer of cells is maintained.

Of 30 2D model simulations at each tension level (as defined in Section 3.1.10), 43% of SAMs exhibit monolayer disruption in the free boundary condition and 7-10% in the low, average, and high tension levels. Under the 2x tension condition, we did not capture any monolayer disruption in 2D simulations. In P3D simulations, only 7% of free-boundary SAMs exhibited monolayer disruption, and all samples maintained monolayer structure for any higher tension level.

This suggests that cells anisotropically expanding out-of-plane offsets structurally disruptive cell-cell crowding in the direction of the longitudinal plane. The only quantifiable instances of monolayer breakdown in P3D simulations were under the free boundary condition, which demonstrates that there is a stabilizing effect of experimentally-calibrated boundary forces on the layered tunica structure of the SAM.

Tunica cell shape distribution is sensitive to cell-cell crowding without considering out-of-plane growth. To further examine the crowding of cells in the epidermal and subepidermal cell layers which may disrupt cell monolayer structure, we calculated the cell aspect ratio distributions in the L1 and L2 cell layers, the apical corpus, and the basal corpus. The aspect ratio of a cell is defined as the ratio between cell length along its longest axis and its length in the perpendicular direction as in [1], and it is used as a measure of cell elongation. The mean aspect ratio of cells in the L1 and L2 is larger in 2D simulations than in P3D simulations for any tension level (Figure 3.9 C-E). The large aspect ratios obtained in the 2D simulations are symptomatic of individual cells being "squeezed" into an elongated shape due to cell crowding in the same layer.

This is significantly reduced by out-of-plane expansion in the P3D model (Tukey HSD test shows $p < 10^{-15}$ for the L1 impact and $p < 0.01$ for the L2 impact). Moreover, L1 cells in the 2D model showed no significant differences in aspect ratio between any levels of tension that were tested pairwise, with the exception of the 2X boundary force condition. In the P3D model, increasing tension provides a significant decrease in the aspect ratios of tunica cells (Figure 3.9 C-D). This indicates that without accounting for 3D cell anisotropic expansion, the individual cell shape is dominated by cell-cell crowding. We neither observed nor expected substantial changes in the basal corpus, since the division plane orientation of cells in the basal corpus is determined by signal concentrations that were not perturbed in these tests.

Tissue shape and apical corpus cell shapes are robust to mechanical perturbation. We noticed that the impacts of model choice (2D vs. P3D) and varying the magnitude of boundary forces on the distribution of cell aspect ratios were restricted to the tunica, with no significant differences in the corpus (Figure 3.9 E).

We then sought to determine whether the tissue-scale shape was also robust to these factors. Tissue shape was quantified by introducing and calculating relative curvature, which captures the shape of the SAM while being agnostic to the absolute size of the simulated tissue (Figure 3.10 C

for a diagram and Section 3.2 for formulation and details). Figure 3.10 shows that most simulated SAMs from both the P3D and 2D models approach the same relative curvature value by 40 hours. Simulated SAMs that do not reach the same relative curvature in 40 hours were obtained in the P3D model, and this is due to the reason that lower in-plane division rate in the P3D model simulations results in a slower rate of convergence of P3D model simulated SAMs to their calibrated curvature.

Moreover, as the magnitude of boundary force increases, the variance of the relative curvature of the SAM decreases significantly. Relative curvature variance decreases from 0.06 under the free boundary condition to 0.005 under the 2X force condition (Section 3.1.10). Figure 3.10 B shows that increasing the magnitude of boundary force increases the rate at which the curvature of the SAM is established. However, it is noteworthy that mean relative curvatures of 2D and P3D free-boundary condition model simulated SAMs at 40 hours is very similar to the simulated SAMs subjected to boundary forces (recalling that these forces act to restore the SAM curvature towards r_{Ex}, described in 3.1.3). These observations together with the robustness of apical corpus cell aspect ratios, suggest that there may be a regulator of cell and tissue shapes. We suspected that this regulation is an emergent property of mechanically determined division plane orientation in the apical corpus, motivating our investigation in the following sections.

The apical corpus mechanical division mechanism regulates cellular and tissue shape. To investigate whether cell division plane placement is compensating for mechanical perturbations, we analyzed division plane patterning via calculation of the percentage of periclinal divisions (measurement specifics in Section 3.2). The division planes in 150 2D simulated SAMs' apical corpus divide at 52.1% periclinal frequency and in 150 P3D simulations divide with 47.5% periclinal frequency (two-way ANOVA, $p < 0.002$). Both 2D and P3D model simulation percentage-periclinal means are within the confidence bounds determined in our previous experimental study [1]. This change in division patterning, which occurs while cell and tissue shape remain largely unchanged,

suggests that an emergent property of the mechanically-determined division plane placement in the apical corpus has the emergent property of regulating the cell and tissue shape.

Experimentally, this would be consistent with the fact that mutant SAMs, experiencing higher levels of CK (pCLV3::LhG4; 6xOP::ARR1-ΔDDK-GR) and also no CK (cytokinin receptor mutants), have substantially different shapes and division patterning [1]. In (pCLV3::LhG4; 6xOP::ARR1-ΔDDK-GR) mutants, the characteristic shape of the dome is observed to be qualitatively taller and more pointed and, on the cell scale, a clear deviation from wildtype division patterning is observed (Fig 3 from [1] for a representative). In *wus-1* mutants, division patterning also deviates to promote periclinal division, and the *wus-1* mutant meristem is notably flatter.

In order to confirm that there was a distinct structural difference between the simulated tissues in 2D and P3D models, we examined three more abstract quantifications of tissue structure patterning using the simulated SAM adhesion partner graph (Figure 3.11 A-C). This method has been used before for analyzing many types of tissues [109]. Centrality has been used as a measure of how important an individual node in a graph (or cell in a tissue, in this case) is for communication [109, 110]. This has been used in the SAM specifically to quantify the relative importance of any individual cell in diffusion-based signaling [21]. We chose to investigate the frequency distribution of three established types of centrality: *random shortest path betweenness centrality* (RSPB centrality) [111], *random shortest path betweenness net centrality* (RSPBN centrality) [111], and *PageRank centrality* [109].

The frequency distributions of the RSPBC and RSPBNC of cells in 30 SAMs were shifted significantly lower between 2D and P3D simulations (Figure 3.11; ANOVA test, $p < 10^{-15}$ for RSPBC, $p < 10^{-16}$ for RSPBNC). The PageRank centrality distribution of cells was significantly higher in P3D simulations (ANOVA $p < 10^{-15}$). While applying these metrics to the model simulations representing a longitudinal section of a tissue (as opposed to the full 3D tissue in vivo) is rather abstract, it indicates substantial differences in the patterning between the 2D and P3D models in addition to the percentage periclinal division patterning. Despite the marked difference in

tissue structure and division patterning, the tissue shape distributions (via relative curvature) and cell shape distributions (via aspect ratio) are robust to model selection.

Apical corpus structure is robust to perturbations of tunica structure. The percentage of periclinal divisions in the apical corpus in model simulations was robust to variation of tension magnitude up to and including double the biological maximum value (two-way ANOVA, $p > 0.1$). This means that even under substantial mechanical perturbation of the tunica, the mechanically-driven division patterning of the rib meristem remains unaffected. Values of RSPB, RSPBN, and PageRank centrality throughout the tissue were also unaffected by tension in the tissue, indicating a robustness of SAM's tissue structure to boundary tension.

The tunica cells are tightly adhered to the apical corpus cells, it is noteworthy that even under the 2X tension condition, there was no impact of the boundary forces on the shape or structure. This is in spite of the fact that the model apical corpus cells divide in response to local mechanical cues. This suggests that there is some other emergent phenomenon that prevents the effect of tension tangent to the SAM surface from propagating into the apical corpus structure.

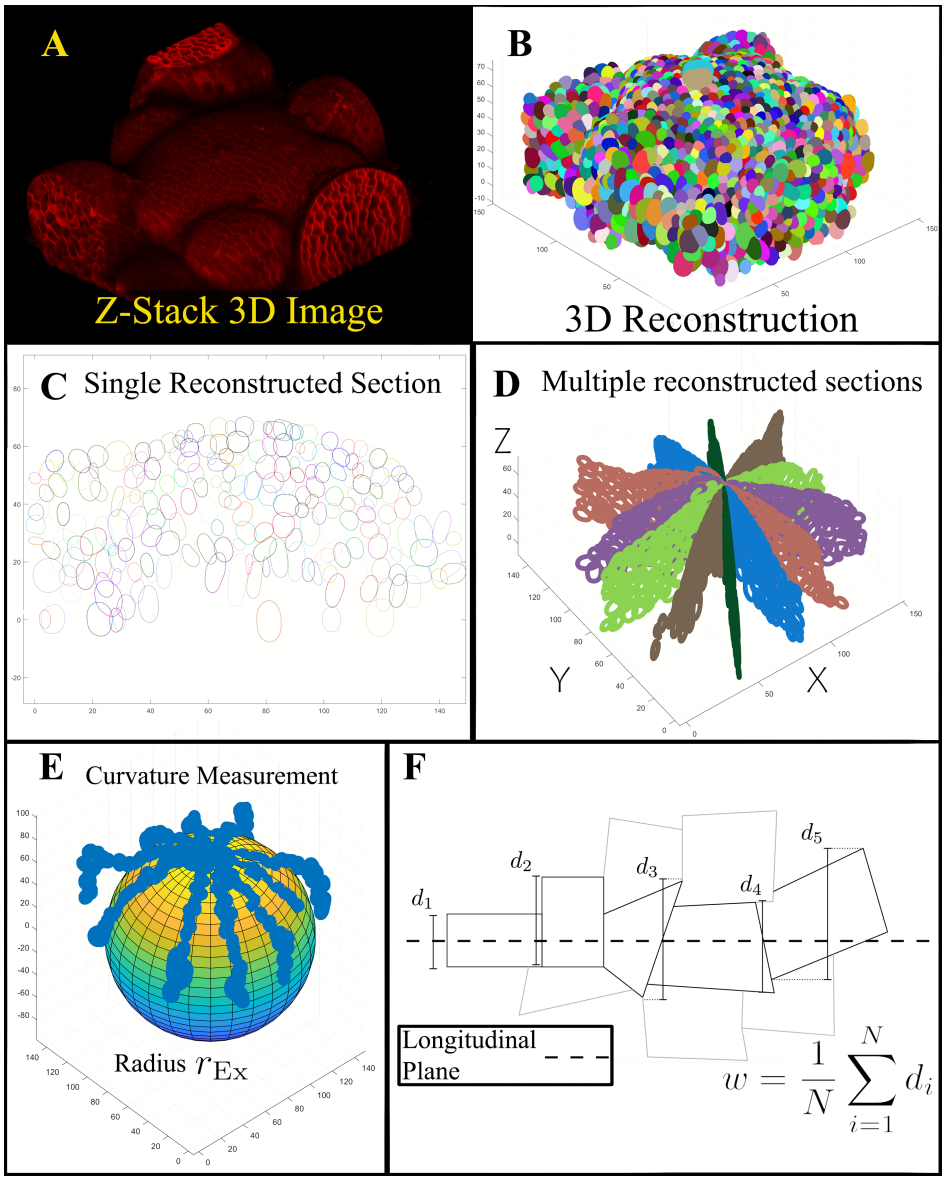

Figure 3.8: **Obtaining r_{Ex} and w from experimental data.** (A) 3D confocal micrograph of the SAM. (B) Corresponding output of the Spherical Harmonic Segmentation of the SAM. Each colored region in 3D is a cell that was identified via the segmentation mechanism. (C) Individual reconstructed section of a SAM with cell sections represented as rings. (D) Multiple longitudinal sections can be generated from the 3D reconstruction. The longitudinal planes are rotated about the (manually identified) SAM apex. (E) Cells in the L1 of each section were isolated in MATLAB (blue). A sphere was fit via the MSAC method, which identifies the best-fit sphere which is robust to the presence of primordia bulges. (F) To measure w, Experimental cells i that appear in any of the longitudinal section from (D) have their width in the direction orthogonal to the plane, d_i, measured. The value for w is taken as the average of all d_i from 17 wildtype experimental SAMs.

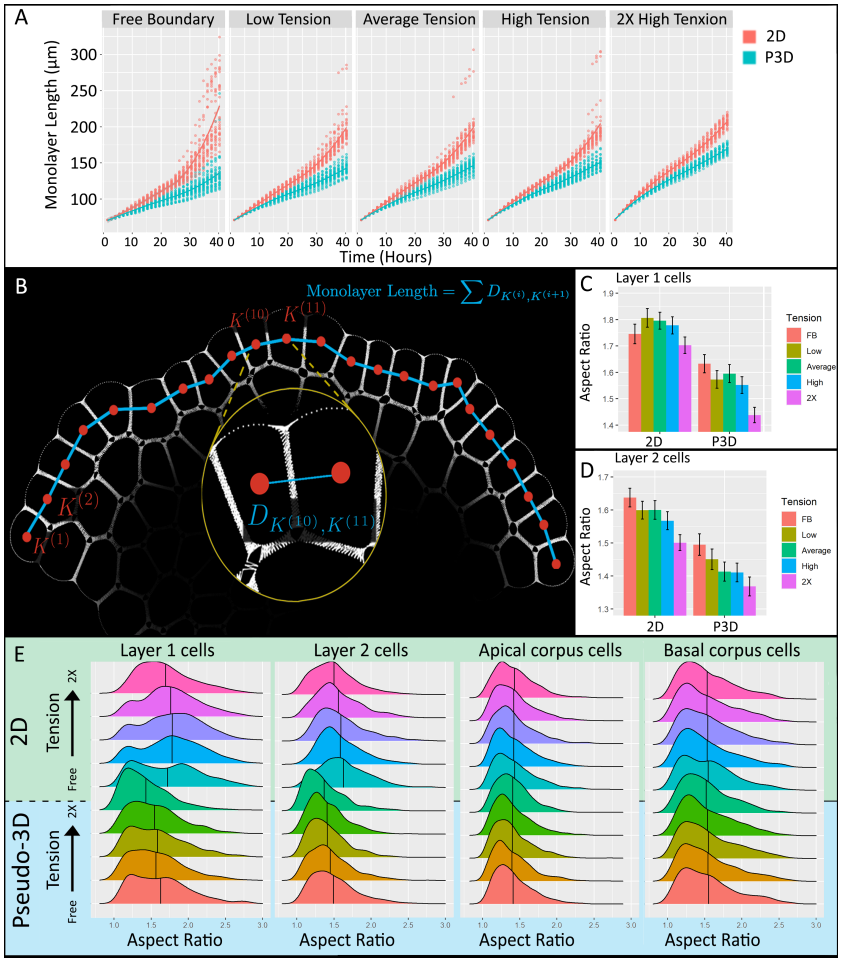

Figure 3.9: **Apical Surface Structure.** (A) Monolayer length of the SAM over time. Each panel shows longitudinal data from in-plane (red) and out-of-plane (blue) simulations under different tension ranges. Discontinuities are present in both 2D and P3D simulations under the free boundary condition, and only persist in the 2D simulations as tension increases. Jumps in the monolayer length are sufficient to indicate a break in L1 monolayer structure. (B) Schematic of the monolayer length. Details of this computation and its properties are in Section 3.2. (C-D) Mean aspect ratios of both the 2D and P3D model cells in layer 1 (C) and layer 2 (D). Error bars are 95% confidence intervals computed with the Benjamini-Hochberg correction. Conditions with non-overlapping error bars have statistically significantly different means ($p < 0.05$). (E) Frequency distributions of the aspect ratio of cells in layer 1, layer 2, Apical corpus, and Basal corpus. Each frequency distribution comprises cell aspect ratios from 30 simulated SAMs that were run to $40h$. In each column, the top five graphs (green region) are taken from 2D simulations, and the bottom five (blue region) are taken from P3D simulations. The five frequency distributions per region were generated under different levels of boundary tension, from Free boundary to 2X. Rounded cells have aspect ratio 1, while elongated cells have higher aspect ratios. Cells in the 2D simulations are tightly squeezed by their neighbors, increasing their aspect ratios.

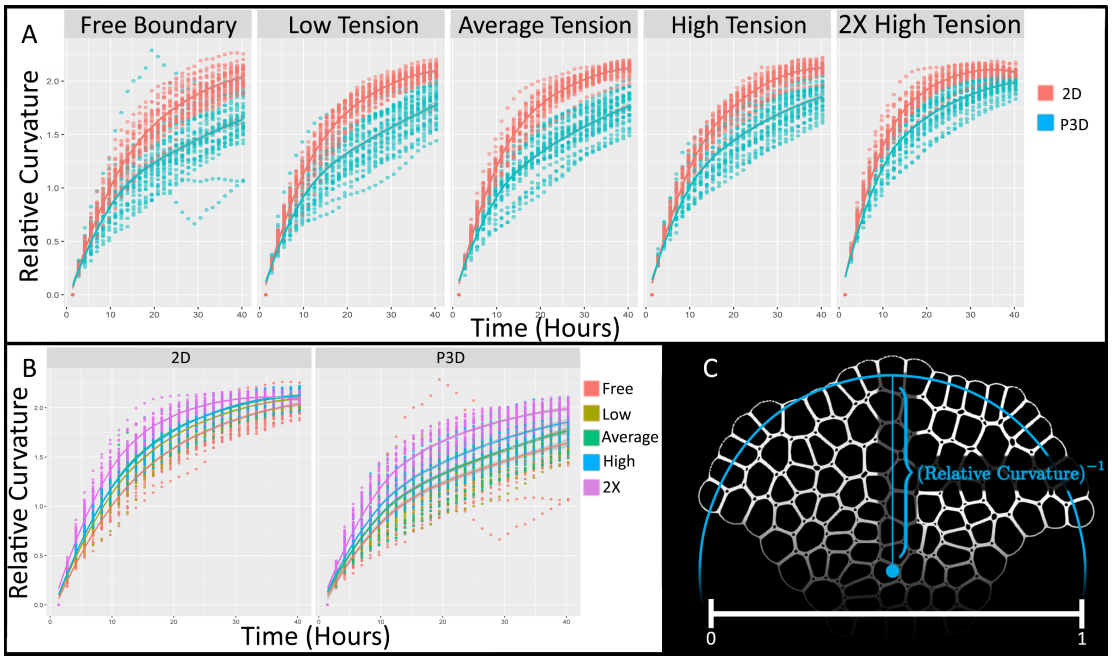

Figure 3.10: **Tissue shape is robust to P3D or 2D model selection and choice of boundary force magnitude.** (A-B) The relative curvature for 30 SAMs per tension level are shown for both 2D and P3D simulations. In each facet, the horizontal axis shows the timeline of the simulation. These data are shown in two ways, splitting data points between multiple graphs by (A) tension magnitude levels and (B) 2D and P3D simulations. In each graph, the vertical axis describes the curvature of the simulated SAM. Each facet shows the individual data points from 30 simulations, and the ribbons around each interpolated line show the standard error. Invisible or non-overlapping error ribbons for any point on the horizontal axis represent significant differences between the faceted populations at that time with $p < 0.05$. (C) Schematic of the calculation of relative curvature (details in Section 3.2. To investigate shape while remaining agnostic to absolute size, the SAM is scaled down to width 1.

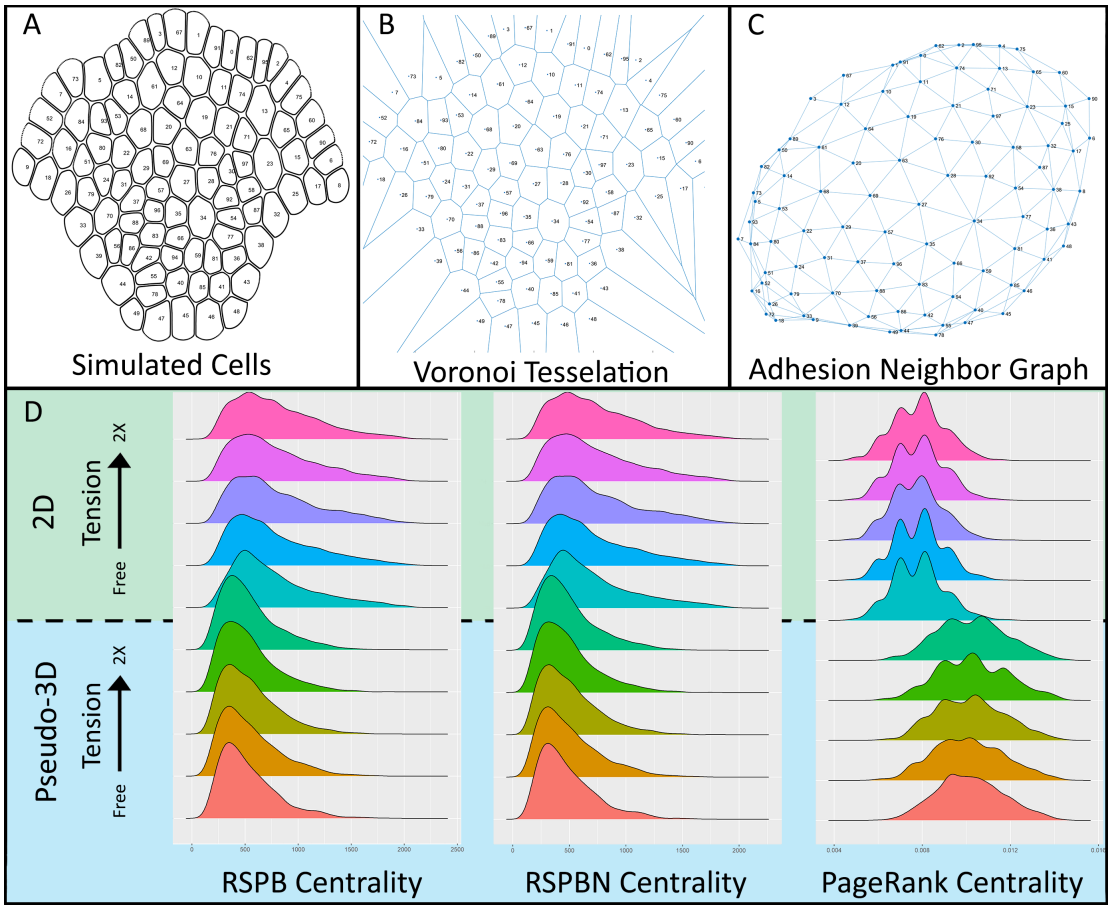

Figure 3.11: **Impact of pseudo-3D behavior on tissue structure.** (A) Cell wall nodes from a simulated SAM are shown in blue. An arbitrary label is placed on its centroid. (B-C) A voronoi tessellation (B) was performed on each centroid to extract the adhesion neighbor network (C). (D) Frequency distributions of RSPB random-walk centrality, RSPBN centrality, and Pagerank centrality of cells taken from simulated SAMs at $t = 40h$. Centrality values were pooled from 30 SAMs from each tension-level in both 2D (green region) and P3D (blue region).

Chapter 4

Computational Model Implementation and Code Availability

4.1 Code Availability each model

Computational model code for the model presented in Chapter 2 is available at https://github.com/ICQMB/Combined-signaling-and-mechanical-mechanism-maintains-the-structure-and-shape-of-the-SAM.git. Computational model code for the 2D and Pseudo-3D model presented in Chapter 3 is available at https://github.com/cmich004/ScePlantCells_Parallel/tree/division.

4.2 Code Structure

The object-oriented C++ code from each model follows the same hierarchical structure. "Wall Node" and "Cytoplasm Node" objects are endowed with member variables containing their coordinates in $\mathbb{R}^2$, as well as variables for the local mechanical parameters (e.g. k_{bend}). Wall Node objects, in particular, have a doubly-linked list structure which endows Wall Nodes with a neighborhood structure. Each Wall Node and Cytoplasm Node belongs to a "Cell" object, which also contains cell-scale variables such as CP_i, anisotropic expansion direction v, and signal concentrations. Cells have member functions which allow them to label and modify node, e.g. heterogeneously assigning mechanical properties to wall nodes as described in Chapter 3 Section 3.1.5. Cells belong to a single "Tissue" object, whose member functions loop through every cell and executes tissue-scale model components, such as assigning [WUS] and [CK] values to simulated cells. Stage 2 of the simulation begins at $1.1h$, or $T_i = 10,000$; simulations follow Stage 1 behavior for $T_i < 10,000$. Pseudocode for the main loop is given in Algorithm 1. Components unique to the pseudo-3D model components are indicated as such in the pseudocode.

Algorithm 1 Main program to execute model simulations.

Require: input parameters P

Define tissue $T = T(P)$ ▷ This implicitly defines all initial cells and nodes.

Initialize adhesion neighbors and signal concentrations in all cells

Determine which cells are expanding out-of-plane, if running the P3D model

for E **do**ach timestep T_i

    Update chemical signals and cell anisotropic expansion directions every $4.4h$

    if Stage 2 is in progress **then**

        Add new wall to cells every $7min$ if tensile stress is sufficiently high

    end if

    if Stage 1 is in progress **then**

        Update adhesion connections between nodes every $7min$ ▷ This allows cell-cell sliding

    else Stage 2 is in progress

        Update adhesion connections between nodes every $5.5h$

    end if

    if $T_i = 0$ **then**

        Identify nodes on simulation boundary to experience F_{Boundary}

    end if

    if Stage 2 is in progress **then**

        Update CP_i for each cell i

        Divide cells if $CP_i \geq 1$. If so and in the P3D model, determine the anisotropic expansion direction for the next cell cycle.

    end if

    Calculate all forces experienced by nodes. Store $\sum \nabla E$ as member-variables in each node

    Update cell locations using the forward Euler method

    Print output for time-series metrics

end for

Due to the computational demand of these simulations, CPU parallelization was implemented using the OpenMP API, distributed through the GNU Compiler Collection. We used this method to parallelize all functions that occur for each cell independently. Notably, lines 7, 10, 12, 18, 19, 21, and 22 in Algorithm 1 while synchronizing threads between each of these lines. We ran this simulation via parallelized CPUs since many cell-scale functions are not easily GPU-parallelized in many cases, due largely to (1) the heavy reliance upon the linked-list structure of cell wall nodes, (2) the difference in calculations between Cytoplasm and Wall nodes for each cell, and (3) the heterogeneity of the number of adhesion neighbors that each wall node possesses.

Chapter 5

Experimental and Image Analysis Methods Used for Calibration of the Models

This chapter contains the experimental methods and image analysis techniques used in this dissertation. All experimental methods were designed and performed by G.V. Reddy, Kevin Rodriguez, and Alexander Plong at the Reddy lab at U.C. Riverside. Image analysis techniques were selected and configured by Amit K. Roy-Chowdhury his graduate student Calvin-Khang Ta. Output of image segmentation methods were analyzed by Christian Michael and Calvin-Khang Ta. Section 5.1 in particular is a reproduction of the experimental methods used in [1]. The text of Sections 5.2-5.3 are reproductions of the supplemental information of [1], and were written primarily by myself with assistance from Mikahl Banwarth-Kuhn, Calvin Khang-Ta and Kevin Rodriguez. Figures 2 and 7 and their captions in this chapter were primarily created by Christian Michael.

5.1 Experimental methods used in the 2D modeling study

5.1.1 Plant growth and genotypes.

Plants were grown on 0.5X MS media in plates at 25°C under continuous light for 7-8 days. The null mutants in this study: WUS null mutant - *wus1-1* [69] and cytokinin triple receptor mutant - *cre1-12; ahk2-2; ahk3-3*[112] have been previously described. Transgenic plants containing fluorescent reporters for the WUS protein *pWUS::eGFP-WUS* [66] and cytokinin signaling reporter *pTCS::mGFP-ER* [71, 72] have also been previously described. A two component system, consisting of a LhG4 transcription factor driven from *CLAVATA3 promoter* constitutively activating the 6xOP promoter, and a dexamethasone (Dex) inducible rat glucocorticoid receptor (GR) were used for ectopic misexpression of the WUS protein *pCLV3::LhG4;6xOP::eGFP-WUS-GR* [61] and CK signaling *pCLV3::LhG4;6xOP::ARR1-*Δ*DDK-GR*[68]. For induction of ectopic expression, seedlings were transferred to 0.5X MS plates containing 10 μM Dex (Sigma) for 48 hours.

5.1.2 Imaging

Seedlings were embedded in molten 4% agarose and then chilled in an ice bath. Longitudinal hand-dissections, using polished blades (FEATHER), were done through the seedling and the supporting agarose. Samples were then submerged in plasma membrane stain, FM4-64, for 10 minutes and imaged with a 40x objective lens on the Zeiss LSM 880 and Leica SP5 confocal microscopes. For 3D analysis of cells, the inflorescence meristems were stained with FM4-64 and confocal cross sections were obtained by acquiring z-stack on the Zeoss LSM 880. FM4-64 staining was activated with 561 nm - Zeiss or 543 nm - Leica SP5 and collected with Airyscan detector - Zeiss or collection window 600-650 nm - Leica SP5. eGFP and mGFP were activated with 488 nm and collected between 525-550 nm. Metrics to calculate cell and tissue values from imaging analysis and simulations are detailed in Section 5.2.

5.1.3 Statistical Analysis.

Statistical tests were implemented using the `statannot` package in python [113]. Statistical analyses of the data (p-values and type of test) are presented in the Results section.

5.2 Image segmentation, quantification and analysis

5.2.1 Image segmentation

Images were manually cropped using MATLAB to focus on the distal portion of the SAM. Each cropped micrograph was segmented in MATLAB by isolating the color channel containing stained plasma membrane and passing it through a 2-D Gaussian filter with a standard deviation of 2.5. An h-minima transformation was then applied, with the h value optimized to minimize the variance of cell areas in each tissue region. This was followed by a watershed transformation to segment the image and remove cells on the boundary of the image. All functions mentioned were part of MATLAB's Image Processing Toolbox.

5.2.2 Feature quantification

Segmentation resulted in a mask compatible with MATLAB's "regionprops" measurements, which included calculations of cell centroids, areas, major and minor axis lengths, and orientations (see Fig 5.1, panels H, I, and J). We then manually annotated the layer identity of each cell as L1, L2, or corpus (see Fig 5.1, panel B). The *depth* of each cell was calculated by measuring the distance from the centroid of the cell to the center of the L1 cell layer, where the center of the L1 cell layer was defined to be the mean of all centroids belonging to cells in the L1 cell layer. The *aspect ratio* of a cell was calculated to be the ratio of the longest axis to the shortest axis of the cell. To calculate the *width* of the SAM, the horizontal distance between the left-most and right-most cell centroids among all L1 cell centroids was calculated for each SAM image. To calculate the *dome height* of the

SAM, the vertical distance between the lowest and highest cell centroids among all L1 cell centroids was calculated for each SAM image (see Fig 3 F in [1]).

Definition and quantification of anticlinal and periclinal divisions. Classically, anticlines and periclines are used to quantify the patterning of division plane placement relative to the nearest tissue surface or sub-epidermal cell layers [55, 56]. While developmentally relevant, such definitions present problems in the present study because these axes implicitly require placement of vertices in the corpus based on SAM shape which may require inconsistent or arbitrary heuristics that vary considerably between some of the more deformed mutant phenotypes (e.g. flat vs. enlarged meristems), ultimately leading to ambiguous definitions of anticlines and periclines for the present work. Since we are considering cells near the tunica in the central zone and for the above reasons, we define anticlinal and periclinal growth and division relative to the apical-basal axis in both simulations and experimental images. In the CZ, the conservative classifications made with our method would likely align well with classification of anticlines and periclines in the natural coordinate system as presented in [55, 56], provided that the center of the natural coordinate system was placed below the SAM. Moreover, we acknowledge that we are using this terminology as a metric for establishing phenotypic distinction between meristems, which is independent of the original developmental context behind the classic definition of anticlines and periclines.

Pairs of cells that descended from the division of a single precursor cell (i.e. sibling cells) were manually identified based on four characteristics: 1) small longitudinal section areas, 2) similar cell sizes, 3) straight flanking walls on the lateral edges of the cell pair and 4) one cell wall shared exclusively between the cell pair (see Fig 5.1, panel G). To categorize division planes into anticlinal and periclinal, the apical-basal axis was used as an absolute reference for the vertical direction. This is because near the central zone (see Fig 1.2A in Chapter 1), the curvature of the SAM is not pronounced enough to have significant disparity between the apical-basal direction and the direction normal to the surface of the SAM. With the apical-basal axis taken as vertical, we defined the

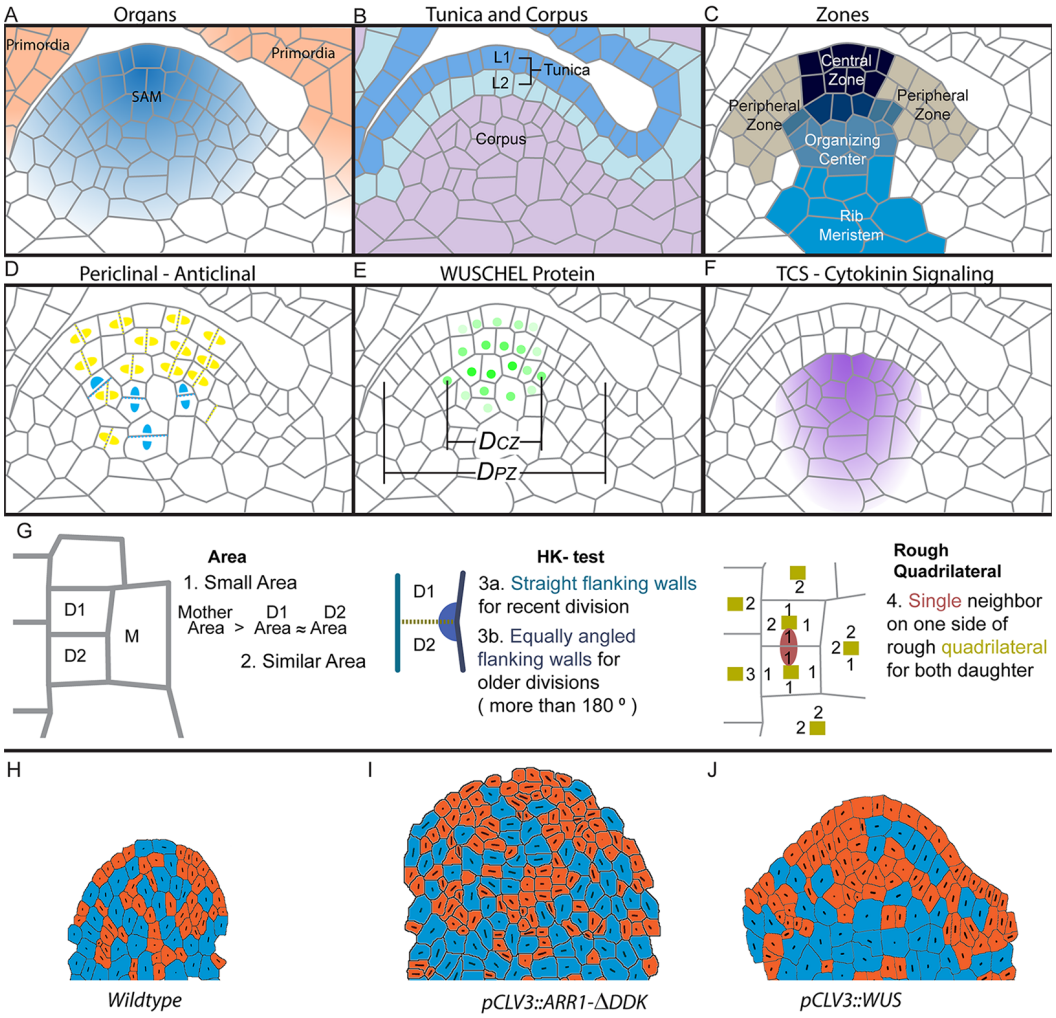

Figure 5.1: **Multiple levels of SAM organization.** (A) An annotated longitudinal section through a wildtype shoot apical meristem (SAM) and organ primordia. Clonal layers (B) and distinct functional zones (C) of the SAM. (D) Annotated cell walls from inferred daughters cells after division. Anticlinal cell divisions are shown in yellow and periclinal cell divisions are shown in cyan. (E) Overlay representing the nuclear WUS protein distribution (green). (F) Overlay representing TCS reporter of cytokinin signaling (purple). (G) Four features used to determine cell division plane orientation. Segmentation output of wildtype (H),ectopic misexpression of CK [pCLV3::LhG4; 6xOP::ARR1-ΔDDK-GR] (I), and ectopic misexpression of WUS [pCLV3::LhG4; 6xOP::eGFP-WUS-GR] (J) experimental SAMs. Line segments inside cells are provided to help visual each individual cell's aspect ratio and orientation. The length of a cell's line segment is proportional to its aspect ratio- where cell's with aspect ratio = 1 have line segments with length 0. The directional vector of each line segment represents the orientation of the longest axis of the encompassing cell. Orange denotes cells that are classified as small cells and blue denotes cells that are classified as large cells (see S1 Appendix Section 5.2.3 for details on analyses comparing large and small cell characteristics).

orientation of the newly-placed cell wall as the angle that the plane makes with the radial (i.e. horizontal) axis. More specifically, since the data are two-dimensional, new cell walls appear as lines, and the orientation is the acute angle between that line and the horizontal axis. Anticlinal divisions are those divisions with orientation $\geq 60^\circ$ and periclinal divisions are those divisions with orientation $\leq 30^\circ$. More detail on the selection of these thresholds is given in S2 Appendix. Once a pair of sibling cells was identified, the orientation of the new cell wall between them was quantified as either *anticlinal* (perpendicular to the SAM surface) or *periclinal* (perpendicular to the apical-basal axis). The number of divisions of each type was counted for a minimum of 10 experimental samples for each signaling condition.

Quantification of the direction of anisotropic cell expansion. In this study, we define the *orientation* of an individual cell as the acute angle between the radial (i.e. horizontal) axis and the longest axis of the cell. This value is given in degrees, ranging from 0° to 90° . In this way, the orientation of a cell describes its direction of anisotropic expansion relative to the SAM tissue. For example, a cell with orientation equal to 0° is expanded primarily along the radial axis of the SAM and a cell with orientation equal to 90° is expanded primarily along the apical-basal axis of the SAM. We define cells as being *elongated* if the cells have aspect ratio > 1.3. This threshold was determined because elongated cell sections in 2D have their anisotropic expansion direction better-represent the cells they are taken from in 3D (see S2 Appendix for details).

Quantification of the levels and spatial patterns of chemical signaling. The WUSCHEL (WUS) levels of individual cells were measured using fluorescence intensity from isolated color channels reporting the WUS protein in experimental SAM images for wildtype condition as shown in Fig 2.2B in Chapter 2. The WUS levels of individual cells and their corresponding cell depths were then analyzed and fit to an exponential function as in [83]. This process was repeated for SAM images containing the cytokinin (CK) distribution, which was visualized similarly (see Fig 2.2C in Chapter 2).

5.2.3 Large and small cell classification

We are using cell size as a proxy to classify cells as recently divided or about to divide. In order to get the volume of data to perform the analyses presented in this work, we relied on methods precluding the acquisition of time-series data. As such, using size as a proxy for the pre-mitotic or post-mitotic state of a cell was a methodological necessity. For analyses comparing large and small cell characteristics separately, we heuristically identify "large" cells as those with a greater than average cell area within the SAM section the cell was taken from, and "small" cells to be those cells with lower than average cell area within the SAM section the cell was taken from.

5.3 Justification of 2D experimental methods

5.3.1 Feature quantification across neighboring longitudinal section images

To determine whether feature quantification of two-dimensional, longitudinal section images was robust to the choice of median longitudinal axis, the distributions of cell aspect ratios and orientations were compared between neighboring longitudinal section images for 9 wildtype experimental SAMs. Five to ten parallel, longitudinal section images were taken from each meristem spaced apart by 1.26 microns. Cell aspect ratios and orientations were quantified for each image as described in S1 Appendix. Distributions of cell aspect ratios and orientations were compared across all longitudinal section images for each meristem using the one-way analysis of variance (ANOVA). It was determined that the distributions of cell-scale features were not significantly different between longitudinal section images.

5.3.2 Comparison of 3D vs. 2D experimental data

The use of a 2D model suggests that for a more accurate direct experimental comparison, 2D experimental data should be used. However, we would like to confirm that we may draw meaningful conclusions about an intrinsically 3D system from 2D data. Specifically, the orientation of the cell section was predicted to be highly correlated with the orientation of the cell in 3D among elongated cell sections - i.e. cell sections with large aspect ratios.

To test this prediction, 2D sections and 3D reconstructions of multiple cells were compared to one another. Two 3D Z-Stacks of wildtype inflorescent SAMs were imaged at 0.33 micron intervals producing a voxel size of 0.13 x 0.13 x 0.33 microns. These 3D images were segmented by using a deep neural network that was trained to predict, for each cell in 3D, the distance between each pixel from the boundary of the cell containing that pixel. The prediction includes the coefficients required in order to spatially fit the cell's volume in 3D to spherical harmonics, and the error in this process was minimized by training the network on a published, hand-segmented training dataset of multiple SAMs[114]. This segmentation method was performed in python from the pytorch library, and this method was detailed by Eschweiler et al. in [27].

This produced two 3D reconstructions of the SAM with 49.5 and 42.9 μm depth, respectively. Using these reconstructed 3D SAM images, we took multiple longitudinal sections of the reconstructed SAM using open-access MATLAB packages to triangulate the reconstructed SAM's cells and intersect them with the cell boundaries. Each plane passed through the apex of the SAM, and was parallel to the apical-basal axis. Five such planes - each different from one another by a rotation about the apical-basal axis - were used to generate 2D cross-sections taken from the reconstruction. Each 2D section image was then analyzed using MATLAB packages (including regionprops) as before to obtain 2D features such as orientation, aspect ratio, and area. Each cell whose section was analyzed also had its 3D properties analyzed in MATLAB's regionprops3 package to extract information such as the 3D orientation of each cell.

To confirm that the orientation direction of elongated cells in 2D well-represented the orientation direction of cells in 3D in their ability to categorize cells as anticlinal or periclinal, we calculated the angle between the orientation vectors and the apical-basal axis (i.e. the *azimuthal angle*, which is equivalent to 90° minus the orientation of a cell) both in 2D as well as 3D for each cell section (see Fig 5.2, panels A and B). In the 3D setting, we define cells that are anisotropically expanded periclinally as those with azimuthal angle $\leq 45°$ and anticlinally as those with azimuthal angle $\geq 45°$.

It was found that for aspect ratio greater than 1.3, 80% of cell sections had their 2D azimuthal angle within 15 degrees of the azimuthal angle measured from the 3D cell (see Fig 5.2, panel C). Categorizations of cell sections as anticlinally or periclinally expanded were made by placing the *section* azimuthal angle between 0° and 30° for periclinal, and 60° to 90° for anticlinal. This analysis ensures that with 80% probability, anisotropically expanded cells counted as anticlinal or periclinal by 2D section observation only give accurate representations of the cells' anisotropically expanded in 3D. That is to say, by considering cell sections with aspect ratio ≥ 1.3, we ensure:

$$\text{Prob}(\text{2D Section azimuthal angle } \leq 30° \text{ and 3D azimuthal angle } \geq 45°) \leq 20\%, \text{ and}$$

$$\text{Prob}(\text{2D Section azimuthal angle } \geq 60° \text{ and 3D azimuthal angle } \leq 45°) \leq 20\%.$$

This is equivalently stated as

$$\text{Prob}(\text{2D Section is classified as periclinal and 3D cell is classified as anticlinal}) \leq 20\%, \text{ and}$$

$$\text{Prob}(\text{2D Section is classified as anticlinal and 3D cell is classified as periclinal}) \leq 20\%.$$

Moreover, it should be noted that by observing the data (visualized in Fig 5.2, panel C), larger threshold values, e.g. aspect ratio 1.6, would improve confidence from 80% to 90%, however it would decrease the amount of experimental data points available. Therefore the threshold of aspect ratio ≥ 1.3 was chosen. Furthermore, by using the ranges of $0° - 30°$ and $0° - 45°$ to classify cells as periclinally elongated in 2D and 3D respectively, and similarly using $60° - 90°$ and $45° - 90°$ to classify cells as anticlinally expanded, 91% of 2D cell sections identified as anticlinal or periclinal

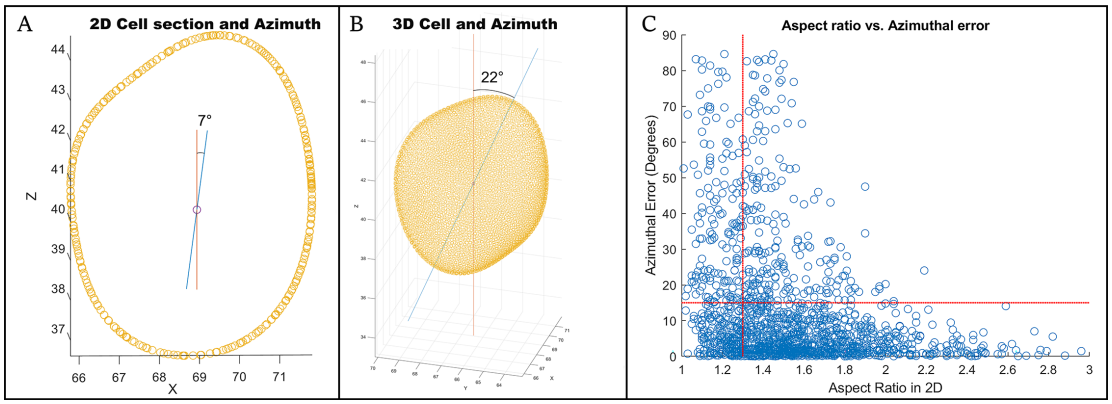

Figure 5.2: **Verification of 2D section analysis as a proxy for 3D.** (A-B) The principal direction of elongation for both 2D sections (A) and 3D cells (B) are shown in blue. The direction of apical-basal axis (taken to be the Z axis) is shown in red, and the angle between them are the azimuthal angles, which we use to classify cells as anticlinally or periclinally expanded. The 3D cell and section are taken from a z-stack image of a wildtype SAM. The units of the axes are in microns. The origin point of both the 2D and 3D axes are arbitrary. (C) The difference between the 2D and 3D cell azimuthal angles taken from 3D cells and their longitudinal section is shown on the vertical axis. The horizontal axis is the aspect ratio of the cell sections, with larger values representing more dramatically elongated cell sections. The threshold chosen for aspect ratio ≥ 1.3 is indicated by the vertical red line, and the tolerance of 15° is shown as a horizontal line. Cell sections analyzed in the 2D experimental analysis are those cells to the right of the vertical line. The aspect ratio threshold of 1.3 was chosen to include a significant portion of data, while ensuring cell sections were elongated enough to well-represent the behavior of the 3D cell.

agreed with their 3D classification. These considerations indicate that, at least among elongated longitudinal cell sections, the orientation of a cell from a 2D section provides a good estimation of the true 3D cell orientation.

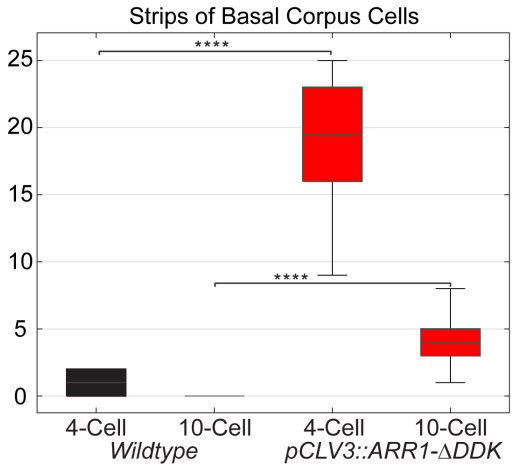

Figure 5.3: **Cytokinin signaling increases periclinal cell divisions in Basal Corpus.** Consecutive periclinal division lead to the formation of strips in wildtype (black) and ectopic misexpression of cytokinin (red). 4-cell strips are caused by three sequential periclinal divisions and 10-cell strips are caused by nine sequential periclinal division. Significance was determined by student T-test for ectopic misexpression of CK signaling compared to wildtype. Asterisks indicate significance at the following levels ****p < 0.0001.

5.4 Experimental and Image Analysis Methods Used for the Pseudo-3D Model

5.4.1 Experimental imaging ethods

Arabidopsis plants were grown for 3 weeks at 25°C under continuous light. The SAMs were excised with 2 cm of the stem. The older flowers and siliques were hand dissected. The stems were embedded into a plastic imaging box with a 1 cm layer of 1.5% agarose. The stems were positioned and further stabilized by adding additional molten agarose. The SAMs were then submerged in deionized water and further processed under a stereo microscope. Extra fine tweezers were used to remove additional flowers to expose the SAM. To stain the SAMs, the water was removed and a droplet of 3% FM-4-64 dissolved in deionized water containing 0.016% silwet-77 was placed on each SAMs for 10 minutes. After staining, plants were again submerged in deionized water and image in the upright Zeiss880. FM-4-64 was captured to produce Z-stacks by exciting with the 561 nm laser

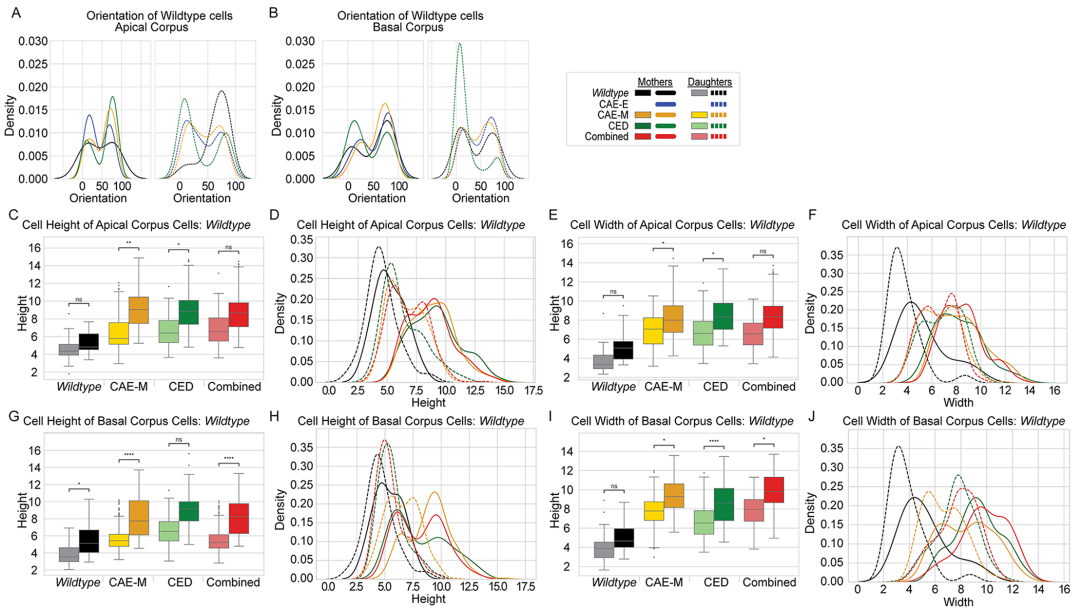

Figure 5.4: **Comparison of cell orientations, heights, and widths between experimental wildtype SAMs and wildtype simulations for all four hypothesized mechanisms.** The distributions of cell orientations for mother (solid lines) and daughter cells (dashed lines) in the (A) apical corpus and (B) basal corpus. The distributions of (C) cell heights and (D) cell widths in the apical corpus. The distribution of (E) cell heights and (F) cell widths in the basal corpus. In all Fig, experimental data (black), CAE-E (blue), CAE-M (gold), and CED(green). Significance was determined by Levene's test.

and emissions collected with BP 570 nm - 620 nm filter. Individual slices of Z-stacks were manually cropped to remove the floral primordia that were adjacent but not directly touching the meristem to improve the segmentation discussed below.

5.4.2 Image Analysis: 3D Cell Segmentation

Two 3D Z-Stacks of wildtype inflorescent SAMs were imaged at 0.33 micron intervals producing a voxel size of 0.13 x 0.13 x 0.33 microns. In order to utilize these images we perform 3D segmentation on each cell in each stack of images. Specifically we utilize a deep neural network that was trained to predict for each pixel the distance from the cell boundary and the parameters to a spherical harmonic that best fits the cell. By fitting each cell to a spherical harmonic we are able

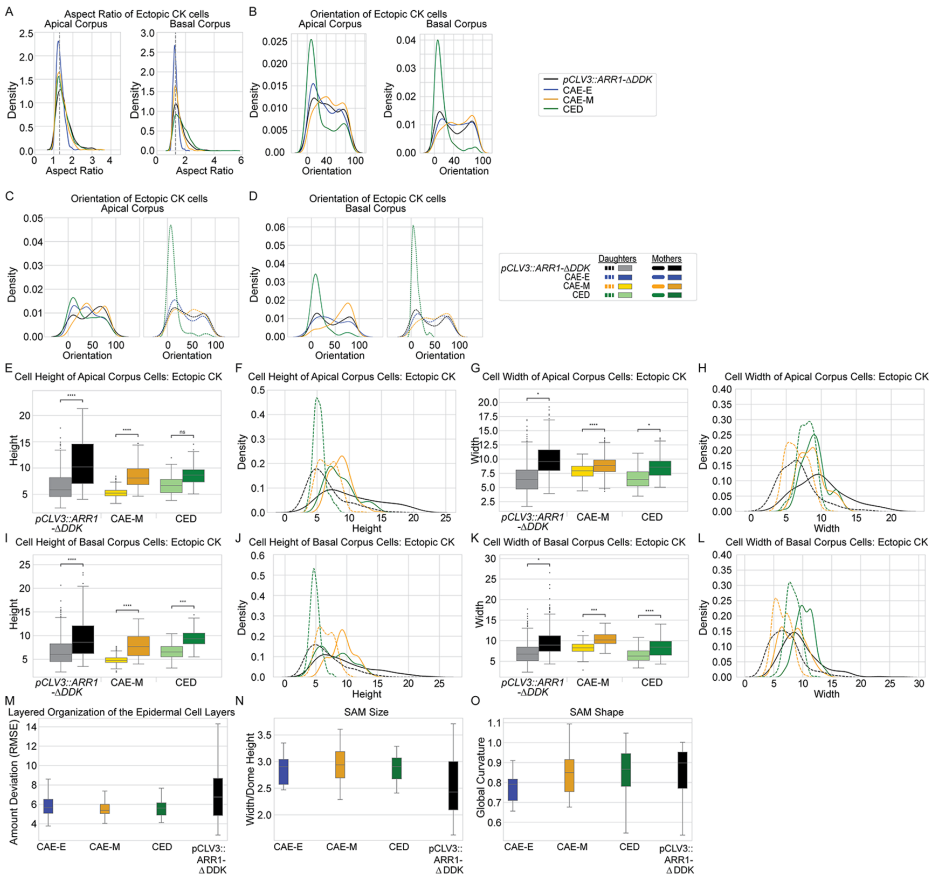

Figure 5.5: **Ectopic misexpression of CK influences the direction of anisotropic cell expansion.** The distributions of (A) cell aspect ratios and (B-D) orientations in the Apical and Basal corpus from ectopic misexpression of CK experiments [pCLV3::LhG4; 6xOP;ARR1- Δ DDK-GR] and simulations comparing three hypothesized mechanisms. (A,B) The distributions for all cells in experimental (black), CAE-E (blue), CAE-M (gold), and CED (green). The distributions of cell orientations for (C) mother cells (solid lines) and (D) daughter cells (dashed lines) were segregated based on cell size and independently graphed. The distributions of (E-F) cell heights and (G-H) cell widths in the Apical corpus for the ectopic misexpression of CK condition. The distributions of (I-J) cell heights and (K-L) cell widths in the Basal corpus for the ectopic misexpression of CK condition. (M) Amount of deviation from a single-cell layer in the epidermal L1 and L2 cell layers for experimental SAMs (black), CAE-E simulations (blue), CAE-M simulations (gold), and CED simulations (green) in the ectopic misexpression of CK condition. (N) The ratio of SAM width to dome height for experimental SAMs (black), CAE-E simulations (blue), CAE-M simulations (gold), and CED simulations (green) in the ectopic misexpression of CK condition. (O) Global curvature of the SAM surface for experimental SAMs (black), CAE-E simulations (blue), CAE-M simulations (gold), and CED simulations (green) in the ectopic misexpression of CK condition. See S2 Text for detailed description of all metrics used in this Fig

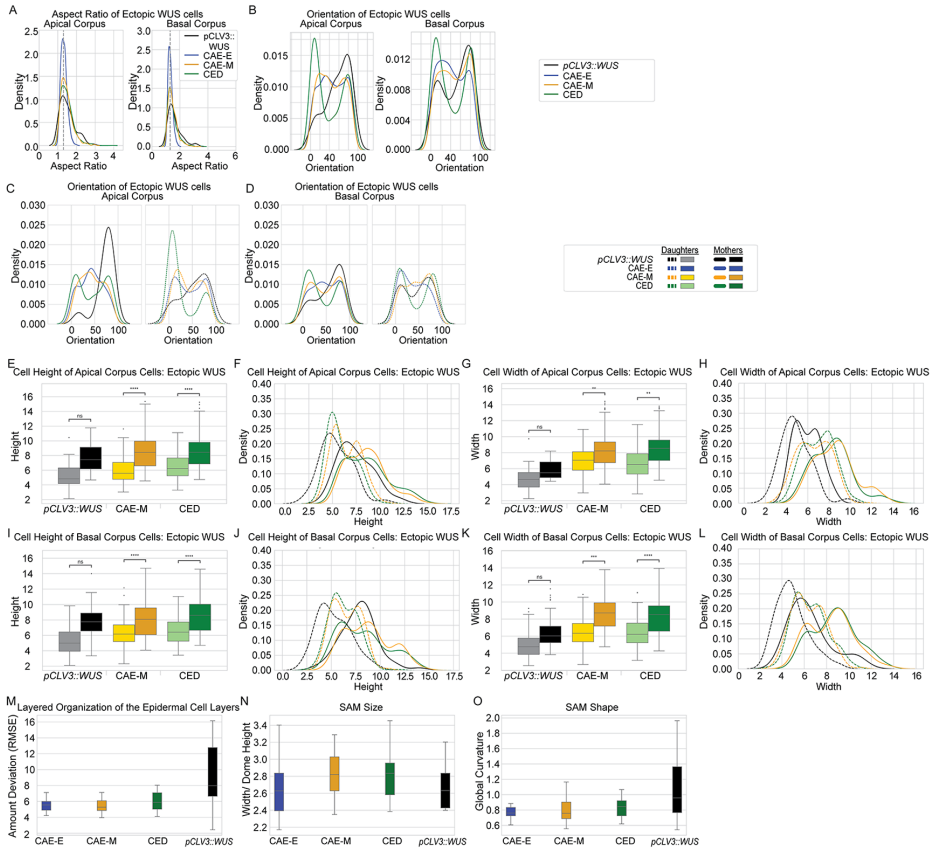

Figure 5.6: **Ectopic misexpression of WUS influences the direction of anisotropic cell expansion.** The distribution of (A) cell aspect ratios and (B-D) orientations in the apical corpus and basal corpus from ectopic misexpression of WUS in experiments [pCLV3::LhG4; 6xOP;eGFP-WUS-GR] and simulations comparing three hypothesized mechanisms. (A,B) The distribution for all cells in experimental (black), CAE-E (blue), CAE-M (gold), and CED (green). The distribution of cell orientations for (C) mother cells (solid lines) and (D) daughter cells (dashed lines) were segregated based on cell size and independently graphed. The distributions of (E-F) cell heights and (G-H) cell widths in the apical corpus of cells in ectopic misexpression of WUS condition. The distributions of (I-J) cell heights and (K-L) cell widths in the basal corpus of cells in ectopic misexpression of WUS condition. (M) Amount of deviation from a single-cell layer in the epidermal L1 and L2 cell layers for experimental SAMs (black), CAE-E simulations (blue), CAE-M simulations (gold), and CED simulations (green) in the ectopic misexpression of WUS condition. (N) The ratio of SAM width to dome height for experimental SAMs (black), CAE-E simulations (blue), CAE-M simulations (gold), and CED simulations (green) in the ectopic misexpression of WUS condition. (O) Global curvature of the SAM surface for experimental SAMs (black), CAE-E simulations (blue), CAE-M simulations (gold), and CED simulations (green) in the ectopic misexpression of WUS condition. See S2 Text for detailed description of all metrics used in this Fig

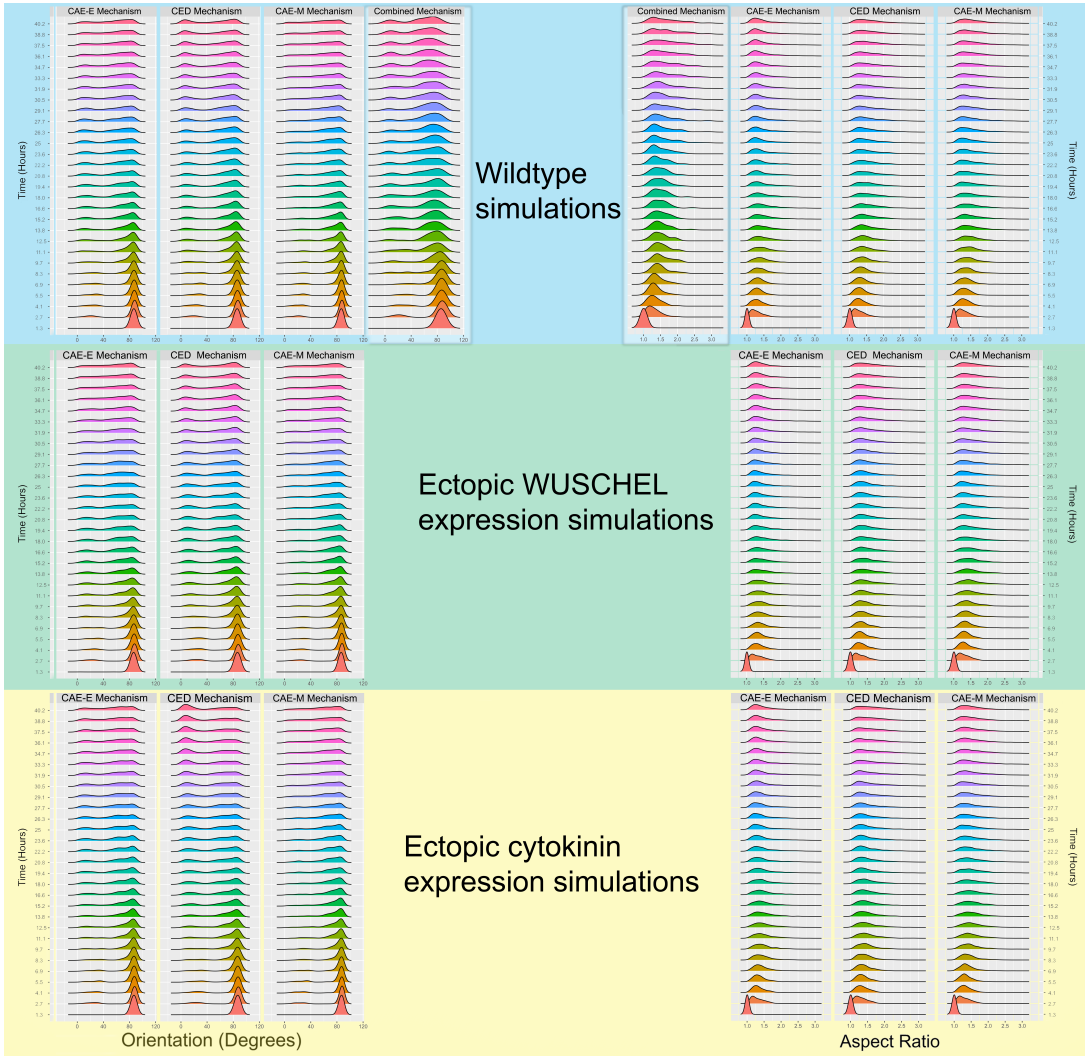

Figure 5.7: **Time evolution of simulated cell orientations and aspect ratios by condition and division plane mechanism.** The distributions of cell orientations (Left) and aspect ratios (Right) at various time points computed directly from simulations, organized by cell division plane mechanisms and perturbation condition. The distributions of cell orientations and aspect ratios were obtained for the combined mechanism only in the wildtype simulations.

to filter out low quality segmentations by rejecting any segmentations that result in irregular cell shapes. This network was trained on a published, hand-segmented training dataset of multiple SAMs [114]. The segmentation method was performed in Python and the neural network was implemented using the Pytorch library, and this method was detailed by Eschweiler et al. in [27]. From there we

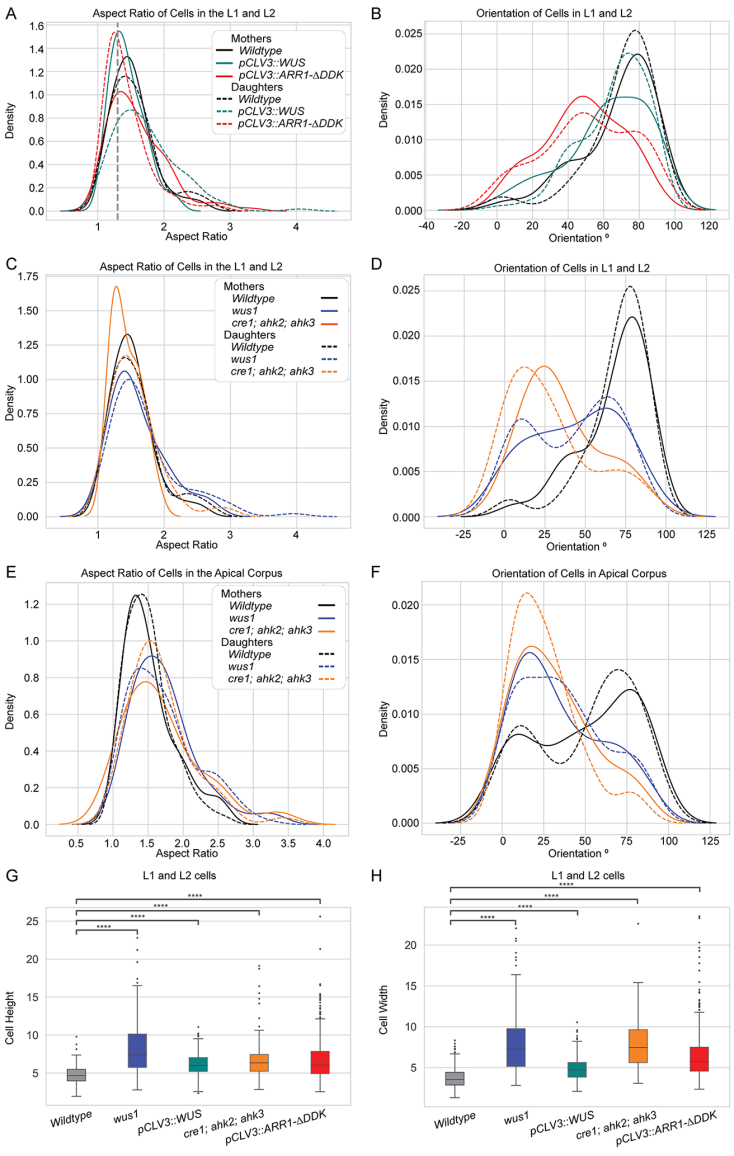

Figure 5.8: **WUS and CK misexpression and loss of function mutants influence the direction of anisotropic expansion of cells.** (A) Aspect ratio and (B) orientation of L1 and L2 cells in from wildtype, ectopic misexpression of WUS [pCLV3::LhG4; 6xOP::eGFP-WUS-GR], and ectopic misexpression of CK [pCLV3::LhG4; 6xOP::ARR1-ΔDDK-GR] experimental SAMs. (C-F) Cell layer specific aspect ratio and orientation of cells from wildtype, *wus1* mutants [*wus1-1*], and cytokinin triple receptor mutants[*cre1;ahk2;ahk3*]. Cell height (G) and width (H) of L1 and L2 cell layers for each experimental condition. Significance was determined by t-test for each experimental condition compared to wildtype. Asterisks indicate significance at the following levels:****$p < 0.0001$.

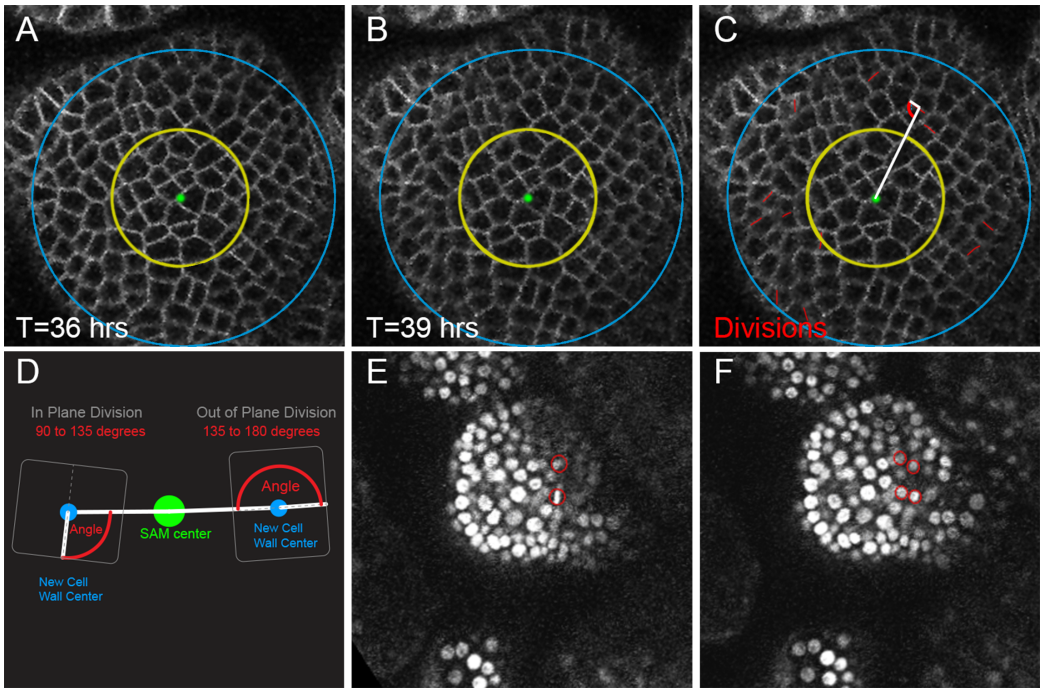

Figure 5.9: **Quantification of out-of-plane divisions from time-lapse images.** (A-B) Manually identified cell division events in the L layer of the SAM labeled with plasma membrane-localized YFP between time intervals 36 and 39 hours of time lapse series. The yellow ring indicates the central zone; the blue ring is the peripheral zone. (C) Division planes observed between 36 and 39 hours are marked in red. Lines connecting the SAM apex and the midpoint of the new cell walls are connected and the angle between the new wall and the line are measured. (D) Divisions are categorized as in-plane or out-of-plane based on the measured angle. (E-F) In the deeper layers of the SAM, similar measurements were taken on the nuclear labeled images of a SAM taken every 1.5 hours hours. Division planes in these images were inferred from cell nucleus centroid positions (E) before versus (F) after divisions.

then reconstructed the segmented SAMs by taking the segmentation and computing a convex hull around each cell in 3D.

This resulted in two 3D reconstructions of SAMs with 49.5 and 42.9 μm depth, respectively. Using these reconstructed 3D SAM images, we took multiple longitudinal sections of the reconstructed SAM using open-access MATLAB packages to intersect them with the cell boundaries. Each plane passed through the apex of the SAM, and was parallel to the apical-basal axis. Five such planes - each different from one another by a rotation about the apical-basal axis - were used to generate 2D cross-sections taken from the reconstruction. Each 2D cross-section was then analyzed using MATLAB packages (including regionprops) to extract 2D features such as orientation, aspect ratio, and area. Then from each cross-section we also had each cell's 3D properties analyzed using MATLAB's regionprops3 package to extract additional 3D features such as the 3D orientation of each cell.

Chapter 6

Discussion and Future Work

In this dissertation, a pseudo 3D (P3D) cell-based SCE model of a longitudinal section of the SAM in *Arabidopsis thaliana* is developed and calibrated using 3D experimental imaging data. The P3D model is novel by taking into account anisotropic expansion of cells orthogonal to the longitudinal cross-section plane. 2D and P3D models were applied to study the impacts of epidermal tension within the biologically relevant range resulting from the connection of the SAM to the surrounding tissue, on the maintenance of SAM tissue shape and structure. In particular, the apical corpus has a layer structure, which is critical to properly place organs and produce different cell types during development. Maintenance of such layer structure requires that cell division follows a specific rule. The cell division plane placement mechanism introduced in [1] was shown to preserve this important morphology under epidermal tension in this study.

Model simulations demonstrated that cell shapes in the tunica were dependent on the magnitude of the SAM boundary tension in the P3D model, while other effects, such as increased cell-cell crowding, dominated tunica cell shapes in the 2D model. Nevertheless, cell and tissue shapes in the corpus were similar in both 2D and P3D model simulations. Upon analysis of division patterning and cell neighborhood structure, it is shown that this may be due to the local stress based division plane orientation mechanism. This was further supported by the observations that the

model simulations with free boundary conditions produced tissue and corpus cell shapes very similar to those obtained in simulations with boundary forces that give rise to experimentally observed curvature.

Moreover, comparison between the 2D and P3D models simulations revealed regulatory functionality of the mechanically-driven division plane mechanism in tissue patterning. Boundary tension was shown to play an essential role in maintaining the layered structure of the SAM tunica, though its importance is overshadowed by cell-cell crowding effects if 3D expansion is not considered in the model. Cell-cell crowding and buckling observed in 2D simulations suggest that coordinated anisotropic cell expansion along a plane can lead to tissue morphological changes similar to intestinal crypt formation [115], or other epithelial invagination processes [116, 117, 118].

It was also observed that even substantially increased boundary tension along the tunica did not impact corpus structure or distribution of cell shapes in either the 2D or P3D models. This suggests that the cell division patterning in the apical corpus has some robustness to variations in the magnitude of tension applied along the tunica. This robustness can facilitate plant growth, as it implies that the cellular structure of the rib meristem could be robust to mechanical perturbations, whether they are extrinsic (e.g. tissue damage) or intrinsic (e.g. expansin-induced changes to tunica mechanical properties).

The results also suggest that mutant types of SAMs which exhibit deviations in percentages of periclinal divisions and distorted tissue shapes (e.g. pCLV3::LhG4; 6xOP::ARR1-ΔDDK-GR cytokinin receptor mutants [1]) may have their division patterning disrupted by a perturbation of the ability in cells to respond to mechanical signals. This may be caused by cell-cell crowding from uncontrolled or uncoordinated cell growth and division within the corpus. It may also be the case that WUS and CK have a critical role for cells in sensing their mechanical surroundings, and mutant types are less sensitive to their mechanical environment.

Finally, we hypothesize, based on obtained results, that ectopic activation of WUS and CK signaling can modify the cell identity, so that the division planes are no longer determined

mechanically. Therefore, there are several different directions of future study suggested by the current work. If the mechanical signals generated by boundary forces applied to the tunica do not impact the apical corpus structure and organization, and if the tunica and apical corpus are tightly adhered, it would be important to study how the mechanical signals from the tunica are kept separate from the corpus. It will be also worthwhile to investigate how WUS and CK affect the ability of cells in the corpus to receive mechanical signals. It is possible that there is a mechanical signaling pathway that WUS and CK regulate nontrivially, or there are signals independent of the ability of cells to respond to their local mechanical stresses. Identifying the downstream components of cell growth and division regulated by WUS and CK, and analysis of the cytoskeletal response to perturbation of these regulators may provide new insight about the maintenance of tissue structure.

In the future, we plan to build on the recently obtained results on the maintenance of the WUS protein gradient by *CLAVATA3* signaling [19] and the WUS concentration dependent regulation of *CLAVATA3* transcription [20] to implement a dynamic signaling variant of the present model, wherein the WUS and CK gradients influence the mechanical model, and the mechanical model provides dynamically evolving domain for signaling submodel.

Future experimentation including analysis of deep-layer division patterning under the conditions of mechanically perturbed SAM tunica tension, can show the independence between the corpus and tunica of the SAM predicted by the model simulations described in this dissertation. The spatial localization of this patterning in a functional zone would motivate the investigation of the functionality of this regulation. It may also suggest a self-maintenance programming of the SAM in order to maintain a consistent spatial domain and further to facilitate the characteristic phyllotactic patterning in the plant.

References

[1] Mikahl Banwarth-Kuhn, Kevin Rodriguez, Christian Michael, Calvin-Khang Ta, Alexander Plong, Eric Bourgain-Chang, Ali Nematbakhsh, Weitao Chen, Amit Roy-Chowdhury, G. Venugopala Reddy, and Mark Alber. Combined computational modeling and experimental analysis integrating chemical and mechanical signals suggests possible mechanism of shoot meristem maintenance. *PLOS Computational Biology*, 18(6):e1010199, jun 2022. ISSN 1553-7358. doi: 10.1371/journal.pcbi.1010199. URL `https://dx.plos.org/10.1371/journal.pcbi.1010199`.

[2] Mikahl Banwarth-Kuhn, Ali Nematbakhsh, Kevin W. Rodriguez, Stephen Snipes, Carolyn G. Rasmussen, G. Venugopala Reddy, and Mark Alber. Cell-Based Model of the Generation and Maintenance of the Shape and Structure of the Multilayered Shoot Apical Meristem of Arabidopsis thaliana. *Bulletin of Mathematical Biology*, 81(8):3245–3281, 2019. ISSN 15229602. doi: 10.1007/s11538-018-00547-z.

[3] Marion Louveaux, Jean-Daniel Julien, Vincent Mirabet, Arezki Boudaoud, and Olivier Hamant. Cell division plane orientation based on tensile stress in arabidopsis thaliana. *Proc. Natl. Acad. Sci. U. S. A.*, 113(30):E4294–303, July 2016.

[4] Bruce Alberts. *Molecular Biology of the Cell*. Garland Science, August 2017.

[5] Jocelyn K C Rose. *The Plant Cell Wall*. CRC Press, 2003.

[6] Marcia Maria de Oliveira Buanafina and Daniel J Cosgrove. Cell walls: Structure and biogenesis. In *Sugarcane: Physiology, Biochemistry, and Functional Biology*, pages 307–329. John Wiley & Sons Ltd, Chichester, UK, December 2013.

[7] N C Carpita and D M Gibeaut. Structural models of primary cell walls in flowering plants: consistency of molecular structure with the physical properties of the walls during growth. *Plant J.*, 3(1):1–30, January 1993.

[8] Daniel J Cosgrove. Growth of the plant cell wall. *Nat. Rev. Mol. Cell Biol.*, 6(11):850–861, November 2005.

[9] D J Cosgrove. Wall structure and wall loosening. a look backwards and forwards. *Plant Physiol.*, 125(1):131–134, January 2001.

[10] Sébastien Besson and Jacques Dumais. Universal rule for the symmetric division of plant cells. *Proc. Natl. Acad. Sci. U. S. A.*, 108(15):6294–6299, April 2011.

[11] Bruce E Shapiro, Cory Tobin, Eric Mjolsness, and Elliot M Meyerowitz. Analysis of cell division patterns in the arabidopsis shoot apical meristem. *Proc. Natl. Acad. Sci. U. S. A.*, 112(15):4815–4820, April 2015.

[12] Olivier Hamant, Marcus G Heisler, Henrik Jönsson, Pawel Krupinski, Magalie Uyttewaal, Plamen Bokov, Francis Corson, Patrik Sahlin, Arezki Boudaoud, Elliot M Meyerowitz, Yves Couder, and Jan Traas. Developmental patterning by mechanical signals in arabidopsis. *Science*, 322(5908):1650–1655, December 2008.

[13] Sijia Liu, François Jobert, Zahra Rahneshan, Siamsa M Doyle, and Stéphanie Robert. Solving the puzzle of shape regulation in plant epidermal pavement cells. *Annual Review of Plant Biology*, 72:525–550, 2021.

[14] Silvia Lechthaler, Natasa Kiorapostolou, Andrea Pitacco, Tommaso Anfodillo, and Giai Petit. The total path length hydraulic resistance according to known anatomical patterns: What is

the shape of the root-to-leaf tension gradient along the plant longitudinal axis? *Journal of Theoretical Biology*, 502:110369, 2020.

[15] Dorota Kwiatkowska and Jacques Dumais. Growth and morphogenesis at the vegetative shoot apex of anagallis arvensis l. *Journal of Experimental Botany*, 54(387):1585–1595, 2003.

[16] ERRERA and L. Uber zellformen und seifenblasen. *Bot. Cent.bl.*, 34:395–398, 1888.

[17] L G Smith. Plant cell division: building walls in the right places. *Nat. Rev. Mol. Cell Biol.*, 2 (1):33–39, January 2001.

[18] Magalie Uyttewaal, Agata Burian, Karen Alim, Benoît Landrein, Dorota Borowska-Wykręt, Annick Dedieu, Alexis Peaucelle, Michał Ludynia, Jan Traas, Arezki Boudaoud, Dorota Kwiatkowska, and Olivier Hamant. Mechanical stress acts via katanin to amplify differences in growth rate between adjacent cells in arabidopsis. *Cell*, 149(2):439–451, April 2012.

[19] Alexander Plong, Kevin Rodriguez, Mark Alber, Weitao Chen, and G Venugopala Reddy. Clavata3 mediated simultaneous control of transcriptional and post-translational processes provides robustness to the wuschel gradient. *Nature communications*, 12(1):1–13, 2021.

[20] Kevin Rodriguez, Albert Do, Betul Senay-Aras, Mariano Perales, Mark Alber, Weitao Chen, and G Venugopala Reddy. Concentration-dependent transcriptional switching through a collective action of cis-elements. *Science Advances*, 8(31):eabo6157, 2022.

[21] Matthew D.B. Jackson, Salva Duran-Nebreda, Daniel Kierzkowski, Soeren Strauss, Hao Xu, Benoit Landrein, Olivier Hamant, Richard S. Smith, Iain G. Johnston, and George W. Bassel. Global Topological Order Emerges through Local Mechanical Control of Cell Divisions in the Arabidopsis Shoot Apical Meristem. *Cell Systems*, 8(1):53–65.e3, jan 2019. ISSN 24054712. doi: 10.1016/j.cels.2018.12.009. URL `https://doi.org/10.1016/j.cels.2018.12.009https://linkinghub.elsevier.com/retrieve/pii/S2405471218305088`.

[22] Patrik Sahlin and Henrik Jönsson. A modeling study on how cell division affects properties of epithelial tissues under isotropic growth. *PloS one*, 5(7):e11750, 2010.

[23] Alexander G Fletcher, Miriam Osterfield, Ruth E Baker, and Stanislav Y Shvartsman. Vertex models of epithelial morphogenesis. *Biophysical journal*, 106(11):2291–2304, 2014.

[24] Yuchen Long, Ibrahim Cheddadi, Gabriella Mosca, Vincent Mirabet, Mathilde Dumond, Annamaria Kiss, Jan Traas, Christophe Godin, and Arezki Boudaoud. Cellular heterogeneity in pressure and growth emerges from tissue topology and geometry. *Current Biology*, 30(8): 1504–1516, 2020.

[25] George W Bassel, Petra Stamm, Gabriella Mosca, Pierre Barbier de Reuille, Daniel J Gibbs, Robin Winter, Ales Janka, Michael J Holdsworth, and Richard S Smith. Mechanical constraints imposed by 3d cellular geometry and arrangement modulate growth patterns in the arabidopsis embryo. *Proceedings of the National Academy of Sciences*, 111(23):8685–8690, 2014.

[26] Gabriella Mosca, Aleksandra Sapala, Soeren Strauss, Anne-Lise Routier-Kierzkowska, and Richard S Smith. On the micro-indentation of plant cells in a tissue context. *Physical Biology*, 14(1):015003, 2017.

[27] Dennis Eschweiler, Malte Rethwisch, Simon Koppers, and Johannes Stegmaier. Spherical harmonics for shape-constrained 3d cell segmentation. In *2021 IEEE 18th International Symposium on Biomedical Imaging (ISBI)*, pages 792–796, 2021. doi: 10.1109/ISBI48211.2021.9433983.

[28] Léna Beauzamy, Marion Louveaux, Olivier Hamant, and Arezki Boudaoud. Mechanically, the shoot apical meristem of arabidopsis behaves like a shell inflated by a pressure of about 1 mpa. *Frontiers in plant science*, 6:1038, 2015.

[29] J Sebastian Giudice, Wei Zeng, Taotao Wu, Ahmed Alshareef, Daniel F Shedd, and Matthew B Panzer. An analytical review of the numerical methods used for finite element modeling of traumatic brain injury. *Annals of biomedical engineering*, 47(9):1855–1872, 2019.

[30] Guoqiang Luo, Yuxuan Zhu, Ruizhi Zhang, Peng Cao, Qiwen Liu, Jian Zhang, Yi Sun, Huan Yuan, Wei Guo, Qiang Shen, et al. A review on mechanical models for cellular media: Investigation on material characterization and numerical simulation. *Polymers*, 13(19):3283, 2021.

[31] Benjamin Owen, Nicholas Bojdo, Andrey Jivkov, Bernard Keavney, and Alistair Revell. Structural modelling of the cardiovascular system. *Biomechanics and modeling in mechanobiology*, 17(5):1217–1242, 2018.

[32] Mohammad M Faghih and M Keith Sharp. Modeling and prediction of flow-induced hemolysis: a review. *Biomechanics and modeling in mechanobiology*, 18(4):845–881, 2019.

[33] Gordon F Newell and Elliott W Montroll. On the theory of the ising model of ferromagnetism. *Reviews of Modern Physics*, 25(2):353, 1953.

[34] Renfrey Burnard Potts. *Mathematical investigation of some cooperative phenomena*. PhD thesis, University of Oxford, 1950.

[35] François Graner and James A Glazier. Simulation of biological cell sorting using a two-dimensional extended potts model. *Physical Review Letters*, 69(13):2013, 1992.

[36] Mark Alber, Nan Chen, Tilmann Glimm, and Pavel M Lushnikov. Multiscale dynamics of biological cells with chemotactic interactions: from a discrete stochastic model to a continuous description. *Physical Review E*, 73(5):051901, 2006.

[37] James A Glazier and François Graner. Simulation of the differential adhesion driven rearrangement of biological cells. *Physical Review E*, 47(3):2128, 1993.

[38] Evelyn F Keller and Lee A Segel. Model for chemotaxis. *Journal of theoretical biology*, 30(2): 225–234, 1971.

[39] Mark Alber, Nan Chen, Pavel M Lushnikov, and Stuart A Newman. Continuous macroscopic limit of a discrete stochastic model for interaction of living cells. *Physical review letters*, 99 (16):168102, 2007.

[40] Jesús A Izaguirre, Rajiv Chaturvedi, Chengbang Huang, Trevor Cickovski, J Coffland, G Thomas, Gabor Forgacs, M Alber, G Hentschel, Stuart A Newman, and J A Glazier. Compucell, a multi-model framework for simulation of morphogenesis. *Bioinformatics*, 20(7): 1129–1137, 2004.

[41] Rajiv Chaturvedi, Chengbang Huang, Bogdan Kazmierczak, T Schneider, Jesus A Izaguirre, Tilmann Glimm, H George E Hentschel, JA Glazier, SA Newman, and MS Alber. On multiscale approaches to three-dimensional modelling of morphogenesis. *Journal of the Royal Society interface*, 2(3):237–253, 2005.

[42] Maciej H Swat, Gilberto L Thomas, Julio M Belmonte, Abbas Shirinifard, Dimitrij Hmeljak, and James A Glazier. Multi-scale modeling of tissues using compucell3d. In *Methods in cell biology*, volume 110, pages 325–366. Elsevier, 2012.

[43] Calvin Lam, Sajeev Saluja, George Courcoubetis, Dottie Yu, Christian Chung, Josquin Courte, and Leonardo Morsut. Parameterized computational framework for the description and design of genetic circuits of morphogenesis based on contact-dependent signaling and changes in cell–cell adhesion. *ACS Synthetic Biology*, 11(4):1417–1439, 2022.

[44] J Todd Blankenship, Stephanie T Backovic, Justina SP Sanny, Ori Weitz, and Jennifer A Zallen. Multicellular rosette formation links planar cell polarity to tissue morphogenesis. *Developmental cell*, 11(4):459–470, 2006.

[45] Alexander Nestor-Bergmann, Guy B Blanchard, Nathan Hervieux, Alexander G Fletcher, Jocelyn Étienne, and Bénédicte Sanson. Adhesion-regulated junction slippage controls cell intercalation dynamics in an apposed-cortex adhesion model. *PLoS computational biology*, 18 (1):e1009812, 2022.

[46] Roeland MH Merks, Michael Guravage, Dirk Inzé, and Gerrit TS Beemster. Virtualleaf: an open-source framework for cell-based modeling of plant tissue growth and development. *Plant physiology*, 155(2):656–666, 2011.

[47] Roeland MH Merks and Michael A Guravage. Building simulation models of developing plant organs using virtualleaf. In *Plant Organogenesis*, pages 333–352. Springer, 2013.

[48] Henri B Wolff, Lance A Davidson, and Roeland MH Merks. Adapting a plant tissue model to animal development: introducing cell sliding into virtualleaf. *Bulletin of mathematical biology*, 81(8):3322–3341, 2019.

[49] Nan Chen, James A Glazier, Jesús A Izaguirre, and Mark S Alber. A parallel implementation of the cellular potts model for simulation of cell-based morphogenesis. *Computer physics communications*, 176(11-12):670–681, 2007.

[50] Ali Nematbakhsh, Wenzhao Sun, Pavel A. Brodskiy, Aboutaleb Amiri, Cody Narciso, Zhiliang Xu, Jeremiah J. Zartman, and Mark Alber. Multi-scale computational study of the mechanical regulation of cell mitotic rounding in epithelia. *PLoS Computational Biology*, 13(5):e1005533, may 2017. ISSN 15537358. doi: 10.1371/journal.pcbi.1005533.

[51] Raphaël Conradin, Christophe Coreixas, Jonas Latt, and Bastien Chopard. Palacell2d: A framework for detailed tissue morphogenesis. *Journal of Computational Science*, 53:101353, 2021.

[52] TA Steeves and I Sussex. *Patterns in Plant Development: Shoot Apical Meristem Mutants of Arabidopsis thaliana*. Cambridge Univ Press, New York, 1989.

[53] Mingtang Xie, Moses Tataw, and G Venugopala Reddy. Towards a functional understanding of cell growth dynamics in shoot meristem stem-cell niche. *Semin. Cell Dev. Biol.*, 20(9): 1126–1133, December 2009.

[54] Robert F Lyndon. *The shoot apical meristem: its growth and development*. Cambridge University Press, 1998.

[55] Dorota Kwiatkowska. Structural integration at the shoot apical meristem: models, measurements, and experiments. *American journal of botany*, 91(9):1277–1293, 2004.

[56] Z Hejnowicz and J Karczewski. Modeling of meristematic growth of root apices in a natural coordinate system. *American Journal of Botany*, 80(3):309–315, 1993.

[57] Jekaterina Truskina and Teva Vernoux. The growth of a stable stationary structure: coordinating cell behavior and patterning at the shoot apical meristem. *Curr. Opin. Plant Biol.*, 41: 83–88, February 2018.

[58] M K Barton. Twenty years on: The inner workings of the shoot apical meristem, a developmental dynamo. *Dev. Biol.*, 341(1):95–113, May 2010.

[59] G Venugopala Reddy, Marcus G Heisler, David W Ehrhardt, and Elliot M Meyerowitz. Real-time lineage analysis reveals oriented cell divisions associated with morphogenesis at the shoot apex of arabidopsis thaliana. *Development*, 131(17):4225–4237, September 2004.

[60] G Venugopala Reddy and Elliot M Meyerowitz. Stem-cell homeostasis and growth dynamics can be uncoupled in the arabidopsis shoot apex. *Science*, 310(5748):663–667, October 2005.

[61] Ram Kishor Yadav, Montreh Tavakkoli, and G Venugopala Reddy. WUSCHEL mediates stem cell homeostasis by regulating stem cell number and patterns of cell division and differentiation of stem cell progenitors. *Development*, 137(21):3581–3589, November 2010.

[62] Didier Reinhardt, Eva-Rachele Pesce, Pia Stieger, Therese Mandel, Kurt Baltensperger, Malcolm Bennett, Jan Traas, Jirí Friml, and Cris Kuhlemeier. Regulation of phyllotaxis by polar auxin transport. *Nature*, 426(6964):255–260, November 2003.

[63] Henrik Jönsson, Marcus G Heisler, Bruce E Shapiro, Elliot M Meyerowitz, and Eric Mjolsness. An auxin-driven polarized transport model for phyllotaxis. *Proc. Natl. Acad. Sci. U. S. A.*, 103(5):1633–1638, January 2006.

[64] Richard S Smith, Soazig Guyomarc'h, Therese Mandel, Didier Reinhardt, Cris Kuhlemeier, and Przemyslaw Prusinkiewicz. A plausible model of phyllotaxis. *Proc. Natl. Acad. Sci. U. S. A.*, 103(5):1301–1306, January 2006.

[65] Pierre Barbier de Reuille, Isabelle Bohn-Courseau, Karin Ljung, Halima Morin, Nicola Carraro, Christophe Godin, and Jan Traas. Computer simulations reveal properties of the cell-cell signaling network at the shoot apex in arabidopsis. *Proc. Natl. Acad. Sci. U. S. A.*, 103(5): 1627–1632, January 2006.

[66] Ram Kishor Yadav, Mariano Perales, Jérémy Gruel, Thomas Girke, Henrik Jönsson, and G Venugopala Reddy. WUSCHEL protein movement mediates stem cell homeostasis in the arabidopsis shoot apex. *Genes Dev.*, 25(19):2025–2030, October 2011.

[67] Sean P Gordon, Vijay S Chickarmane, Carolyn Ohno, and Elliot M Meyerowitz. Multiple feedback loops through cytokinin signaling control stem cell number within the arabidopsis shoot meristem. *Proc. Natl. Acad. Sci. U. S. A.*, 106(38):16529–16534, September 2009.

[68] Stephen A Snipes, Kevin Rodriguez, Aaron E DeVries, Kaori N Miyawaki, Mariano Perales, Mingtang Xie, and G Venugopala Reddy. Cytokinin stabilizes WUSCHEL by acting on the protein domains required for nuclear enrichment and transcription. *PLoS Genet.*, 14(4):e1007351, April 2018.

[69] T Laux, K F Mayer, J Berger, and G Jürgens. The WUSCHEL gene is required for shoot and floral meristem integrity in arabidopsis. *Development*, 122(1):87–96, January 1996.

[70] Jenia Schlegel, Gregoire Denay, Rene Wink, Karine Gustavo Pinto, Yvonne Stahl, Julia Schmid, Patrick Blümke, and Rüdiger GW Simon. Control of arabidopsis shoot stem cell homeostasis by two antagonistic cle peptide signalling pathways. *Elife*, 10:e70934, 2021.

[71] Evelyne Zürcher, Deborah Tavor-Deslex, Dmytro Lituiev, Katalin Enkerli, Paul T Tarr, and Bruno Müller. A robust and sensitive synthetic sensor to monitor the transcriptional output of the cytokinin signaling network in planta. *Plant Physiol.*, 161(3):1066–1075, March 2013.

[72] Vijay S Chickarmane, Sean P Gordon, Paul T Tarr, Marcus G Heisler, and Elliot M Meyerowitz. Cytokinin signaling as a positional cue for patterning the apical-basal axis of the growing arabidopsis shoot meristem. *Proc. Natl. Acad. Sci. U. S. A.*, 109(10):4002–4007, March 2012.

[73] G Venugopala Reddy. Live-imaging stem-cell homeostasis in the arabidopsis shoot apex. *Current opinion in plant biology*, 11(1):88–93, 2008.

[74] Priyanka Jha, Sergio J Ochatt, and Vijay Kumar. Wuschel: a master regulator in plant growth signaling. *Plant cell reports*, 39(4):431–444, 2020.

[75] Pascale Milani, Maryam Gholamirad, Jan Traas, Alain Arnéodo, Arezki Boudaoud, Françoise Argoul, and Olivier Hamant. In vivo analysis of local wall stiffness at the shoot apical meristem in arabidopsis using atomic force microscopy. *The Plant Journal*, 67(6):1116–1123, 2011.

[76] Stefano Bencivenga, Antonio Serrano-Mislata, Max Bush, Samantha Fox, and Robert Sablowski. Control of oriented tissue growth through repression of organ boundary genes promotes stem morphogenesis. *Developmental cell*, 39(2):198–208, 2016.

[77] Andrew C Willoughby and Zachary L Nimchuk. Wox going on: Cle peptides in plant development. *Current opinion in plant biology*, 63:102056, 2021.

[78] Geraldine Brunoud, Carlos S Galvan-Ampudia, and Teva Vernoux. Methods to visualize auxin and cytokinin signaling activity in the shoot apical meristem. In *Plant Stem Cells*, pages 79–89. Springer, 2020.

[79] Christophe Godin, Christophe Golé, and Stéphane Douady. Phyllotaxis as geometric canalization during plant development. *Development*, 147(19):dev165878, 2020.

[80] Sajid Hussain, Satyabrata Nanda, Junhua Zhang, Muhammad Ishaq Asif Rehmani, Muhammad Suleman, Gaojie Li, and Hongwei Hou. Auxin and cytokinin interplay during leaf morphogenesis and phyllotaxy. *Plants*, 10(8):1732, 2021.

[81] Yun Zhou, An Yan, Han Han, Ting Li, Yuan Geng, Xing Liu, and Elliot M Meyerowitz. Hairy meristem with wuschel confines clavata3 expression to the outer apical meristem layers. *Science*, 361(6401):502–506, 2018.

[82] Teva Vernoux, Fabrice Besnard, and Jan Traas. Auxin at the shoot apical meristem. *Cold Spring Harbor perspectives in biology*, 2(4):a001487, 2010.

[83] Mikahl Banwarth-Kuhn, Ali Nematbakhsh, Kevin W. Rodriguez, Stephen Snipes, Carolyn G. Rasmussen, G. Venugopala Reddy, and Mark Alber. Cell-based model of the generation and maintenance of the shape and structure of the multilayered shoot apical meristem of arabidopsis thaliana. *Bulletin of Mathematical Biology*, 81(8):3245–3281, 2019. doi: 10.1007/s11538-018-00547-z. URL `https://doi.org/10.1007/s11538-018-00547-z`.

[84] Ali Nematbakhsh, Megan Levis, Nilay Kumar, Weitao Chen, Jeremiah J Zartman, and Mark Alber. Epithelial organ shape is generated by patterned actomyosin contractility and maintained by the extracellular matrix. *PLoS Comput. Biol.*, 16(8):e1008105, August 2020.

[85] Ali Nematbakhsh, Wenzhao Sun, Pavel A Brodskiy, Aboutaleb Amiri, Cody Narciso, Zhiliang Xu, Jeremiah J Zartman, and Mark Alber. Multi-scale computational study of the mechanical

regulation of cell mitotic rounding in epithelia. *PLoS Comput. Biol.*, 13(5):e1005533, May 2017.

[86] Aboutaleb Amiri, Cameron Harvey, Amy Buchmann, Scott Christley, Joshua D Shrout, Igor S Aranson, and Mark Alber. Reversals and collisions optimize protein exchange in bacterial swarms. *Phys Rev E*, 95(3-1):032408, March 2017.

[87] Ziheng Wu, Zhiliang Xu, Oleg Kim, and Mark Alber. Three-dimensional multi-scale model of deformable platelets adhesion to vessel wall in blood flow. *Philos. Trans. A Math. Phys. Eng. Sci.*, 372(2021), August 2014.

[88] Christopher R Sweet, Santanu Chatterjee, Zhiliang Xu, Katharine Bisordi, Elliot D Rosen, and Mark Alber. Modelling platelet-blood flow interaction using the subcellular element langevin method. *J. R. Soc. Interface*, 8(65):1760–1771, December 2011.

[89] Cameron W Harvey, Faruck Morcos, Christopher R Sweet, Dale Kaiser, Santanu Chatterjee, Xiaomin Liu, Danny Z Chen, and Mark Alber. Study of elastic collisions of myxococcus xanthus in swarms. *Phys. Biol.*, 8(2):026016, 2011.

[90] Sebastian A Sandersius, Manli Chuai, Cornelis J Weijer, and Timothy J Newman. Correlating cell behavior with tissue topology in embryonic epithelia. *PLoS One*, 6(4):e18081, April 2011.

[91] S A Sandersius, C J Weijer, and T J Newman. Emergent cell and tissue dynamics from subcellular modeling of active biomechanical processes. *Phys. Biol.*, 8(4):045007, August 2011.

[92] Sebastian A Sandersius and Timothy J Newman. Modeling cell rheology with the subcellular element model. *Phys. Biol.*, 5(1):015002, April 2008.

[93] Scott Christley, Mark S Alber, and Stuart A Newman. Patterns of mesenchymal condensation in a multiscale, discrete stochastic model. *PLoS Comput. Biol.*, 3(4):e76, April 2007.

[94] Timothy J Newman. Modeling multicellular structures using the subcellular element model. In Alexander R A Anderson, Mark A J Chaplain, and Katarzyna A Rejniak, editors, *Single-Cell-Based Models in Biology and Medicine*, pages 221–239. Birkhäuser Basel, Basel, 2007.

[95] Mikahl Banwarth-Kuhn. *Mathematical Model for Studying Combined Effect of Individual Cell Behavior on Developing Tissue Shape in Plants*. PhD thesis, University of California, Riverside, 2019.

[96] Martin Bringmann, Benoit Landrein, Christian Schudoma, Olivier Hamant, Marie-Theres Hauser, and Staffan Persson. Cracking the elusive alignment hypothesis: the microtubule–cellulose synthase nexus unraveled. *Trends Plant Sci.*, 17(11):666–674, November 2012.

[97] Tobias I Baskin. Anisotropic expansion of the plant cell wall. *Annu. Rev. Cell Dev. Biol.*, 21: 203–222, 2005.

[98] Mariano Perales, Kevin Rodriguez, Stephen Snipes, Ram Kishor Yadav, Mercedes Diaz-Mendoza, and G Venugopala Reddy. Threshold-dependent transcriptional discrimination underlies stem cell homeostasis. *Proc. Natl. Acad. Sci. U. S. A.*, 113(41):E6298–E6306, October 2016.

[99] Pablo Martinez, Lindy A Allsman, Kenneth A Brakke, Christopher Hoyt, Jordan Hayes, Hong Liang, Wesley Neher, Yue Rui, Allyson M Roberts, Amir Moradifam, Bob Goldstein, Charles T Anderson, and Carolyn G Rasmussen. Predicting division planes of Three-Dimensional cells by Soap-Film minimization. *Plant Cell*, 30(10):2255–2266, October 2018.

[100] Leia Colin, Antoine Chevallier, Satoru Tsugawa, Florian Gacon, Christophe Godin, Virgile Viasnoff, Timothy E Saunders, and Olivier Hamant. Cortical tension overrides geometrical cues to orient microtubules in confined protoplasts. *Proc. Natl. Acad. Sci. U. S. A.*, 117(51): 32731–32738, December 2020.

[101] Francis Corson, Olivier Hamant, Steffen Bohn, Jan Traas, Arezki Boudaoud, and Yves Couder. Turning a plant tissue into a living cell froth through isotropic growth. *Proc. Natl. Acad. Sci. U. S. A.*, 106(21):8453–8458, May 2009.

[102] Arun Sampathkumar, Alexis Peaucelle, Miki Fujita, Christoph Schuster, Staffan Persson, Geoffrey O Wasteneys, and Elliot M Meyerowitz. Primary wall cellulose synthase regulates shoot apical meristem mechanics and growth. *Development*, 146(10), May 2019.

[103] Carolyn G. Rasmussen and Marschal Bellinger. An overview of plant division-plane orientation. *New Phytologist*, 219(2):505–512, 2018. doi: https://doi.org/10.1111/nph.15183. URL `https://nph.onlinelibrary.wiley.com/doi/abs/10.1111/nph.15183`.

[104] Michelle R Facette, Carolyn G Rasmussen, and Jaimie M Van Norman. A plane choice: coordinating timing and orientation of cell division during plant development. *Curr. Opin. Plant Biol.*, 47:47–55, February 2019.

[105] Nancy A. Eckardt. High-resolution imaging of cortical microtubule arrays. *The Plant Cell*, 20(4):817–819, 2008. ISSN 1040-4651. doi: 10.1105/tpc.108.060228. URL `http://www.plantcell.org/content/20/4/817`.

[106] Vytautas Gapsys, Daniel Seeliger, and Bert L de Groot. New soft-core potential function for molecular dynamics based alchemical free energy calculations. *Journal of Chemical Theory and Computation*, 8(7):2373–2382, 2012.

[107] G. Venugopala Reddy, Marcus G. Heisler, David W. Ehrhardt, and Elliot M. Meyerowitz. Real-time lineage analysis reveals oriented cell divisions associated with morphogenesis at the shoot apex of Arabidopsis thaliana. *Development*, 131(17):4225–4237, 09 2004. ISSN 0950-1991. doi: 10.1242/dev.01261. URL `https://doi.org/10.1242/dev.01261`.

[108] Z Hejnowicz and J Karczewski. Modeling of meristematic growth of root apices in a natural coordinate system. *American Journal of Botany*, 80(3):309–315, 1993.

[109] Mikaela Koutrouli, Evangelos Karatzas, David Paez-Espino, and Georgios A Pavlopoulos. A guide to conquer the biological network era using graph theory. *Frontiers in Bioengineering and Biotechnology*, page 34, 2020.

[110] Mark EJ Newman. A measure of betweenness centrality based on random walks. *Social networks*, 27(1):39–54, 2005.

[111] Ilkka Kivimäki, Bertrand Lebichot, Jari Saramäki, and Marco Saerens. Two betweenness centrality measures based on randomized shortest paths. *Scientific reports*, 6(1):1–15, 2016.

[112] Masayuki Higuchi, Melissa S Pischke, Ari Pekka Mähönen, Kaori Miyawaki, Yukari Hashimoto, Motoaki Seki, Masatomo Kobayashi, Kazuo Shinozaki, Tomohiko Kato, Satoshi Tabata, Ykä Helariutta, Michael R Sussman, and Tatsuo Kakimoto. In planta functions of the arabidopsis cytokinin receptor family. *Proc. Natl. Acad. Sci. U. S. A.*, 101(23):8821–8826, June 2004.

[113] Marc Weber. statannot, 2019. URL `https://github.com/webermarcolivier/statannot`.

[114] Lisa Willis, Yassin Refahi, Raymond Wightman, Benoit Landrein, José Teles, Kerwyn Casey Huang, Elliot M Meyerowitz, and Henrik Jönsson. Cell size and growth regulation in the arabidopsis thaliana apical stem cell niche. *Proceedings of the National Academy of Sciences*, 113(51):E8238–E8246, 2016.

[115] Axel A Almet, Philip K Maini, Derek E Moulton, and Helen M Byrne. Modeling perspectives on the intestinal crypt, a canonical system for growth, mechanics, and remodeling. *Current Opinion in Biomedical Engineering*, 15:32–39, 2020.

[116] Esther J Pearl, Jingjing Li, and Jeremy BA Green. Cellular systems for epithelial invagination. *Philosophical Transactions of the Royal Society B: Biological Sciences*, 372(1720):20150526, 2017.

[117] Hanqing Guo, Michael Swan, and Bing He. Optogenetic inhibition of actomyosin reveals mechanical bistability of the mesoderm epithelium during drosophila mesoderm invagination. *ELife*, 11:e69082, 2022.

[118] Ulla-Maj Fiuza and Patrick Lemaire. Mechanical and genetic control of ascidian endoderm invagination during gastrulation. In *Seminars in Cell & Developmental Biology*, volume 120, pages 108–118. Elsevier, 2021.

[119] Morgen E. Anyan, Aboutaleb Amiri, Cameron W. Harvey, Giordano Tierra, Nydia Morales-Soto, Callan M. Driscoll, Mark S. Alber, and Joshua D. Shrout. Type IV pili interactions promote intercellular association and moderate swarming of Pseudomonas aeruginosa. *Proceedings of the National Academy of Sciences of the United States of America*, 111(50):18013–18018, dec 2014. ISSN 10916490. doi: 10.1073/pnas.1414661111. URL `http://www.pnas.org/lookup/doi/10.1073/pnas.1414661111`.

[120] Cameron W. Harvey, Faruck Morcos, Christopher R. Sweet, Dale Kaiser, Santanu Chatterjee, Xiaomin Liu, Danny Z. Chen, and Mark Alber. Study of elastic collisions of Myxococcus xanthus in swarms. *Physical Biology*, 8(2):026016, apr 2011. ISSN 14783975. doi: 10.1088/1478-3975/8/2/026016. URL `https://iopscience.iop.org/article/10.1088/1478-3975/8/2/026016`.

[121] Kathryn G. Link, Michael T. Stobb, Jorge Di Paola, Keith B. Neeves, Aaron L. Fogelson, Suzanne S. Sindi, and Karin Leiderman. A local and global sensitivity analysis of a mathematical model of coagulation and platelet deposition under flow. *PLoS ONE*, 13(7):e0200917, jul 2018. ISSN 19326203. doi: 10.1371/journal.pone.0200917.

[122] Simeone Marino, Ian B. Hogue, Christian J. Ray, and Denise E. Kirschner. A methodology for performing global uncertainty and sensitivity analysis in systems biology. *Journal of Theoretical Biology*, 254(1):178–196, sep 2008. ISSN 00225193. doi: 10.1016/j.jtbi.2008.04.011.

[123] Juan José Ripoll, Mingyuan Zhu, Stephanie Brocke, Cindy T. Hon, Martin F. Yanofsky, Arezki Boudaoud, and Adrienne H.K. Roeder. Growth dynamics of the Arabidopsis fruit is mediated by cell expansion. *Proceedings of the National Academy of Sciences of the United States of America*, 116(50):25333–25342, 2019. ISSN 10916490. doi: 10.1073/pnas.1914096116.

[124] M-P Dubuisson and Anil K Jain. A modified hausdorff distance for object matching. In *Proceedings of 12th international conference on pattern recognition*, volume 1, pages 566–568. IEEE, 1994.

[125] Andrea Saltelli, Marco Ratto, Terry Andres, Francesca Campolongo, Jessica Cariboni, Debora Gatelli, Michaela Saisana, and Stefano Tarantola. *Global Sensitivity Analysis. The Primer*. John Wiley & Sons, Ltd, Chichester, UK, dec 2007. ISBN 9780470725184. doi: 10.1002/9780470725184. URL `http://doi.wiley.com/10.1002/9780470725184`.

[126] Esther M. Arkin, L. Paul Chew, Daniel P. Huttenlocher, and Klara Kedem. An Efficiently Computable Metric for Comparing Polygonal Shapes, 1991. ISSN 01628828.

[127] Emily Atwood Williams and Elizabeth A. Wentz. Pattern analysis based on type, orientation, size, and shape. *Geographical Analysis*, 40(2):97–122, 2008. ISSN 00167363. doi: 10.1111/j.1538-4632.2008.00715.x.

[128] Bruce E. Shapiro, Cory Tobin, Eric Mjolsness, and Elliot M. Meyerowitz. Analysis of cell division patterns in the Arabidopsis shoot apical meristem. *Proceedings of the National Academy of Sciences of the United States of America*, 112(15):4815–4820, 2015. ISSN 10916490. doi: 10.1073/pnas.1502588112.

[129] I. M. Sobol. Global sensitivity indices for nonlinear mathematical models and their Monte Carlo estimates. *Mathematics and Computers in Simulation*, 55(1-3):271–280, 2001. ISSN 03784754. doi: 10.1016/S0378-4754(00)00270-6.

[130] Maikol SolÃs. Non-parametric estimation of the first-order sobol indices with bootstrap bandwidth. *Communications in Statistics - Simulation and Computation*, 50(9):2497–2512, 2021. doi: 10.1080/03610918.2019.1655575. URL `https://doi.org/10.1080/03610918.2019.1655575`.

[131] Magalie Uyttewaal, Agata Burian, Karen Alim, Benoît Landrein, Dorota Borowska-Wykręt, Annick Dedieu, Alexis Peaucelle, Michał Ludynia, Jan Traas, Arezki Boudaoud, et al. Mechanical stress acts via katanin to amplify differences in growth rate between adjacent cells in arabidopsis. *Cell*, 149(2):439–451, 2012.

[132] Ernesto ABF Lima, Danial Faghihi, Russell Philley, Jianchen Yang, John Virostko, Caleb M Phillips, and Thomas E Yankeelov. Bayesian calibration of a stochastic, multiscale agent-based model for predicting in vitro tumor growth. *PLoS Computational Biology*, 17(11):e1008845, 2021.

[133] Arezki Boudaoud. An introduction to the mechanics of morphogenesis for plant biologists. *Trends in plant science*, 15(6):353–360, 2010.

[134] John A Fozard, Mikaël Lucas, John R King, and Oliver E Jensen. Vertex-element models for anisotropic growth of elongated plant organs. *Frontiers in plant science*, 4:233, 2013.

[135] Aleksandr Bobrovskikh, Alexey Doroshkov, Stefano Mazzoleni, Fabrizio Cartenì, Francesco Giannino, and Ulyana Zubairova. A sight on single-cell transcriptomics in plants through the prism of cell-based computational modeling approaches: benefits and challenges for data analysis. *Frontiers in genetics*, 12:652974, 2021.

[136] Daniel L Barton, Silke Henkes, Cornelis J Weijer, and Rastko Sknepnek. Active vertex model for cell-resolution description of epithelial tissue mechanics. *PLoS computational biology*, 13 (6):e1005569, 2017.

[137] Donald A Fowler and Hans CE Larsson. The benefits differential equations bring to limb development. *Wiley Interdisciplinary Reviews: Developmental Biology*, 9(1):e364, 2020.

[138] Bin Yang and Yuehui Chen. Overview of gene regulatory network inference based on differential equation models. *Current Protein and Peptide Science*, 21(11):1054–1059, 2020.

[139] Zizhen Zhang, Anwar Zeb, Oluwaseun Francis Egbelowo, and Vedat Suat Erturk. Dynamics of a fractional order mathematical model for covid-19 epidemic. *Advances in Difference Equations*, 2020(1):1–16, 2020.

[140] Yuli Chen, Fawang Liu, Qiang Yu, and Tianzeng Li. Review of fractional epidemic models. *Applied mathematical modelling*, 97:281–307, 2021.

[141] Sajad Razavi Bazaz, Ali Mashhadian, Abbas Ehsani, Suvash Chandra Saha, Timm Krüger, and Majid Ebrahimi Warkiani. Computational inertial microfluidics: A review. *Lab on a Chip*, 20(6):1023–1048, 2020.

[142] Asit Saha and Barsha Saha. Novel coronavirus sars-cov-2 (covid-19) dynamics inside the human body. *Reviews in Medical Virology*, 30(5):e2140, 2020.

[143] Katherine Copenhagen, Ricard Alert, Ned S Wingreen, and Joshua W Shaevitz. Topological defects promote layer formation in myxococcus xanthus colonies. *Nature Physics*, 17(2):211–215, 2021.

[144] Nikodem J Popławski, Abbas Shirinifard, Maciej Swat, and James A Glazier. Simulation of single-species bacterial-biofilm growth using the glazier-graner-hogeweg model and the compucell3d modeling environment. *Mathematical biosciences and engineering: MBE*, 5(2):355, 2008.

[145] Jennifer C Fletcher, Ulrike Brand, Mark P Running, Rüdiger Simon, and Elliot M Meyerowitz. Signaling of cell fate decisions by CLAVATA3 in arabidopsis shoot meristems. *Science*, 283 (5409):1911–1914, March 1999.

[146] Léna Beauzamy, Marion Louveaux, Olivier Hamant, and Arezki Boudaoud. Mechanically, the shoot apical meristem of arabidopsis behaves like a shell inflated by a pressure of about 1 MPa. *Front. Plant Sci.*, 6:1038, November 2015.

[147] Saiko Yoshida, Pierre Barbier de Reuille, Brendan Lane, George W Bassel, Przemyslaw Prusinkiewicz, Richard S Smith, and Dolf Weijers. Genetic control of plant development by overriding a geometric division rule. *Dev. Cell*, 29(1):75–87, April 2014.

[148] Yong-He Ding, Nai-You Liu, Zuo-Shun Tang, Jie Liu, and Wei-Cai Yang. Arabidopsis GLUTAMINE-RICH PROTEIN23 is essential for early embryogenesis and encodes a novel nuclear PPR motif protein that interacts with RNA polymerase II subunit III. *Plant Cell*, 18 (4):815–830, April 2006.

[149] Ram Kishor Yadav, Mariano Perales, Jérémy Gruel, Carolyn Ohno, Marcus Heisler, Thomas Girke, Henrik Jönsson, and G Venugopala Reddy. Plant stem cell maintenance involves direct transcriptional repression of differentiation program. *Mol. Syst. Biol.*, 9:654, 2013.

[150] S Satina, A F Blakeslee, and Amos G Avery. Demonstration of the three germ layers in the shoot apex of datura by means of induced polyploidy in periclinal chimeras. *Am. J. Bot.*, 27 (10):895–905, 1940.

[151] Jan Traas and Teva Vernoux. The shoot apical meristem: the dynamics of a stable structure. *Philos. Trans. R. Soc. Lond. B Biol. Sci.*, 357(1422):737–747, June 2002.

[152] Jérémy Gruel, Benoit Landrein, Paul Tarr, Christoph Schuster, Yassin Refahi, Arun Sampathkumar, Olivier Hamant, Elliot M Meyerowitz, and Henrik Jönsson. An epidermis-driven mechanism positions and scales stem cell niches in plants. *Sci Adv*, 2(1):e1500989, January 2016.

[153] H Jönsson, B E Shapiro, E M Meyerowitz, and E Mjolsness. Modeling plant development with gene regulation networks including signaling and cell division. In Nikolay Kolchanov and

Ralf Hofestaedt, editors, *Bioinformatics of Genome Regulation and Structure*, pages 311–318. Springer US, Boston, MA, 2004.

[154] Anne Vatén, Jan Dettmer, Shuang Wu, York-Dieter Stierhof, Shunsuke Miyashima, Shri Ram Yadav, Christina J Roberts, Ana Campilho, Vincent Bulone, Raffael Lichtenberger, Satu Lehesranta, Ari Pekka Mähönen, Jae-Yean Kim, Eija Jokitalo, Norbert Sauer, Ben Scheres, Keiji Nakajima, Annelie Carlsbecker, Kimberly L Gallagher, and Ykä Helariutta. Callose biosynthesis regulates symplastic trafficking during root development. *Dev. Cell*, 21(6):1144–1155, December 2011.

[155] P L Rinne and C van der Schoot. Symplasmic fields in the tunica of the shoot apical meristem coordinate morphogenetic events. *Development*, 125(8):1477–1485, April 1998.

[156] Sandra Ormenese, Georges Bernier, and Claire Périlleux. Cytokinin application to the shoot apical meristem of sinapis alba enhances secondary plasmodesmata formation. *Planta*, 224(6): 1481–1484, November 2006.

[157] Emmanuelle Bayer, Carole Thomas, and Andy Maule. Symplastic domains in the arabidopsis shoot apical meristem correlate with PDLP1 expression patterns. *Plant Signal. Behav.*, 3(10): 853–855, October 2008.

[158] Gabor Daum, Anna Medzihradszky, Takuya Suzaki, and Jan U Lohmann. A mechanistic framework for noncell autonomous stem cell induction in arabidopsis. *Proceedings of the National Academy of Sciences*, 111(40):14619–14624, October 2014.

[159] G Eric Schaller, Ian H Street, and Joseph J Kieber. Cytokinin and the cell cycle. *Curr. Opin. Plant Biol.*, 21:7–15, October 2014.

[160] Juan Carlos Montesinos, Anas Abuzeineh, Aglaja Kopf, Alba Juanes-Garcia, Krisztina Ötvös, Jan Petrášek, Michael Sixt, and Eva Benková. Phytohormone cytokinin guides microtubule

dynamics during cell progression from proliferative to differentiated stage. *EMBO J.*, 39(17): e104238, September 2020.

[161] Dajian Zhang, Xiaomin Wang, Min Wang, Junhua Li, Xiaoyu Guo, Kang Chong, and Yunyuan Xu. Ectopic expression of WUS in hypocotyl promotes cell division via GRP23 in arabidopsis. *PLoS One*, 8(9):e75773, September 2013.

[162] K F Mayer, H Schoof, A Haecker, M Lenhard, G Jürgens, and T Laux. Role of WUSCHEL in regulating stem cell fate in the arabidopsis shoot meristem. *Cell*, 95(6):805–815, December 1998.

[163] Kevin Rodriguez, Mariano Perales, Stephen Snipes, Ram Kishor Yadav, Mercedes Diaz-Mendoza, and G Venugopala Reddy. DNA-dependent homodimerization, sub-cellular partitioning, and protein destabilization control WUSCHEL levels and spatial patterning. *Proc. Natl. Acad. Sci. U. S. A.*, 113(41):E6307–E6315, October 2016.

[164] Ulrike Brand, Margit Grünewald, Martin Hobe, and Rüdiger Simon. Regulation of CLV3 expression by two homeobox genes in arabidopsis. *Plant Physiol.*, 129(2):565–575, June 2002.

[165] Lisa Willis, Yassin Refahi, Raymond Wightman, Benoit Landrein, José Teles, Kerwyn Casey Huang, Elliot M Meyerowitz, and Henrik Jönsson. Cell size and growth regulation in the arabidopsis thaliana apical stem cell niche. *Proc. Natl. Acad. Sci. U. S. A.*, 113(51):E8238–E8246, December 2016.

[166] Yong-Tao Zhang, Mark S Alber, and Stuart A Newman. Mathematical modeling of vertebrate limb development. *Math. Biosci.*, 243(1):1–17, May 2013.

[167] Michael C Mackey and Philip K Maini. What has mathematics done for biology? *Bull. Math. Biol.*, 77(5):735–738, May 2015.

[168] Isaac Salazar-Ciudad, Jukka Jernvall, and Stuart A Newman. Mechanisms of pattern formation in development and evolution. *Development*, 130(10):2027–2037, May 2003.

[169] Przemyslaw Prusinkiewicz and Anne-Gaëlle Rolland-Lagan. Modeling plant morphogenesis. *Curr. Opin. Plant Biol.*, 9(1):83–88, February 2006.

[170] Jannik Vollmer, Fernando Casares, and Dagmar Iber. Growth and size control during development. *Open Biol.*, 7(11), November 2017.

[171] Vijay Velagala, Weitao Chen, Mark Alber, and Jeremiah J. Zartman. Chapter 4.1 - multiscale models coupling chemical signaling and mechanical properties for studying tissue growth. In Glen L. Niebur, editor, *Mechanobiology*, pages 173 – 195. Elsevier, 2020. ISBN 978-0-12-817931-4. doi: https://doi.org/10.1016/B978-0-12-817931-4.00010-8. URL http://www.sciencedirect.com/science/article/pii/B9780128179314000108.